

# A New System for Online Measurement of the Beam Emittance of Particle Accelerators for Research and medical Applications

Inauguraldissertation  
der Philosophisch-naturwissenschaftlichen Fakultät  
der Universität Bern

vorgelegt von

**Konrad Paweł Nesteruk**

von Polen

Leiter der Arbeit:

Prof. Dr. Antonio Ereditato

Albert Einstein Center for Fundamental Physics

Laboratorium für Hochenergiephysik

Physikalisches Institut



# A New System for Online Measurement of the Beam Emittance of Particle Accelerators for Research and medical Applications

Inauguraldissertation  
der Philosophisch-naturwissenschaftlichen Fakultät  
der Universität Bern

vorgelegt von

**Konrad Paweł Nesteruk**

von Polen

Leiter der Arbeit:

Prof. Dr. Antonio Ereditato

Albert Einstein Center for Fundamental Physics

Laboratorium für Hochenergiephysik

Physikalisches Institut

Von der Philosophisch-naturwissenschaftlichen Fakultät angenommen.

Bern, 29.06.2017

Der Dekan  
Prof. Dr. Gilberto Colangelo



I don't want to believe.

I want to know.

— Carl Sagan

To my parents...



# Acknowledgements

I would like to thank Prof. Antonio Ereditato, my supervisor and the director of the Albert Einstein Center for Fundamental Physics - Laboratory for High Energy Physics, for the opportunity to work in a great international team and to take part in many interesting research activities.

I would like to express my gratitude to PD Dr. Saverio Braccini, my tutor and the leader of the group, in which I was working during the whole Ph.D. period. Thank you for all the fruitful discussions and advice. I have learnt a lot from you and you helped me to become a mature researcher.

I am very grateful to Dr. Callum Wilkinson, who carefully read the draft of my thesis. Thank you very much for all the suggestions and invaluable support during the writing process.

My warmest thoughts go to Tommaso Carzaniga, my great friend, collaborator, and office mate. I really enjoyed working with you and I appreciate all the support I received from you.

I would like to thank all the friends from LHEP, especially Callum, Gigi, Mykhi, and Tommy, for all the great time spent together, which helped me a lot to survive!

Finally, I would like to acknowledge my family. I always receive invaluable support from them. I would like to express special thanks to my mother Teresa, who helped me to develop my scientific interests and supported mentally during the whole Ph.D. period. Last but not least, I thank my girlfriend Magda for her care, understanding, and patience.



# Contents

<b>Acknowledgements</b>	<b>i</b>
<b>List of figures</b>	<b>v</b>
<b>List of tables</b>	<b>ix</b>
<b>Introduction</b>	<b>1</b>
<b>1 Cyclotrons</b>	<b>7</b>
1.1 Historical overview . . . . .	7
1.2 Physics principles . . . . .	8
1.2.1 Lawrence cyclotron . . . . .	8
1.2.2 Orbit stability . . . . .	10
1.2.3 Longitudinal stability . . . . .	15
1.2.4 Azimuthally varying field cyclotron . . . . .	16
1.3 Medical cyclotrons . . . . .	19
<b>2 Transverse beam dynamics</b>	<b>21</b>
2.1 Beam transport . . . . .	21
2.2 Transverse beam emittance . . . . .	27
2.3 Energy spread and its influence on the transverse beam dynamics . . . .	32
2.4 Methods of transverse emittance measurements . . . . .	34
2.4.1 The “pepper-pot” technique . . . . .	35
2.4.2 Quadrupole variation . . . . .	35
2.4.3 Use of multiple beam profilers . . . . .	36

## Contents

---

<b>3</b>	<b>The 18 MeV Bern medical cyclotron</b>	<b>39</b>
3.1	Machine characteristics . . . . .	40
3.2	Beam transport line . . . . .	44
3.3	Low current beams . . . . .	46
<b>4</b>	<b>A system for online measurement of the transverse beam emittance</b>	<b>51</b>
4.1	The UniBEaM detector for monitoring ion beams . . . . .	52
4.1.1	Principles of operation . . . . .	52
4.1.2	Performance of UniBEaM with 18 MeV proton beams . . . . .	54
4.1.3	Beam monitoring with non-doped silica fibers . . . . .	60
4.1.4	Monitoring of high-energy proton and pion beams . . . . .	62
4.1.5	Commercial UniBEaM detector . . . . .	65
4.2	<sup>4</sup> PrOB $\epsilon$ aM: a system for online measurement of the transverse beam emittance . . . . .	68
<b>5</b>	<b>Characterization of proton beams</b>	<b>73</b>
5.1	Beam characterization of the 18 MeV Bern cyclotron . . . . .	74
5.1.1	Transverse RMS beam emittance as a function of the cyclotron parameters . . . . .	74
5.1.2	Transverse RMS beam emittance for the standard cyclotron settings	81
5.1.3	Proton energy distribution . . . . .	84
5.1.4	Simulation of the Beam Transport Line . . . . .	87
5.2	Transverse beam emittance of the TR24 Strasbourg cyclotron . . . . .	92
	<b>Conclusions</b>	<b>97</b>
	<b>A Appendix</b>	<b>99</b>
	<b>Bibliography</b>	<b>158</b>
	<b>Curriculum Vitae</b>	<b>161</b>

# List of Figures

1.1	Classical cyclotron. . . . .	9
1.2	Particle deviated from the equilibrium orbit. . . . .	11
1.3	Weak focusing. . . . .	15
1.4	AVF pole tip. . . . .	16
1.5	Azimuthal field component created with the AVF pole tips. . . . .	17
1.6	The principle of Thomas focusing. . . . .	17
2.1	Quadrupole magnet. . . . .	25
2.2	field profile in a real quadrupole. . . . .	26
2.3	Phase space ellipse. . . . .	28
2.4	Transformation of a phase space ellipse along a drift section. . . . .	31
2.5	Transformation of a phase space ellipse due to focusing. . . . .	31
2.6	Illustration of the “pepper-pot” method to measure transverse beam emittance. . . . .	34
3.1	The Bern medical cyclotron. . . . .	40
3.2	A stripper disassembled from the Bern cyclotron. . . . .	41
3.3	RF cavities and accelerating gaps. . . . .	42
3.4	RF voltage as a function of the RF phase within an RF cavity. . . . .	43
3.5	Schematic drawing of a cold-cathode PIG ion source. . . . .	44
3.6	Schematic view of the Beam Transport Line (BTL). . . . .	45
3.7	Photograph of the BTL during the alignment of an experimental set-up. . . . .	46
3.8	High-sensitivity Faraday cup. . . . .	47
3.9	Beam current as a function of the RF peak voltage. . . . .	48
3.10	Beam current as a function of the current in the main coil of the cyclotron. . . . .	49

## List of Figures

---

4.1	The UniBEaM detector installed on the BTL of the Bern cyclotron. . . . .	53
4.2	Typical experimental set-up of the UniBEaM detector. . . . .	54
4.3	The UniBEaM detector and the Faraday cup installed on the BTL of the Bern cyclotron. . . . .	55
4.4	Profiles of pA proton beams measured with a Ce <sup>3+</sup> doped silica fiber. . .	56
4.5	Profile integral as a function of beam current in the pA range. . . . .	57
4.6	Profile of a 50 nA proton beam measured with an Sb <sup>3+</sup> doped silica fiber. .	58
4.7	Profile integral as a function of beam current in the nA and $\mu$ A range. . .	58
4.8	Seven consecutive beam profiles measured at a current intensity of 20 $\mu$ A. .	59
4.9	Profiles of proton beams measured with a non-doped silica fiber. . . . .	61
4.10	Profile integral as a function of beam current for a non-doped optical fiber	62
4.11	The UniBEaM detector located in the air after the exit window of one of the SPS secondary beam lines at CERN. . . . .	63
4.12	Beam profile of the hadron beam measured with the in-air UniBEaM detector at the CERF facility. . . . .	64
4.13	Intensity of successive spills of the SPS synchrotron at CERN. . . . .	65
4.14	D-Pace's commercial UniBEaM dual axis probe (left) and its internal view (right). . . . .	66
4.15	D-Pace's commercial UniBEaM installed on the BTL. . . . .	67
4.16	User interface of the commercial UniBEaM detector. . . . .	67
4.17	The <sup>4</sup> PrOB $\epsilon$ aM system for online measurement of the transverse beam emittance. . . . .	68
4.18	Readout system of <sup>4</sup> PrOB $\epsilon$ aM located in the control room. . . . .	69
4.19	Four beam profiles measured with the <sup>4</sup> PrOB $\epsilon$ aM system. . . . .	70
4.20	Variance as a function of the distance from the first UniBEaM detector obtained with the <sup>4</sup> PrOB $\epsilon$ aM system. . . . .	71
5.1	The <sup>4</sup> PrOB $\epsilon$ aM system and a Faraday cup installed on the BTL. . . . .	74
5.2	The horizontal and vertical transverse RMS emittance as a function of the main coil current for cold machine. . . . .	76
5.3	Comparison of the dependency of the horizontal and vertical RMS trans- verse emittance on the main coil current for cold and warm machine. . .	77

5.4 The horizontal and vertical transverse RMS emittance as a function of the RF peak voltage. . . . .	79
5.5 The horizontal and vertical transverse RMS emittance as a function of the stripper angle. . . . .	80
5.6 Variance as a function of the quadrupole current obtained for the horizontal and vertical planes. . . . .	82
5.7 Variance as a function of the location obtained for the horizontal and vertical planes. . . . .	83
5.8 Schematic of the experimental method of the proton energy distribution measurement. . . . .	86
5.9 Distribution of the proton energy. . . . .	87
5.10 The horizontal and vertical $1\sigma$ -phase-space ellipses at the injection to the BTL. . . . .	88
5.11 User interface of the BTL simulation in Maple. . . . .	89
5.12 Output of the BTL simulation in Maple for the horizontal plane. . . . .	90
5.13 Histogram representing a beam profile at a chosen location along the BTL. . . . .	91
5.14 Simulated beam envelope in both horizontal and vertical planes. . . . .	92
5.15 The TR24 cyclotron and its beamline at IPHC in Strasbourg. . . . .	93
5.16 The $^4\text{PrOB}\epsilon\text{aM}$ system installed on the beamline of the TR24 cyclotron in Strasbourg. . . . .	93
5.17 Variance as a function of the location obtained for the horizontal and vertical planes with the 18 MeV proton beam. . . . .	94
5.18 The RMS transverse beam emittance of the 18 MeV proton beam of the TR24 Strasbourg cyclotron as a function of stripper position. . . . .	96
5.19 The RMS transverse beam emittance of the 25 MeV proton beam of the TR24 Strasbourg cyclotron as a function of stripper position. . . . .	96



# List of Tables

3.1	Main characteristics of the Bern medical cyclotron. . . . .	41
5.1	The standard settings of the cyclotron parameters used for research purposes. . . . .	75
5.2	Fit parameters and the RMS emittance values obtained by quadrupole variation for both horizontal and vertical planes [36]. . . . .	81
5.3	Fit parameters and the RMS emittance values obtained by using multiple profilers for both horizontal and vertical planes [36]. . . . .	84
5.4	List of absorbers used for the measurement of the proton energy distribution. . . . .	85



# Introduction

Particle accelerators are widely used in research, industry, and medicine. Depending on the specific use, different types of accelerator are concerned, which vary in size, energy, particle species, and acceleration technology. There are nearly 20000 accelerators in operation around the world, among which about half are employed for biomedical use [1]. In particular, accelerated beams of charged hadrons allow tumors to be treated with high precision. This modality of radiation therapy for cancer treatment is called hadrontherapy [2]. Beams of charged particles are also used for radioisotope production. One of the most commonly produced isotopes is  $^{18}\text{F}$ , which is used for synthesis of a radiotracer called FDG for Positron Emission Tomography (PET) [3]. In both therapeutic and diagnostic uses of accelerators, a precise understanding of the beam properties is essential. Furthermore, multi-disciplinary research in the field of medical applications of physics is not possible without beam diagnostics tools to characterize beam dynamics and to control crucial parameters such as beam size, shape, and intensity. These challenges constitute the motivation for the work reported here.

In this thesis, I will present a new system for online measurement of the transverse beam emittance of particle accelerators. It is named  $^4\text{PrOB}\epsilon\text{aM}$ , which stands for 4-Profilers Online Beam Emittance Measurement, and can be installed at any location along a beamline or directly at an accelerator outport. The beam emittance is the main quantity characterizing an accelerated particle beam. Since its value often depends on many machine parameters, the possibility of measuring it online is essential for many studies carried out at accelerator facilities. The system is aimed for charged beams used in medical applications. However, since it can be operated over a wide intensity

## Introduction

---

range, one could well envision the use  ${}^4\text{PrOB}\epsilon\text{aM}$  at some facilities for fundamental research. I developed this system based on four beam profile detectors named Universal BEam Monitor (UniBEaM). The UniBEaM profiler has been developed at the Albert Einstein Center for Fundamental Physics - Laboratory for High Energy Physics in the University of Bern with my significant contribution. This detector uses a scintillating fiber that moves through an ion beam. At each position the light yield, caused by charged particles passing through the fiber, is measured.

The IBA Cyclone 18 MeV proton cyclotron designed for PET radioisotope production is in operation at the Bern University Hospital (Inselspital). It is used for both daily radioisotope production and multidisciplinary research. The new system for making the beam emittance measurements has been tested at this facility and the proton beam was characterized at the Beam Transport Line (BTL) ending in a separate bunker. The system was also deployed to evaluate the transverse beam emittance of the TR24 cyclotron at IPHC in Strasbourg (France).

This thesis is structured in five chapters. The first chapter provides an overview of cyclotrons, as they are of direct interest for the studies reported in the thesis. The history of the cyclotron, its physics principles, and its medical applications are presented.

In the second chapter, the fundamentals of transverse beam dynamics are discussed. Beam transport formalism is described and the concept of beam emittance is explained. This is followed by consideration of the beam energy spread and its influence on transverse dynamics. Eventually, a general overview of measurement methods of the transverse beam emittance is given.

The 18 MeV Bern cyclotron is presented in the third chapter. Machine characteristics are provided and the specifically designed beamline is described. In the last section, special attention is given to low current beams. A method developed and proven by our group, with my contribution, allows the production of beam intensities 7 orders of magnitude lower than guaranteed by the cyclotron manufacturer. This achievement opens the way for several multidisciplinary scientific activities not usually performed with this kind of accelerator such as, for instance, radiation biophysics.

The fourth chapter is devoted to the  ${}^4\text{PrOB}\epsilon\text{aM}$  system. Since the core of  ${}^4\text{PrOB}\epsilon\text{aM}$  is the UniBEaM detector, a detailed description of the profiler is provided. The principle of operation is presented. The detector performance is shown for different beam current ranges from 1 pA to tens of  $\mu\text{A}$ . A special mode of operation with the use of non-doped silica fibers is reported. The results with high-energy beams, obtained with a specific version of the profiler, are also presented. In the last subsection devoted to UniBEaM, its commercial version is presented. In the second section, the  ${}^4\text{PrOB}\epsilon\text{aM}$  system is described. Its basic features and specific software for measuring the emittance online are reported.

In the fifth chapter, I present work on the characterization of proton beams. An experimental study conducted at the BTL of the Bern medical cyclotron is reported in the first section. The results of the measurements of the transverse RMS beam emittance as a function of some cyclotron parameters are presented. A separate subsection is devoted to the beam emittance measurements for the standard cyclotron settings performed with two different techniques. The next subsection reports measurement of the beam energy distribution with a method I proposed. It is based on aluminum absorbers of different thicknesses, a UniBEaM detector, and a Faraday cup. Using the results of the presented study, I developed a simulation of the BTL, which is described in the last subsection. This tool allows for online machine parameter tuning and for the optimization of the beam characteristics for specific applications. In the second section, the measurements of the transverse RMS emittance at the TR24 Strasbourg cyclotron are reported.

In the Appendix, I reprint the following papers I authored, which are the most significant with respect to the work presented in this thesis:

1. M. Auger, K. P. Nesteruk et al., *Low current performance of the Bern medical cyclotron down to the pA range*, Meas. Sci. Technol. **26**: 094006, 2015
2. M. Auger, K. P. Nesteruk et al., *A detector based on silica fibers for ion beam monitoring in a wide current range*, JINST **11**: P03027, 2016
3. M. Auger, K. P. Nesteruk (*corresponding author*) et al., *UniBEaM: a silica fiber*

## Introduction

---

- monitor for charged particle beams*, Proceedings of WTTC16, Santa Fe (NM), USA, AIP Conf. Proc. **1845**:020015, 2016
4. D. E. Potkins, K. P. Nesteruk et al., *A low-cost beam profiler based on cerium-doped silica fibers*, Proceedings of CAARI-16, Fort Worth (TX), USA, Physics Procedia (*submitted*)
  5. K. P. Nesteruk et al., *A system for online beam emittance measurements and proton beam characterization*, JINST (*submitted*, Ref. JINST\_102P\_0517, arXiv:1705.07486)
  6. K. P. Nesteruk et al., *Study of the transverse beam emittance of the Bern medical cyclotron*, Proceedings of IBIC2015, Melbourne, Australia, MOPB041:134-138, 2015, <http://www.jacow.org>

I also contributed to the following papers (in reverse chronological order):

1. M. Auger, K. P. Nesteruk et al., *Measurement of Sc-43 and Sc-44 production cross-section with an 18 MeV medical PET cyclotron*, Appl. Radiat. Isot. *submitted*, Ref. ARI\_2017\_438
2. M. Auger, K. P. Nesteruk et al., *Proton scattering radiography using an emulsion detector: a feasibility study*, Radiotherapy and Oncology, **118**:S21-S22, 2016
3. M. Auger, K. P. Nesteruk et al., *An online beam monitor detector for medical applications of ion beams*, Radiotherapy and Oncology, **118**:S13-S14, 2016
4. M. Auger, K. P. Nesteruk (*corresponding author*) et al., *Accelerator and detector physics at the Bern medical cyclotron and its beam transport line*, Nukleonika **61**(1):11-14, 2016
5. A. Ariga, K. P. Nesteruk et al., *Characterization of the dose distribution in the halo region of a clinical proton pencil beam using emulsion film detectors*, JINST **10**:P01007, 2015
6. S. Braccini, K. P. Nesteruk et al., *Study of the radioactivity induced in air by a 15 MeV proton beam*, Radiat. Prot. Dosim. **163** (3): 269-275, 2015

7. S. Braccini, K. P. Nesteruk et al., *Emulsion detectors for dose distribution characterization in the halo of proton pencil beams*, *Strahlenther Onkol* **191** (1): 87, 2014
8. K. P. Nesteruk, *Beam monitor detectors for medical applications*, *Rep. Pract. Oncol. Radiother.* **19**:S32-S36, 2014
9. S. Braccini, K. P. Nesteruk et al., *An innovative on-line beam-monitoring detector based on the emission of secondary electrons*, *Radiotherapy and Oncology*, **110** S1:S14, 2014
10. S. Braccini, K. P. Nesteruk et al., *A beam monitor detector based on doped silica and optical fibres*, *JINST* **7**:T02001, 2012 and arXiv:1110.1583



# 1 Cyclotrons

Cyclotrons are particle accelerators of direct interest for the studies conducted in this work. Their history, physics principles, and some features of medical cyclotrons are provided in this chapter.

## 1.1 Historical overview

The concept of the cyclotron originated in 1929 from Ernest O. Lawrence. The first model was constructed a year later by Lawrence and Edlefsen, and definite proof of the acceleration of particles was established by M. S. Livingston in 1931 [4]. Lawrence was searching for a method to accelerate particles to higher energies than was attainable at that time with DC potentials in order to study nuclear excitations. To avoid using too many electrodes, he considered employing a magnetic field to deflect particles in circular paths and make them pass the same gap with an electric field multiple times. The equation of motion for such a scenario leads to a constant period of revolution. Particles gain energy on each traversal of the gap, the orbit radius increases but the frequency remains constant. This is nowadays known as the cyclotron resonance principle and the corresponding frequency is called the cyclotron frequency. The first practical cyclotron produced  $\text{H}_2^+$  of 0.5 MeV energy by December 1931 and protons of 1.22 MeV, with beam currents of about  $10^{-9}$  A, in January 1932 [5]. For the invention of the cyclotron, Lawrence was awarded the 1939 Nobel prize in physics.

## Chapter 1. Cyclotrons

---

By 1945 it was discovered that these machines were limited by relativity. As the particle gains more energy it behaves like a higher mass particle. Because the radiofrequency (RF) voltage across the electrodes is constant, the effect of the kick is weaker on the more massive ions. Ions are out of phase with the RF cycle and there is no more acceleration. Due to this fact, a 184-inch cyclotron proposed by Lawrence was finally converted into a frequency modulated cyclotron and completed at the Lawrence Radiation Laboratory in Berkeley in 1946. This kind of machine is today known as synchrocyclotron. The one in Berkeley was delivering 190 MeV deuterons, 380 MeV alphas, and later 350 MeV protons [6].

An alternative to a synchrocyclotron is an isochronous cyclotron. In this case, instead of varying frequency, a magnetic field is radially changed to keep the particles in phase with the RF system. This leads to problems with vertical focusing. A solution was proposed by L. H. Thomas in 1938. By introducing azimuthal variations in the field strength, the desired focusing effect is obtained. This kind of isochronous cyclotrons is called an Azimuthally Varying Field (AVF) cyclotron. The first successful experiments were conducted in early 1950s and now almost all the modern cyclotrons are built with AVF pole tips.

## 1.2 Physics principles

### 1.2.1 Lawrence cyclotron

The simplest version of the cyclotron consists of an accelerating chamber with two hollow electrodes called “dees”, as in the earliest models they were D-shaped. A radio-frequency (RF) voltage is applied between the electrodes providing an alternating electric field in the gap and no field inside the dees. The chamber is placed between two poles of a magnet. The dipole magnet produces a constant and almost uniform magnetic field perpendicular to the plane of the dees. The original concept of the cyclotron is sketched in figure 1.1.

When an ion moves in a circular path, the electromagnetic force supplies the cen-

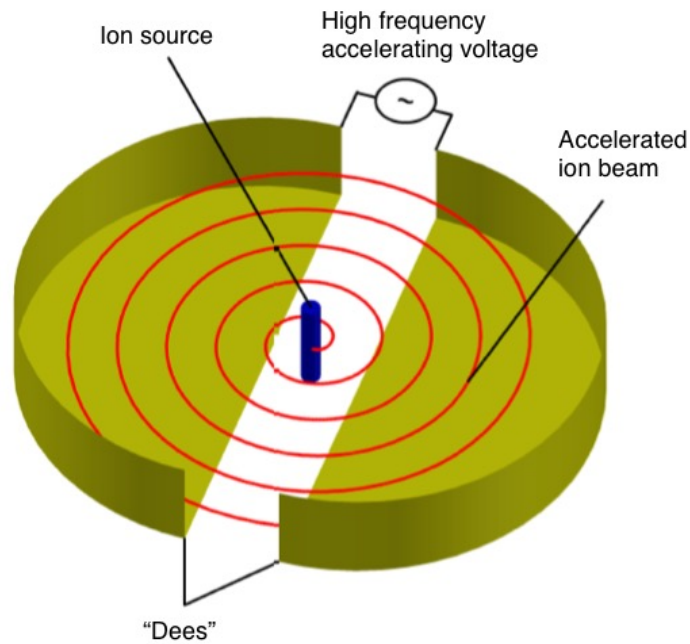


Figure 1.1 – Schematic diagram of the classical cyclotron. The magnetic field is perpendicular to the plane of ion beam circulation.

tripetal force. Thus,

$$\frac{Mv^2}{r} = qvB, \quad (1.1)$$

where  $M$  is the mass of the ion,  $v$  its velocity,  $q$  its charge,  $r$  is the radius of curvature of the path, and  $B$  the magnetic field strength. Hence, the velocity of the particle

$$v = \frac{qBr}{M}. \quad (1.2)$$

The time  $T$  to complete one circular orbit is therefore

$$T = \frac{2\pi r}{v} = \frac{2\pi M}{Bq}. \quad (1.3)$$

The last equation shows that the period of revolution depends only on the field strength and on the charge-to-mass ratio of the ion. This feature is the basis of the success of Lawrence concept. To make a cyclotron work, the electrical period of the RF system must be equal to the period of revolution. This can be realized either by tuning radio-frequency or adjusting the magnetic field strength. Equation (1.3) can

be transformed into the expression for the radian frequency  $\omega$  (also called angular velocity)

$$\omega = \frac{qB}{M}. \quad (1.4)$$

The latter is called cyclotron frequency. Particles circulate with this frequency until extraction and as energy increases after passing through an accelerating gap, the radius of the circular orbit increases. Acceleration is realized by applying an RF accelerating voltage between the dees

$$V = V_0 \cos(\omega_{RF} t), \quad (1.5)$$

where  $V_0$  is the peak voltage,  $t$  is time, and  $\omega_{RF}$  must fulfil the condition

$$\omega_{RF} = h\omega_{rev}, \quad (1.6)$$

where  $h = 1, 2, 3, \dots$  is the RF harmonic and  $\omega_{rev}$  is the cyclotron frequency. Under this condition, isochronism is obtained, meaning the particle takes the same amount of time to travel one turn and arrives always at the same RF phase in the middle of the accelerating gap. The classical cyclotron has many limits, which apply to both the transverse and longitudinal beam dynamics. Regarding the transverse dynamics, the homogeneous magnetic field leads to the lack of axial stability resulting in a linear growth to the vertical beam size. The primary problem concerning longitudinal dynamics are relativistic effects leading to the loss of synchronization with the accelerating voltage. The limits of classical cyclotron are discussed in the next sections.

### 1.2.2 Orbit stability

One of the challenges of cyclotron design is obtaining radial and axial orbit stability [4]. As was mentioned in the previous section, a homogeneous magnetic field results in orbit instabilities. Let's consider first the radial stability. Let  $x$  be a small deviation from the equilibrium circular orbit of radius  $r_e$  with  $x \ll r_e$ , as depicted in figure 1.2.

We also allow the magnetic field  $B$  to vary radially. The equation of motion is

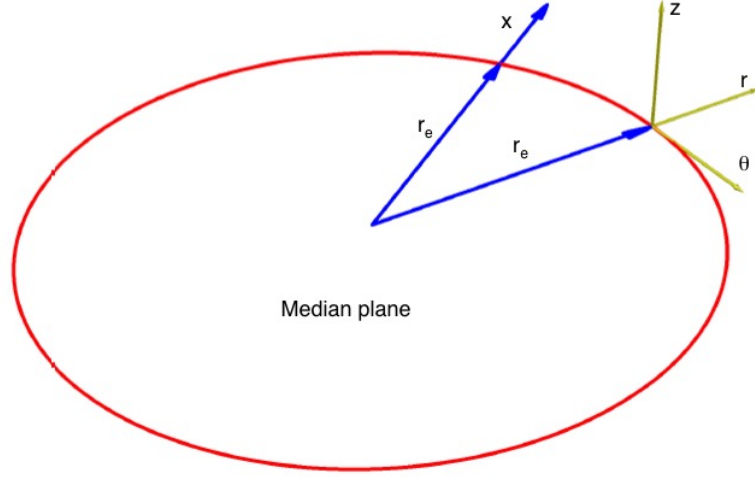


Figure 1.2 – Particle deviated from the equilibrium orbit.

$$M \frac{d^2(r_e + x)}{dt^2} - \frac{Mv_\theta^2}{r_e + x} + qvB_x = 0, \quad (1.7)$$

where  $B_x$  is the field at radius  $r_e + x$ . Since  $x \ll r_e$ , the factor  $1/(r_e + x)$  can be expressed as

$$\frac{1}{r_e + x} = \frac{1}{r_e \left(1 + \frac{x}{r_e}\right)} \approx \frac{1}{r_e} \left(1 - \frac{x}{r_e}\right). \quad (1.8)$$

Using the last equation and the facts that  $r_e$  is constant and  $Mv_\theta^2/r_e = qvB_e$ , where  $B_e$  is the field at  $r_e$ , we obtain

$$M \frac{d^2x}{dt^2} - qv_\theta B_e \left(1 - \frac{x}{r_e}\right) + qv_\theta B_x = 0, \quad (1.9)$$

$$M \frac{d^2x}{dt^2} + qv_\theta (B_x - B_e) + qv_\theta B_e \frac{x}{r_e} = 0. \quad (1.10)$$

The radial dependence of the field for small displacements can be expressed with a Taylor expansion:

$$B_x \approx B_e + \frac{\partial B}{\partial r} x. \quad (1.11)$$

## Chapter 1. Cyclotrons

---

This fact, together with the approximation that for the off-orbit ion  $v_\theta \approx \omega r_e$ , and the relation  $q/M = \omega/B_e$  leads to the following form for the equation of motion:

$$\frac{d^2 x}{dt^2} + \frac{r_e}{B_e} \frac{\partial B}{\partial r} \omega^2 x + \omega^2 x = 0. \quad (1.12)$$

The factor

$$n = -\frac{r_e}{B_e} \frac{\partial B}{\partial r} \quad (1.13)$$

is called the *field index* in the neighborhood of  $r_e$ . By plugging the field index  $n$  in equation (1.12), we obtain the Kerst-Serber equation [7]:

$$\frac{d^2 x}{dt^2} + \omega^2 x(1 - n) = 0. \quad (1.14)$$

The solution of this equation is either  $x = 0$  and corresponds to the equilibrium orbit or, provided that  $n < 1$ , is a simple harmonic motion of the deviation  $x$ :

$$x = x_0 \sin\left(\sqrt{1 - n}\omega t\right), \quad (1.15)$$

where  $x_0$  is the amplitude, and the radian frequency  $\omega_x$  is

$$\omega_x = \omega\sqrt{1 - n}. \quad (1.16)$$

The particle oscillates around the equilibrium orbit with this frequency and these oscillations are called the *radial betatron oscillations*. The number of such oscillations per turn is called the *radial tune* and is given by

$$\nu_r = \frac{\omega_x}{\omega} = \sqrt{1 - n}. \quad (1.17)$$

The radial stability condition is fulfilled when the field index  $n$  is smaller than one and consequently the radial tune  $\nu_r$  is bigger than zero.

Now, let's consider the axial stability. For a simple analysis, we assume that the particle does not vary in radial position and maintains constant azimuthal velocity  $v_\theta$ . To

provide a restoring force for particles, which are axially deviated from the equilibrium orbit, there is a need for a radial component  $B_r$  of the magnetic field above and below the median plane. This component should increase with increasing axial displacement  $z$  measured from the median plane. The  $z$ -dependence of the magnetic field  $B_r$  can be expressed with a power series with coefficients evaluated at the median plane where their values are constant for a given radius

$$B_r = z \left( \frac{\partial B_r}{\partial z} \right)_{z=0} + \frac{z^2}{2} \left( \frac{\partial^2 B_r}{\partial z^2} \right)_{z=0}. \quad (1.18)$$

According to the Maxwell's equations, in a static magnetic field the curl of  $B$  is zero in regions where there is no current. Therefore, the equation to be satisfied is

$$\left( \frac{\partial B_r}{\partial z} \right)_{z=0} - \left( \frac{\partial B_z}{\partial r} \right)_{z=0} = 0. \quad (1.19)$$

For small values of  $z$  only the first term of equation (1.18) can be taken. Since at  $z = 0$  there is no radial component and  $B_z = B$ , by combining equations (1.18) and (1.19) we obtain the following form of the  $B_r$  component:

$$B_r = \frac{\partial B}{\partial r} z. \quad (1.20)$$

The field index is defined as

$$n = -\frac{r}{B} \frac{\partial B}{\partial r}. \quad (1.21)$$

Therefore, equation (1.21) can be rewritten as

$$B_r = -nB \frac{z}{r}. \quad (1.22)$$

an axial force  $qv_\theta B_r$  acts on a particle deviated by  $z$  from the median plane and moving with a constant velocity  $v_\theta$ . The axial motion of the particle is given by the equation

$$M \frac{d^2 z}{dt^2} = -qv_\theta nB \frac{z}{r}. \quad (1.23)$$

## Chapter 1. Cyclotrons

---

Since the velocity  $v_\theta = \omega r$  and  $M\omega = qB$ , the Kerst-Serber equation for axial betatron motion is obtained [7]

$$\frac{d^2 z}{dt^2} + \omega^2 z n = 0. \quad (1.24)$$

As in the case of the corresponding equation for radial motion, the solution is either  $z = 0$ , representing the axially unperturbed orbit, or a simple harmonic motion for  $n > 0$

$$z = z_0 \sin(\sqrt{n}\omega t), \quad (1.25)$$

where  $z_0$  is the amplitude, and the radian frequency  $\omega_z$  is

$$\omega_z = \omega\sqrt{n}. \quad (1.26)$$

The particle oscillates around the median plane with this frequency and these oscillations are called the *axial betatron oscillations*. The number of such oscillations per turn is called the *axial tune* and is given by:

$$\nu_z = \frac{\omega_z}{\omega} = \sqrt{n}. \quad (1.27)$$

The axial stability condition is therefore fulfilled when the field index  $n$  and consequently the axial tune  $\nu_z$  are bigger than zero.

Summarizing all the considerations regarding orbit stability, it can be concluded that to keep stable orbit the field index must be  $0 < n < 1$ , which is the definition of *weak focusing*. To satisfy this criterion, the magnetic field should slightly decrease radially, as shown in figure 1.3. This is realized by shaping pole tips of a cyclotron magnet. The classical cyclotron worked to some extent due to so called *fringe field effects* resulting in the field index being slightly bigger than 0, which provided a marginal weak focusing.

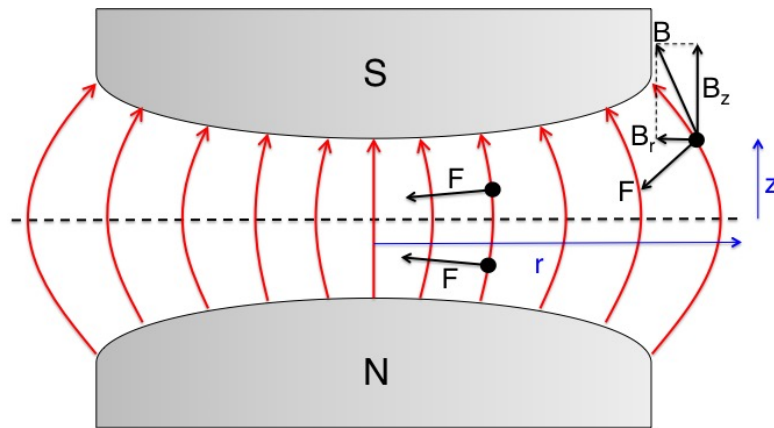


Figure 1.3 – Weak focusing realized by a radially decreasing magnetic field between the poles of a cyclotron magnet.

### 1.2.3 Longitudinal stability

As it has been shown, during acceleration, simultaneous horizontal and vertical stability are needed, therefore, the field index  $n$  should be bounded between 0 and 1. If the magnetic field decreases, the revolution radian frequency  $\omega_{rev}$  also decreases, since  $\omega_{rev} = qB/m$ . Then, a phase difference  $\Delta\varphi$  between the accelerating field phase and the beam builds up such as

$$\Delta\varphi = \pi[(\omega_{RF}/\omega_{rev}) - 1], \quad (1.28)$$

where  $\omega_{RF}$  is the radian frequency of the RF. The isochronous condition (equation (1.6)) is fulfilled only at one radius for the so-called *isochronous bunch*. The focusing condition is not compatible with the isochronism of the machine. The beam extraction should be done before reaching the decelerating phase region. The energy range is limited by the geometry of the cyclotron. Thus the weak focusing does not allow high energies to be produced [8].

Another limiting factor for longitudinal stability is relativity. At higher energies, we have to take into account relativistic effects and equation (1.4) becomes

$$\omega = \frac{qB(r)}{M\gamma(r)}, \quad (1.29)$$

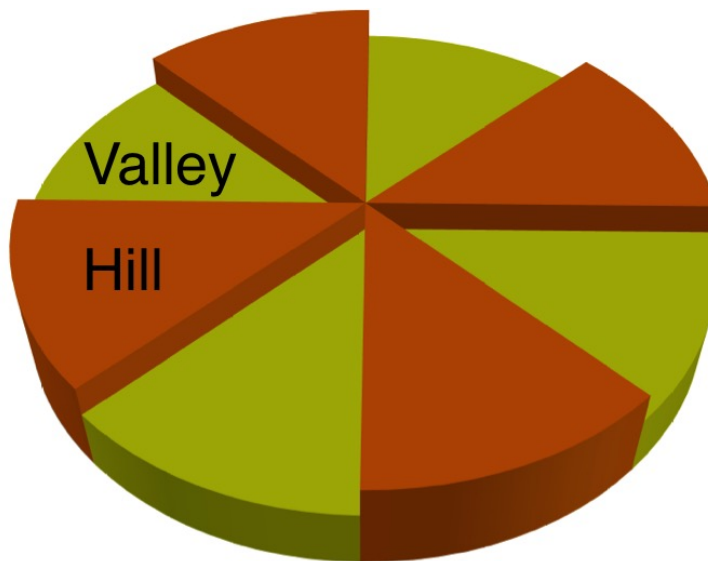


Figure 1.4 – AVF pole tip with sectors to create azimuthal field modulation.

where  $\gamma = 1/\sqrt{1 - v^2/c^2}$  is the Lorentz factor. To keep the radian revolution frequency  $\omega$  constant, the magnetic field  $B(r)$  must increase radially. This translates into a negative field index, which is not compatible with a slightly decreasing field required for weak focusing. Therefore, to keep both longitudinal and transverse stability, another solution is needed. One is so-called synchrocyclotron, in which the RF frequency is varied to keep the synchronism between the beam and the RF. Another alternative is the Azimuthally Varying Field (AVF) cyclotron. Since most modern cyclotrons are AVF machines, the principle of their operation is explained in the next section.

### 1.2.4 Azimuthally varying field cyclotron

The AVF cyclotron is based on pole tips divided in sectors to create azimuthal field modulation for vertical focusing, as presented in figure 1.4. In the pole tips, there is a succession of hills providing a small gap and strong field, and valleys with a large gap and weak field. This produces the  $B_\theta$  field component around the median plane, as shown in figure 1.5. The weak field in the valley induces a large trajectory curvature, while the strong field in the hill results in a small curvature, as shown in figure 1.6. Therefore, the trajectory is not a circle and an orbit is not perpendicular to the hill-valley edge. Thus at the boundary of the sector, the radial component of the particle

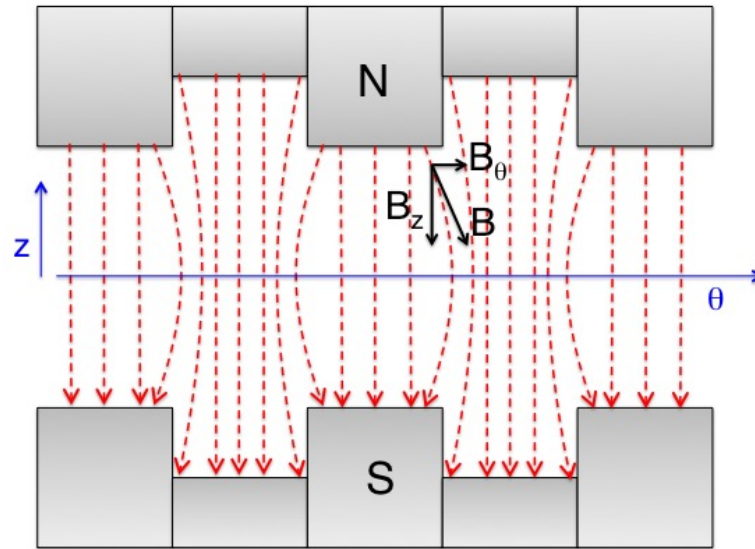


Figure 1.5 – Azimuthal field component  $B_\theta$  created with the AVF pole tips.

velocity  $v_r \neq 0$ . The vertical component  $F_z$  of the Lorentz force at the edge is

$$F_z = q(v_r B_\theta - v_\theta B_r). \quad (1.30)$$

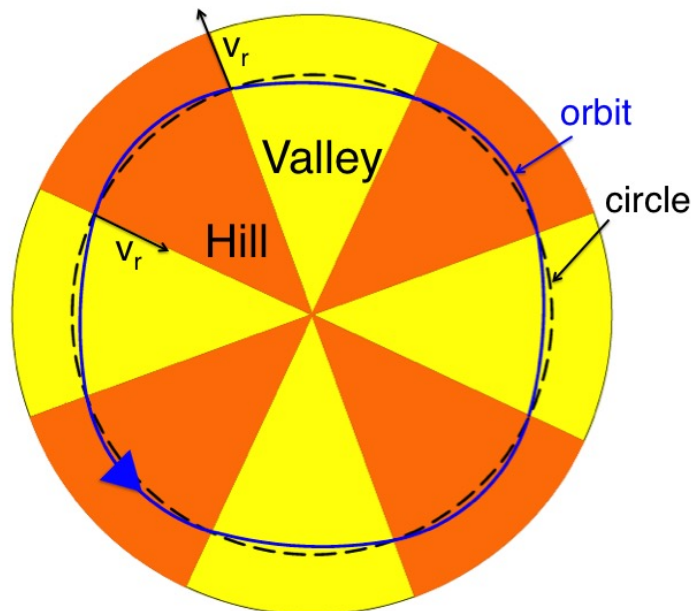


Figure 1.6 – The principle of Thomas focusing,  $v_r \neq 0$  at the boundary of a sector leads to an axial restoring force.

## Chapter 1. Cyclotrons

---

An extra term  $qv_r B_\theta$  represents the so-called *Thomas force*, which always acts towards the median plane, countering the vertical defocusing due to the radial increase in the magnetic field to maintain synchronicity and extend the energy reach of the isochronous cyclotron. This vertical focusing effect is called *Thomas focusing* [9]. To quantify the focusing effect we define *flutter* as

$$F = \frac{\langle B^2 \rangle - \langle B \rangle^2}{\langle B \rangle^2}, \quad (1.31)$$

where  $\langle B \rangle$  is the average magnetic field over one turn. The following relationship between the axial tune  $\nu_z$  and the flutter  $F$  can be derived:

$$\nu_z^2 = n + \frac{N^2}{N^2 - 1} F + \dots, \quad (1.32)$$

where  $n$  is the field index, and  $N$  is the number of sectors of the cyclotron. To fulfill the isochronism condition for a high-energy cyclotron, the average axial magnetic field should radially increase as Lorentz factor  $\gamma$ :

$$\langle B_z(r) \rangle = \gamma(r) \langle B_z(0) \rangle. \quad (1.33)$$

From the last equation and the definition of the field index, we obtain

$$n = 1 - \gamma^2. \quad (1.34)$$

Since for high energy  $\gamma > 1$ , the field index  $n$  is negative and the particle motion is unstable. However, to maintain vertical stability, it is enough to satisfy the condition  $\nu_z > 0$ . The AVF cyclotron allows to do so, since it is characterized by a non-zero flutter. From equation (1.32) we obtain the following condition for vertical stability:

$$\frac{N^2}{N^2 - 1} F > -n = \gamma^2 - 1. \quad (1.35)$$

Practically speaking, the flutter  $F$  of the isochronous cyclotron as described is limited to values near unity. Therefore this kind of cyclotron is still limited in energy. If we consider the acceleration of protons, the maximum achievable energies are about 40-50 MeV. Further extension requires spiral focusing, which allows large cyclotrons

like TRIUMF to reach or exceed 0.5 GeV beam energy.

## 1.3 Medical cyclotrons

The use of cyclotrons for medical applications has a long history. The first ideas came in 1935, only a few years after the invention of the cyclotron. At that time, Lawrence invited his brother, who was a physician, to join him in Berkeley to study beams and their artificial products. Several cyclotron-produced radionuclides were used in studies of physiology and medicine, both in animals and humans. For example, radio-phosphorus-32 was discovered with 27-inch Lawrence cyclotron and used as a tracer to study the absorption and metabolism of phosphorus and cellular regeneration activity. Phosphorus-32 was also administered to a leukemia patient by John Lawrence in 1936, which is considered the beginning of internal radiotherapy. Also in 1936 radioactive sodium-24, obtained at the Berkeley cyclotron, was used to study uptake and transport in animal and human circulatory systems and determine the speed of absorption. In 1937, radioactive sodium was first given to treat leukemia patients [10]. In 1954, the first patient was treated at Berkeley with a 340 MeV proton beam from a 184-inch synchrocyclotron. The first tumor was irradiated with 185 MeV protons at the Uppsala cyclotron [11].

Nowadays, cyclotrons are used daily to produce radioisotopes and for radiation therapy. Special importance is given to the production of isotopes for Positron Emission Tomography (PET). This diagnostic method is used in nearly all large hospitals. Therefore there is a need for large quantities of radiotracers such as fluorodeoxyglucose (FDG) synthesized with cyclotron-produced fluorine-18. Since this is one of the most commonly produced isotopes for medical applications, many medical cyclotrons are designed to provide 18-19 MeV protons to match the optimal cross-section for fluorine-18 production. The use of cyclotrons for radioisotope production is continuously being extended. For instance, technetium-99m, used in approximately 80 % of all the nuclear medicine examinations and usually produced by nuclear reactors, has recently been obtained in large quantities using cyclotrons with maximum energies below 20 MeV [12]. Cyclotrons are also employed in hadrontherapy, a radiation ther-

## **Chapter 1. Cyclotrons**

---

apy modality allowing for a high-precision irradiation of cancer. Machines of different maximum clinical energies are located in hospital-based proton therapy facilities. The number of cyclotrons is therefore continuously growing. According to a survey of the four major medical accelerator manufacturers, in 2010 there were about 700 cyclotrons operating in the world and this number was increasing at a rate of about 7 % per year between 2009 and 2012 [10].

## 2 Transverse beam dynamics

In this chapter, some aspects of transverse beam dynamics, which are relevant to the work presented in this thesis, are discussed. Matrix formalism in linear beam dynamics is introduced to mathematically describe basic elements of beam transport and their influence on a single particle. Phase space and beam emittance are then defined. For a detailed discussion, only the transverse phase plane is considered, since this is directly related to the work presented in this thesis. The influence of the energy spread on the transverse beam dynamics is briefly discussed, as the measurement of the beam energy distribution was a part of my work. Some derivations given in this chapter are based on reference [13].

### 2.1 Beam transport

In this section, basic elements of beam transport lines are discussed, including focusing quadrupoles, and defocusing quadrupoles. A matrix formalism is derived to describe particle trajectories through these components. For this purpose, beam dynamics are treated in the linear approximation. In general, linear magnetic fields for bending and quadrupole magnets are expressed by

$$B_x = -g y, \tag{2.1}$$

$$B_y = B_{y0} + g x, \tag{2.2}$$

## Chapter 2. Transverse beam dynamics

---

where  $B_{y0}$  is the dipole field,  $g$  is the gradient of the quadrupole field, and  $x$  and  $y$  are the transverse particle coordinates. Since bending sections are not considered,  $B_{y0} = 0$ . Therefore I consider a straight trajectory along  $z$ -axis and the following equation of motion:

$$\frac{d\vec{p}}{dt} = q(\vec{v} \times \vec{B}), \quad (2.3)$$

where  $\vec{p} = m\gamma\vec{v}$  is the particle momentum. Thus

$$\frac{d^2x}{dt^2} + \frac{qv_z}{m\gamma}gx = 0, \quad (2.4)$$

$$\frac{d^2y}{dt^2} - \frac{qv_z}{m\gamma}gy = 0. \quad (2.5)$$

It is more convenient to use the slopes  $x' = dx/ds$  and  $y' = dy/ds$ , where  $s = v_z t$  is the distance along  $z$ -axis travelled by the particle. The equations of motion become

$$v_z^2 \frac{d^2x}{ds^2} + \frac{qv_z}{m\gamma}gx = 0, \quad (2.6)$$

$$v_z^2 \frac{d^2y}{ds^2} - \frac{qv_z}{m\gamma}gy = 0. \quad (2.7)$$

In real beams, not all the particles have exactly the same momentum  $p$ . In circular accelerators we define the *reference orbit* or *design trajectory* on which particles have the momentum  $p_0$  and a deviation from this orbit by off-momentum particles is usually defined as  $\delta = \delta p/p_0$ . For our purposes, we can also use the same concept and write the equations of motion for an on-momentum particle ( $p = p_0$ ). Since the longitudinal momentum  $p_z$  is much larger than the transverse components, it is legitimate to use the approximation  $p_0 \approx p_z = m\gamma v_z$ . Therefore, the following equations are obtained:

$$x'' + kx = 0, \quad (2.8)$$

$$y'' - ky = 0, \quad (2.9)$$

where  $k = (q/p_0)g$  is the focusing strength of the quadrupole magnet. In principle  $k$  is  $s$ -dependent, but for the derivation of transport matrices, we can consider a

single piece of the accelerator having constant  $k$ . This is called the *piecewise constant approximation*. By defining

$$k_x = \frac{q}{p_0} \frac{dB_y}{dx}, \quad (2.10)$$

$$k_y = -k_x, \quad (2.11)$$

we obtain homogeneous *Hill's equations of motion*

$$x'' + k_x x = 0, \quad (2.12)$$

$$y'' + k_y y = 0. \quad (2.13)$$

The general form is therefore

$$u'' + k_u u = 0, \quad (2.14)$$

where  $u$  may be used for either  $x$  or  $y$ . The solution is

$$u(s) = C(s)u_0 + S(s)u'_0, \quad (2.15)$$

where for  $k_u > 0$

$$C(s) = \cos(\sqrt{k_u} s), \quad (2.16)$$

$$S(s) = \frac{1}{\sqrt{k_u}} \sin(\sqrt{k_u} s), \quad (2.17)$$

and for  $k_u < 0$

$$C(s) = \cosh(\sqrt{|k_u|} s), \quad (2.18)$$

$$S(s) = \frac{1}{\sqrt{|k_u|}} \sinh(\sqrt{|k_u|} s). \quad (2.19)$$

If we take the derivative of (2.14)

$$u'(s) = \frac{d_u}{ds} = C'(s)u_0 + S'(s)u'_0, \quad (2.20)$$

## Chapter 2. Transverse beam dynamics

---

we can write a general beam transport equation with the transport matrix  $\mathcal{M}$  as

$$\begin{pmatrix} u \\ u' \end{pmatrix} = \begin{pmatrix} C(s) & S(s) \\ C'(s) & S'(s) \end{pmatrix} \begin{pmatrix} u_0 \\ u'_0 \end{pmatrix} = \mathcal{M} \begin{pmatrix} u_0 \\ u'_0 \end{pmatrix}. \quad (2.21)$$

### Drift space

In a drift space of length  $L$ , the focusing parameter  $k_u = 0$ . To derive the transport matrix  $\mathcal{M}_{DR}$  for a drift space, we take the limit  $k_u \rightarrow 0$  of the matrix  $\mathcal{M}$ , and we obtain

$$\mathcal{M}_{DR} = \begin{pmatrix} 1 & L \\ 0 & 1 \end{pmatrix}. \quad (2.22)$$

We can see the expected properties of a particle trajectory in a field free drift space. The amplitude  $u$  changes only if the trajectory has an original non-vanishing slope  $u'_0 \neq 0$  while the slope itself does not change.

### Focusing quadrupole

A quadrupole magnet is shown in figure 2.1. The quadrupole in the figure is focusing in the vertical plane and defocusing in the horizontal one. A focusing effect is obtained for  $k_u > 0$ . The transport matrix  $\mathcal{M}_{QF}$  for a focusing quadrupole of length  $L$  is therefore

$$\mathcal{M}_{QF} = \begin{pmatrix} \cos(\sqrt{k_u}L) & \frac{1}{\sqrt{k_u}} \sin(\sqrt{k_u}L) \\ -\sqrt{k_u} \sin(\sqrt{k_u}L) & \cos(\sqrt{k_u}L) \end{pmatrix}. \quad (2.23)$$

### Defocusing quadrupole

A defocusing effect is obtained for  $k_u < 0$ . The transport matrix  $\mathcal{M}_{QD}$  for a defocusing quadrupole of length  $L$  is therefore

$$\mathcal{M}_{QD} = \begin{pmatrix} \cosh(\sqrt{|k_u|}L) & \frac{1}{\sqrt{|k_u|}} \sinh(\sqrt{|k_u|}L) \\ \sqrt{|k_u|} \sinh(\sqrt{|k_u|}L) & \cosh(\sqrt{|k_u|}L) \end{pmatrix}. \quad (2.24)$$

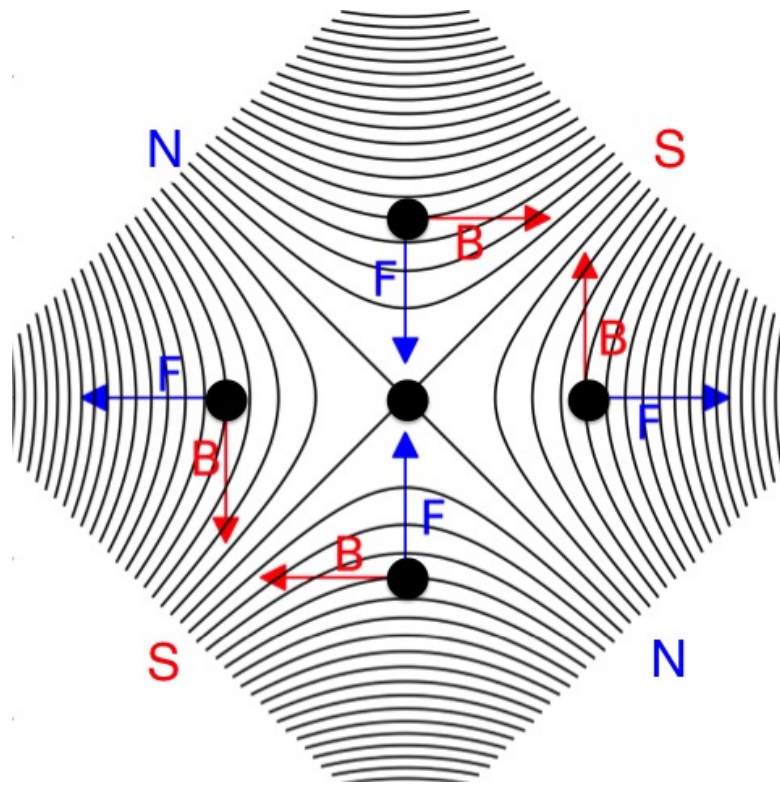


Figure 2.1 – Quadrupole magnet focusing in the vertical plane and defocusing in the vertical plane.

Sometimes, when the length of the quadrupole is small compared to its focal length ( $L \ll f$ ) and it is desirable to calculate the approximate properties of a set of beam elements analytically, the *thin lens approximation* is used. If we let the length of the quadrupole approach zero,  $L \rightarrow 0$ , while keeping the focal length constant as  $1/f = k_u L = \text{const}$ , the matrix  $\mathcal{M}_Q$  for quadrupoles becomes

$$\mathcal{M}_Q = \begin{pmatrix} 1 & 0 \\ \mp \frac{1}{f} & 1 \end{pmatrix}, \quad (2.25)$$

where a negative (positive) sign corresponds to focusing (defocusing).

In defining the transport matrix through a quadrupole, we assumed the strength parameter  $k_u(z)$  to be a step function with a constant non-zero value within the quadrupole and zero outside. In a real quadrupole magnet the strength parameter varies in a gentle way from zero outside the magnet to a maximum value in the middle

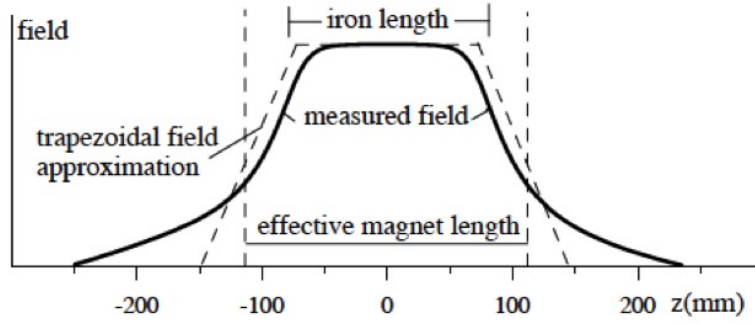


Figure 2.2 – Field profile in a real quadrupole [13].

of the quadrupole, as shown in figure 2.2. As a result, on both sides of the magnet iron, we observe a non-zero *fringe field*. To take this into account in beam transport calculations, we should always consider the *effective magnetic length* rather than iron length. It is defined as

$$l_{eff} = \frac{\int g dz}{g_0}, \quad (2.26)$$

where  $g_0$  is the field gradient in the middle of the quadrupole. We can approximate the real field by a trapezoid such that  $\int g dz$  is the same (figure 2.2). This leads to an approximated value of the iron length

$$l_{eff} \approx l_{iron} + R, \quad (2.27)$$

where  $l_{iron}$  is the iron length and  $R$  is the radius of the bore aperture.

The matrix formalism allows for a simple calculation of the particle trajectory through the whole beam transport line. For a sequence of  $n$  beamline elements given by the matrices  $\mathcal{M}_1, \mathcal{M}_2, \dots, \mathcal{M}_n$ , the transport matrix  $\mathcal{M}$  for the whole beamline is

$$\mathcal{M} = \mathcal{M}_n \dots \mathcal{M}_2 \mathcal{M}_1. \quad (2.28)$$

## 2.2 Transverse beam emittance

In order to know more about the collective motion of particles, their dynamics in phase space is observed. Each particle at any point along a beam transport line is represented by a point in six-dimensional phase space with coordinates  $(x, p_x, y, p_y, \sigma, E)$ , where  $p_x \approx x' p_0$  and  $p_y \approx y' p_0$  are the transverse momenta with  $p_0 = \beta E_0$ ,  $E_0$  is the energy of an on-momentum particle,  $\sigma$  is the coordinate along trajectory, and  $E$  is the particle energy. The horizontal and vertical planes are considered decoupled in linear beam dynamics or the coupling is treated as a perturbation as is the one between transverse and longitudinal motion. We can therefore split the six-dimensional phase space into three independent two-dimensional phase planes.

Particles in a beam occupy a certain region in phase space. Its area divided by  $\pi$  is called *beam emittance* and we define three independent two-dimensional beam emittances. Beam emittance is a measure of the transverse and longitudinal temperature of the beam and is the main physical quantity used to characterize an accelerated particle beam. It depends on the source characteristics and many other effects, being a unique parameter of any particle accelerator. Since this thesis concentrates on the transverse beam emittance, only the two transverse phase planes are considered. Due to complete equivalence of both planes, it is enough to discuss only the horizontal one defined as

$$\varepsilon_x = \frac{1}{\pi} \int_A dx dx', \quad (2.29)$$

where  $A = \pi \varepsilon$  is the area of the phase space occupied by the beam, as shown in figure 2.3. Beam emittance is usually given in mm·mrad. According to *Liouville's theorem* it is a constant of motion if there is no acceleration and we assume the absence of any non-linear coupling, like space charge forces or beam-beam effects. A determination of the emittance is equivalent to the determination of the distribution of the spatial coordinate  $x$  (i.e. the beam profile), the distribution in angle  $x'$ , and the correlation between  $x$  and  $x'$ . In a more realistic case, the distribution is not hard-edge and homogeneous. If we consider a Gaussian density distribution  $\rho(x, x')$ , the value

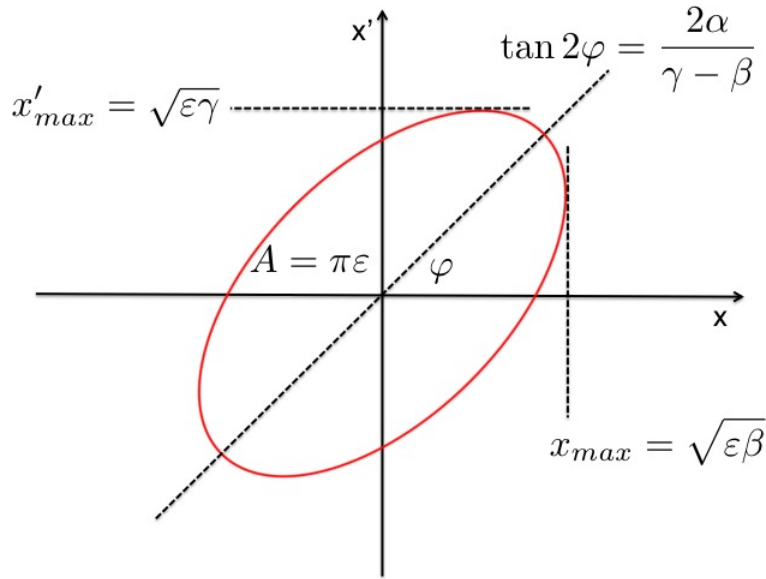


Figure 2.3 – Phase space ellipse of the area  $A = \pi\epsilon$ , where  $\epsilon$  is the beam emittance.

of the emittance is given by

$$\epsilon_x = \frac{1}{\pi} \int_{-\infty}^{\infty} \int_{-\infty}^{\infty} \rho(x, x') dx dx' \quad (2.30)$$

and includes 100 % of the particles. In practice, only a fraction of the beam can be considered and thus a reliable statistical approach is needed. In the case of an arbitrary density distribution  $\rho(x, x')$ , the following moments can be defined:

$$\langle x^2 \rangle = \frac{\iint (x - \mu)^2 \rho(x, x') dx' dx}{\iint \rho(x, x') dx' dx} \quad (2.31)$$

$$\langle x'^2 \rangle = \frac{\iint (x' - \mu')^2 \rho(x, x') dx' dx}{\iint \rho(x, x') dx' dx}, \quad (2.32)$$

and the covariance

$$\langle xx' \rangle = \frac{\iint (x - \mu)(x' - \mu') \rho(x, x') dx' dx}{\iint \rho(x, x') dx' dx}, \quad (2.33)$$

where  $\mu$  and  $\mu'$  are the expectation values for  $x$  and  $x'$ , respectively. We define the

## 2.2. Transverse beam emittance

beam matrix  $\sigma(s)$  at the location  $s$  along the beam transport line

$$\sigma(s) = \begin{pmatrix} \sigma_{11} & \sigma_{12} \\ \sigma_{21} & \sigma_{22} \end{pmatrix} = \begin{pmatrix} \langle x^2 \rangle & \langle xx' \rangle \\ \langle xx' \rangle & \langle x'^2 \rangle \end{pmatrix}. \quad (2.34)$$

Then, the *Root-Mean-Square (RMS) beam emittance*  $\varepsilon_{rms}$  is given by the determinant of the  $\sigma(s)$  matrix

$$\varepsilon_{rms} = \sqrt{\det(\sigma(s))}. \quad (2.35)$$

For a Gaussian distribution, the RMS emittance corresponds to the area  $\pi\varepsilon_{rms}$  including 39 % of the beam. In the case of a well known distribution, the beam coverage can be easily extended. In the case of Gaussian distribution,  $n - \sigma$  emittances, where  $\sigma$  is the standard deviation, are often evaluated. However, typically beams are far from any well defined distribution. Therefore the RMS emittance is the most convenient way to characterize such beams.

Frequently the *Twiss parameters* [14] are used, which are the beam matrix elements normalized by the emittance as

$$\alpha = -\frac{\sigma_{12}}{\varepsilon} = -\frac{\sigma_{21}}{\varepsilon}, \quad (2.36)$$

$$\beta = \frac{\sigma_{11}}{\varepsilon}, \quad (2.37)$$

$$\gamma = \frac{\sigma_{22}}{\varepsilon}. \quad (2.38)$$

The beam matrix can be expressed by these parameters as

$$\sigma = \varepsilon \begin{pmatrix} \beta & -\alpha \\ -\alpha & \gamma \end{pmatrix}. \quad (2.39)$$

The equation of the beam ellipse (figure 2.3) can be written as

$$\gamma x^2 + 2\alpha xx' + \beta x'^2 = \varepsilon, \quad (2.40)$$

where  $\beta\gamma - \alpha^2 = 1$ . The RMS-widths of the beam profile and the angular distribution are

## Chapter 2. Transverse beam dynamics

---

$x_{rms} = \sqrt{\varepsilon_{rms}\beta}$  and  $x'_{rms} = \sqrt{\varepsilon_{rms}\gamma}$ , respectively. In the case of a Gaussian distribution, they correspond to one standard deviation of the transverse profile and angular distribution of the beam. The geometrical size of the phase space ellipse changes along the beam path. Therefore the parameters  $\alpha(s)$ ,  $\beta(s)$ , and  $\gamma(s)$  are functions of the position  $s$ . The function  $\beta(s)$  is frequently used to describe the beam as a whole. The *beam envelope* is defined as

$$E(s) = \pm\sqrt{\varepsilon}\sqrt{\beta(s)}, \quad (2.41)$$

where the choice of the  $\varepsilon$  definition determines the fraction of the beam in the envelope. The two signs indicate that there is an envelope on either side of the beam center.

During transport through a beamline, the phase space ellipse changes its orientation and eccentricity, while the area remains constant. In a drift space, the ellipse becomes distorted in a clockwise direction without changing the slope of any particle, as shown in figure 2.4. The beam width becomes larger or smaller for a divergent or convergent beam, respectively. The width of the angular distribution remains constant. During the process of focusing, the phase space ellipse rotates anti-clockwise and slopes of particle trajectories reverse signs, forming a converging beam, as shown in figure 2.5. In the same figure, we can see that when the beam continues to drift downstream from the focusing section a clockwise distortion is again observed. At a certain location along the beamline it reaches the minimum width (beam waist) and after this point becomes divergent again.

In order to keep track of the phase space ellipse during the beam transport, it is convenient to use the previously defined beam matrix in equation 2.34. A beam matrix  $\sigma$  contains all the information to reconstruct the phase space. The beam matrix  $\sigma(s)$  at any location  $s$  along the beamline, starting at  $s_0$ , is given by the formula [15]:

$$\sigma(s) = \mathcal{M}\sigma(s_0)\mathcal{M}^T, \quad (2.42)$$

where  $\mathcal{M}$  is the beam transport matrix. It can represent a single beamline element or a set of elements, as shown in equation (2.28). Each element is represented by a matrix

## 2.2. Transverse beam emittance

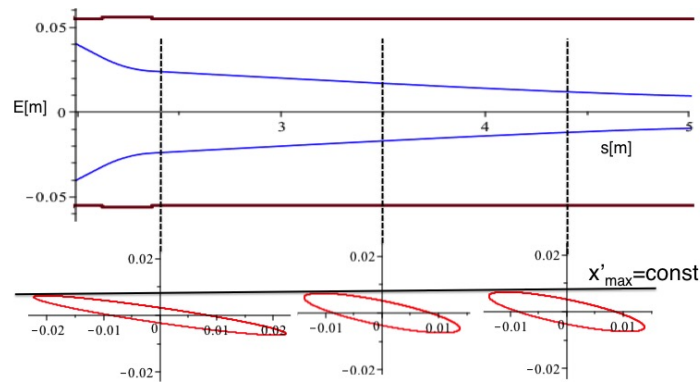


Figure 2.4 – Transformation of a phase space ellipse at different locations along a drift section.

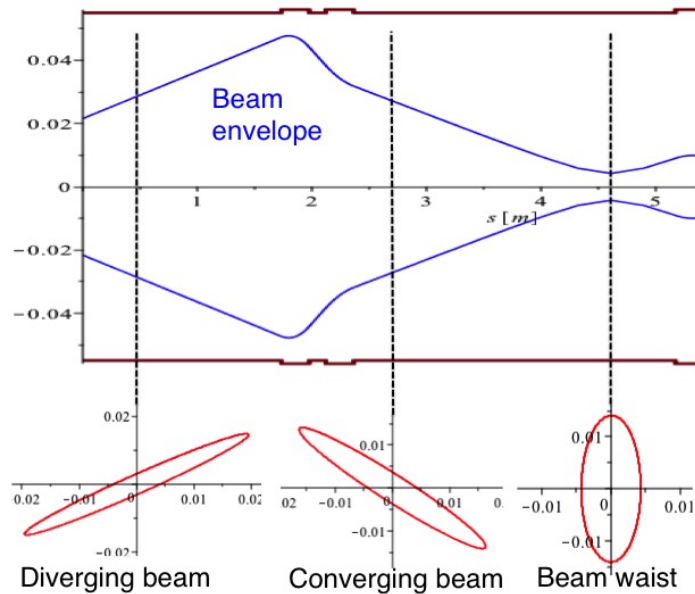


Figure 2.5 – Transformation of a phase space ellipse due to focusing. The initial beam is focused and drifts downstream from the focusing section.

of the same form, as in the case of particle trajectory tracking. If a beam matrix at a location  $s$  is known, the phase space at the initial point can always be reconstructed by computing the  $\sigma(s_0)$  matrix in the following way:

$$\sigma(s_0) = \mathcal{M}^{-1} \sigma(s) (\mathcal{M}^T)^{-1}. \quad (2.43)$$

This formalism is especially significant for the methods of beam emittance measurement employed in the beam dynamics study presented later in this thesis.

### 2.3 Energy spread and its influence on the transverse beam dynamics

In general, due to many reasons, not all the particles have exactly the same energy  $E$  or, consequently, the momentum  $p$ . The ideal particle has energy  $E_0$  and momentum  $p_0$ . Off-momentum particles undergo different bending by dipole magnets and influence the focusing strength  $k$  of the quadrupoles. The former is not considered here, since beam dynamics in this thesis are studied only in a straight beamline. The latter is often called *chromatic aberration* [16]. The focusing strength of a quadrupole is a function of its momentum

$$k = \frac{q}{p}g, \quad (2.44)$$

where  $g$  is the field gradient. If we consider a fractional energy spread  $\Delta E/E_0$  and corresponding fractional momentum spread often defined as

$$\delta = \frac{p - p_0}{p_0} = \frac{\Delta p}{p_0}, \quad (2.45)$$

we can conclude that

$$\frac{\Delta k}{k_0} = -\frac{\delta}{1 + \delta}, \quad (2.46)$$

where  $k$  is the nominal quadrupole strength for an on-momentum particle. Since  $\delta \ll 1$

$$\frac{\Delta k}{k_0} \approx -\delta = -\frac{\Delta p}{p_0}. \quad (2.47)$$

Based on this fact, I performed a calculation showing the influence of the momentum spread on the beam width. Let us consider a focusing quadrupole of length  $L$  and nominal focusing strength  $k_0$ . For simplicity, we can use the thin lens approximation.

### 2.3. Energy spread and its influence on the transverse beam dynamics

---

The transport matrix of such a beamline element is

$$\mathcal{M} = \begin{pmatrix} 1 & \frac{L}{2} \\ 0 & 1 \end{pmatrix} \begin{pmatrix} 1 & 0 \\ -k_0 L & 1 \end{pmatrix} \begin{pmatrix} 1 & \frac{L}{2} \\ 0 & 1 \end{pmatrix} = \begin{pmatrix} 1 - \frac{k_0 L^2}{2} & L \left(1 - \frac{k_0 L^2}{4}\right) \\ -k_0 L & 1 - \frac{k_0 L^2}{2} \end{pmatrix}. \quad (2.48)$$

Let  $x_{0,max} > 0$  and  $x'_{0,max}$  be the position and slope of a particle traveling on the boundary of a beam envelope, respectively. In this case,  $x_{0,max}$  is a measure of the beam width. The particle enters the focusing section described by the matrix  $\mathcal{M}$ . If it is an on-momentum particle, its final position is

$$x = \left(1 - \frac{k_0 L^2}{2}\right) x_{0,max} + L \left(1 - \frac{k_0 L^2}{4}\right) x'_{0,max}. \quad (2.49)$$

The final position of an off-momentum particle, characterized by a deviation  $\delta$ , is

$$x_\delta = \left(1 - \frac{k_0 L^2}{2} + \frac{k_0 \delta L^2}{2}\right) x_{0,max} + L \left(1 - \frac{k_0 L^2}{4} + \frac{k_0 \delta L^2}{4}\right) x'_{0,max}. \quad (2.50)$$

Thus the difference  $\Delta x$  due to the momentum deviation  $\delta$  is

$$\Delta x = x_\delta - x = \delta \frac{k_0 L^2}{2} \left( x_{0,max} + \frac{1}{2} L x'_{0,max} \right). \quad (2.51)$$

$\Delta x$  is positive for a particle of the momentum  $p > p_0$  ( $\delta > 0$ ), and negative for  $p < p_0$  ( $\delta < 0$ ). Therefore, in the former case, an increase of the beam width is observed, since we consider the outermost ray in the envelope with the highest momentum  $p_0 + \Delta p$ . The latter case does not necessarily lead to a decrease of the beam width because other nearby rays may have higher momenta. For a defocusing quadrupole, the strength  $k$  in the beam matrix  $\mathcal{M}$  must be replaced with  $-k$ . Then  $\Delta x$  is

$$\Delta x = -\delta \frac{k_0 L^2}{2} \left( x_{0,max} + \frac{1}{2} L x'_{0,max} \right), \quad (2.52)$$

and the conclusion is exactly the opposite. An increase of the beam width is observed, when considering a particle with momentum  $p = p_0 - \Delta p$  ( $\delta < 0$ ).

These considerations are useful to more precisely simulate a beam envelope in a beam transport line, if the energy spread is large. For instance, the beam energy distribution

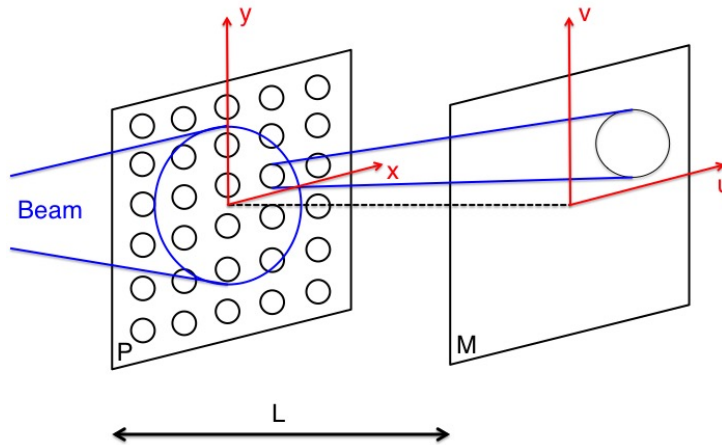


Figure 2.6 – Illustration of the “pepper-pot” method to measure transverse beam emittance.

can be measured. As an energy of the ideal particle, the mean beam energy is taken  $E_0 = \langle E \rangle$ , while  $|\Delta E|$  represents an RMS of the distribution. On this basis,  $|\Delta p/p_0|$  can be calculated. While simulating the beam envelope, at focusing quadrupoles  $p = p_0 + \Delta p$  should be considered, whereas at defocusing quadrupoles  $p = p_0 - \Delta p$ . This allows the predicted beam widths to be corrected, at least to some extent, for the energy spread of the simulated beam.

## 2.4 Methods of transverse emittance measurements

In this section, three methods of transverse beam emittance measurements are discussed. The “pepper-pot” technique is described as one of the mostly used method for a direct measurement of both the spatial and angular distributions of the beam. The quadrupole strength variation is presented, since this method was used for some measurements reported in this thesis. Eventually, the use of multiple beam profilers is described and its advantages are discussed, as the system for online beam emittance measurement, developed in the framework of my PhD, is based on this method. This section is partially based on references [15, 17, 18].

### 2.4.1 The “pepper-pot” technique

In this technique, the beam is collimated by a “pepper-pot plate” into a small beamlets, as shown in figure 2.6. The intensity of each beamlet as a function of the position of the origin-hole gives information on a spatial beam profile. The beam monitor  $M$  is located at a distance  $L$  from the “pepper-pot plate”  $P$  (figure 2.6). If a particle is known to pass through the point  $(x, y)$  on  $P$  and strike  $M$  at the point  $(u, v)$ , the slopes of the particle’s path with respect to the optical axis are given by

$$x' = (u - x) / L, \tag{2.53}$$

$$y' = (v - y) / L. \tag{2.54}$$

Thus the beamlet spatial profiles in  $(u, v)$  are a direct measurement of the angular distribution of the beam sampled at  $(x, y)$ . From the “pepper-pot” image the emittance can be extracted by fitting an ellipse, if the beam is assumed to be Gaussian. One advantage of the method is that the shape of the beam in the  $x - x'$  and  $y - y'$  phase spaces can be determined explicitly and an emittance plot showing contours of constant beam intensity can be generated for each. The precision of the measurement depends on the hole size, the spacing between them, and the plate thickness. However, it is difficult to find the optimal conditions. For example, the spatial distribution is best determined by sampling the beam at small intervals (minimum hole spacing) but the angular distribution is more precisely determined as the spatial profiles of the non-overlapping beamlets get larger, maximizing the spacing.

### 2.4.2 Quadrupole variation

This method is based on the variation of the quadrupole strength. Either type of quadrupole, focusing or defocusing, is followed by a drift space  $L$  before reaching a beam monitor. The beam transport matrix is therefore

$$\mathcal{M}(k) = \mathcal{M}_{DR} \mathcal{M}_Q(k), \tag{2.55}$$

## Chapter 2. Transverse beam dynamics

---

where  $\mathcal{M}_{DR}$  is the drift space  $L$ , and  $\mathcal{M}_Q(k)$  is the quadrupole set at the strength  $k$ . The matrix  $\mathcal{M}(k)$  provides a linear transformation between the beam matrix  $\sigma(s_0)$  at the entrance to the quadrupole and the beam matrix  $\sigma(s_1, k)$  at the location of the beam monitor. The matrix  $\sigma(s_1, k)$  is obtained by

$$\sigma(s_1, k) = \mathcal{M}(k)\sigma(s_0)\mathcal{M}(k)^T, \quad (2.56)$$

which gives the  $\sigma_{11}(s_1, k)$  component as a function of  $k$ , containing three unknown parameters  $\sigma_{11}(s_0)$ ,  $\sigma_{22}(s_0)$ , and  $\sigma_{12}(s_0) = \sigma_{21}(s_0)$ . It holds:

$$\sigma_{11}(s_1, k) = f(k; \sigma_{11}(s_0), \sigma_{12}(s_0), \sigma_{22}(s_0)). \quad (2.57)$$

A set of beam profile measurements for different strengths of the quadrupole allows a set of values  $\sigma_{11}(s_1, k)$  to be determined. The components of the beam matrix  $\sigma(s_0)$  at the entrance to the quadrupole and the corresponding transverse beam emittance value are obtained by performing a fit of the function  $f(k; \sigma_{11}(s_0), \sigma_{12}(s_0), \sigma_{22}(s_0))$  to the data points. This method requires a good knowledge of the quadrupole characteristics. The strength  $k$  is usually changed by setting a different quadrupole current. Therefore, an understanding of the relationship between the magnet current and the field gradient is necessary.

### 2.4.3 Use of multiple beam profilers

In principle, the simplest method is to use multiple beam profilers. The more beam monitors are used, the better precision is obtained, since each profiler increases the number of degrees of freedom. A minimum of three detectors is needed, but using four guarantees one degree of freedom, and allows uncertainties to be estimated. With respect to quadrupole variation, this method does not require any prior knowledge of the optical elements of the beamline. Beam profiles are measured at a few successive locations around a beam waist separated by a drift length  $L$ . From each profile, an estimate of  $\sigma_{11}(s)$  component of the beam matrix  $\sigma(s)$  at the location  $s$  is performed.

## 2.4. Methods of transverse emittance measurements

---

The beam transfer matrix  $\mathcal{M}(s)$  involves now only a drift:

$$\mathcal{M}(s) = \begin{pmatrix} 1 & s \\ 0 & 1 \end{pmatrix}. \quad (2.58)$$

The beam matrix at any location  $s$  with respect to the location of the first profiler ( $s_0 = 0$ ) is therefore given by the formula:

$$\sigma(s) = \mathcal{M}(s)\sigma(0)\mathcal{M}(s)^T. \quad (2.59)$$

From equation (2.59) it can be derived that  $\sigma_{11}(s)$  is a quadratic function of  $s$ :

$$\begin{aligned} \sigma_{11}(s) &= \sigma_{22}(0)s^2 + 2s\sigma_{12}(0) + \sigma_{11}(0) \\ &= f(s; \sigma_{11}(0), \sigma_{12}(0), \sigma_{22}(0)), \end{aligned} \quad (2.60)$$

where  $\sigma_{11}(0)$ ,  $\sigma_{12}(0)$ , and  $\sigma_{22}(0)$  are the components of the  $\sigma(0)$  matrix. These components, and consequently the transverse emittance, are evaluated by fitting the  $f(s; \sigma_{11}(0), \sigma_{12}(0), \sigma_{22}(0))$  function using the data points representing the estimated variance values as a function of the location  $s$ . This method works best if the beam comes to a waist (a point of minimum spatial extent, where  $\sigma_{12} = 0$ ), somewhere between the first and last monitors. The closer one of the monitors is to a waist, the better.



## 3 The 18 MeV Bern medical cyclotron

In this chapter, the Bern medical cyclotron is presented. Machine characteristics are provided and the specifically designed beamline is described. The last section is devoted to low current beams. I report there on a method, developed with my contribution, to obtain stable beams of intensities down to  $pA$  range, opening the way for multidisciplinary scientific activities not usually performed with this kind of accelerator.

The Bern cyclotron laboratory is located in the campus of Bern University Hospital (Inselspital). The facility is part of the SWAN (SWiss hAdroN) project initiated in 2007 by Inselspital and the University of Bern, which aims to foster a combined center for radioisotope production, proton therapy and multi-disciplinary research located in Bern [19]. The cyclotron laboratory was built in 2011 and was fully operational from 2013. It serves two main purposes. The first is the production of PET radiotracers for healthcare institutions, using the most modern industrial technologies<sup>1</sup>. The second is to carry out multi-disciplinary research. The Beam Transport Line (BTL) was conceived to support scientific activities running in parallel with the daily radioisotope production [20].

---

<sup>1</sup>Good Manufacturing Practice (GMP) certificate obtained in 2013

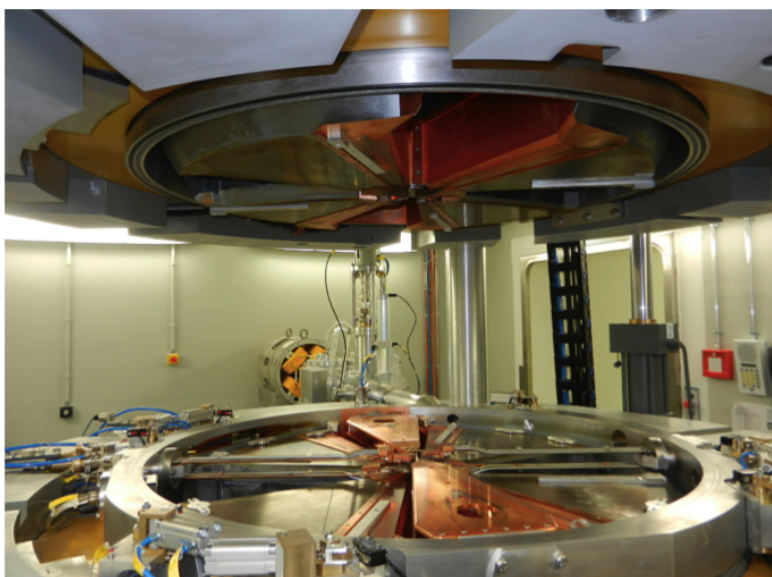


Figure 3.1 – The Bern medical cyclotron opened during maintenance.

### 3.1 Machine characteristics

The Bern cyclotron laboratory hosts the IBA Cyclone 18 MeV cyclotron, shown in figure 3.1. The machine is equipped with two  $H^-$  sources. The negative ions are accelerated to the nominal energy of 18 MeV and stripped by means of  $5\ \mu\text{m}$  thick pyrolytic carbon foils [21]. This kind of extraction is a simple solution and guarantees a very high extraction efficiency. The stripper, as shown in figure 3.2, comprises a rotating carousel and two metallic forks, each holding one stripper foil. The rotation of the carousel allows the beam to be optimized and a damaged stripper foil (figure 3.2) to be changed without opening the cyclotron. Protons can be extracted into one of eight outputs. In dual beam mode, the beam is extracted by two strippers located at an angular distance of approximately 180 degrees. Dual beam mode is only used for PET radioisotope production. The cyclotron provides large beam currents of up to 150 A in either single or dual beam mode. It is also able to accelerate  $D^-$  ions to an energy of 9 MeV. However, this remains an option, since a redundancy of the  $H^-$  sources aims at maximizing the efficiency of the daily production of radioisotopes. A summary of the main technical characteristics is given in table 3.1 [22].

The machine is an AVF cyclotron. It consists of four  $60^\circ$ -sectors with high magnetic

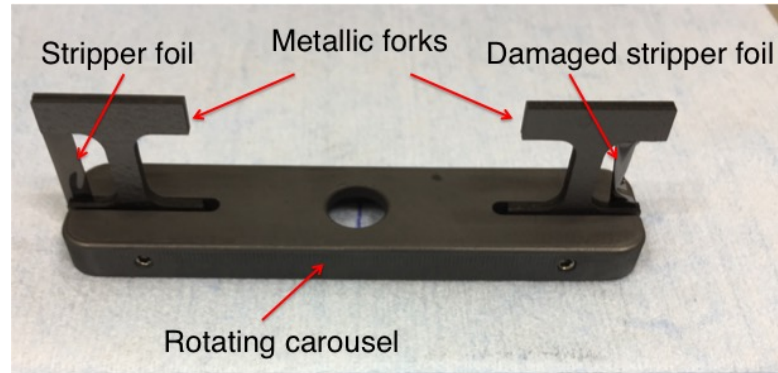


Figure 3.2 – A stripper disassembled from the Bern cyclotron. The main components and a damaged stripper foil are highlighted.

Constructor	Ion Beam Application (IBA), Belgium
Type	Cyclone 18/18 HC
Accelerated particles	H <sup>-</sup> (D <sup>-</sup> possible)
Energy	18 MeV (9 MeV for D <sup>-</sup> )
Maximum current	150 $\mu$ A (40 $\mu$ A for D <sup>-</sup> )
Number of sectors	4
Angle of the dees	30°
Magnetic field	1.9 T (hills) and 0.35 T (valleys)
Radio-frequency	42 MHz
Weight	24000 kg
Dimensions	2 m diameter, 2.2 m height
Ion sources	2 internal PIG H <sup>-</sup>
Extraction ports	8 (one of which connected with the BTL)
Extraction	Carbon foil stripping
Strippers	Two per extraction port on rotating carrousel
Isotope production targets	4 <sup>18</sup> F <sup>-</sup> , <sup>15</sup> O, NIRTA solid target

Table 3.1 – Main characteristics of the Bern medical cyclotron [22].

field (hills) and four 30°-sectors with low magnetic field (valleys). The cyclotron frequency  $\nu_c$  is determined by an average field  $\langle B \rangle$  of 1.4 T to be

$$\nu_c = \frac{1}{2\pi} \frac{q\langle B \rangle}{m} = \frac{1}{2\pi} \frac{e \cdot 1.4 \text{ T}}{938 \text{ MeV}/c^2} \approx 21 \text{ MHz.} \quad (3.1)$$

Acceleration in this cyclotron is realized in four accelerating gaps located at the boundaries of two RF cavities, as shown in figure 3.3. The RF cavities are also traditionally called *dees*. If we consider a particle accelerated by a potential  $V(t) = V_0 \sin(2\pi\nu_{RF}t)$ , we can conclude that at the instant when the particle is passing through Gap 1, the

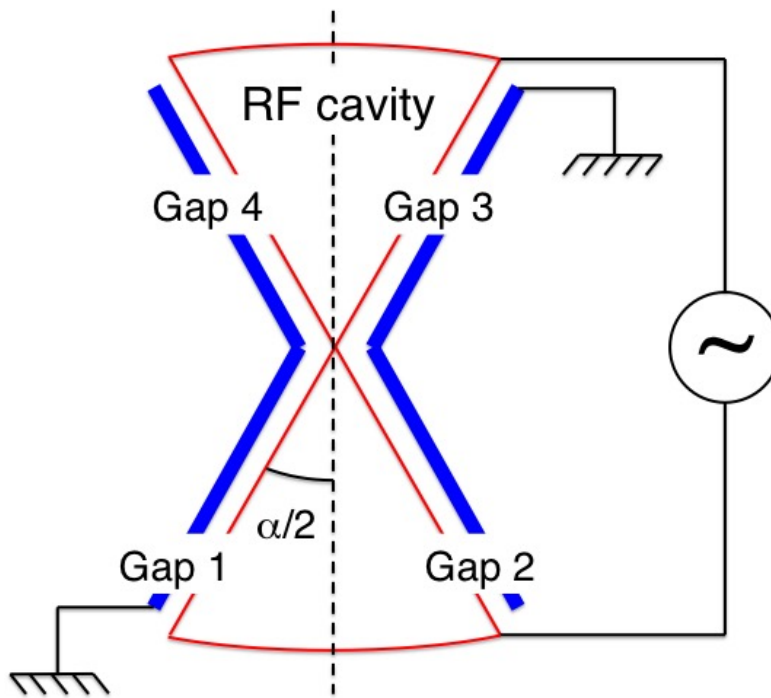


Figure 3.3 – RF cavities and accelerating gaps.

accelerating RF voltage must be positive there and negative in Gap 2. Moreover, to accelerate the particle again in Gap 3, the time which the particle took to travel from Gap 1 to Gap 3 must be equal to an integer number of full RF periods. This leads to the condition

$$\frac{n}{\nu_{RF}} = \frac{1}{2\nu_c} \quad n = 1, 2, \dots, \quad (3.2)$$

where  $\nu_{RF}$  is the desired RF frequency and  $\nu_c$  is the cyclotron frequency. From this equation we obtain

$$\nu_{RF} = 2n\nu_c = h\nu_c \quad h = 2, 4, \dots \quad (3.3)$$

Therefore only even harmonics of the cyclotron frequency can be used. In the case of the Bern cyclotron, the RF system operates in the second harmonic mode and the RF frequency is  $\nu_{RF} = 42$  MHz. The accelerating potential can be rewritten as a function

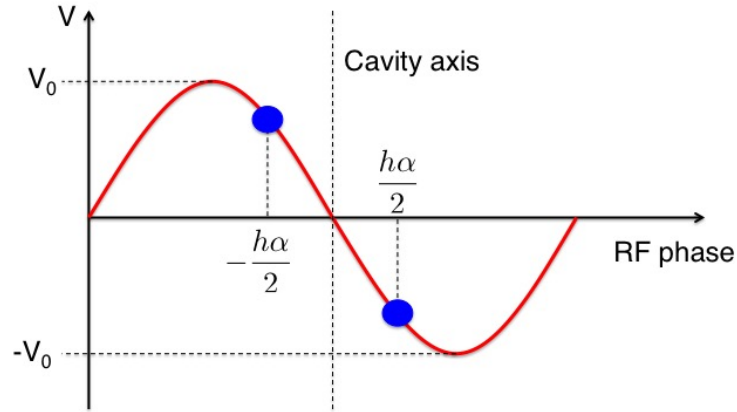


Figure 3.4 – RF voltage as a function of the RF phase within an RF cavity.

of the RF phase  $\varphi$

$$V(\varphi) = V_0 \sin\left(2\pi h\nu_c \frac{\varphi}{2\pi\nu_c}\right) = V_0 \sin(h\varphi). \quad (3.4)$$

The maximum energy gain is obtained when the accelerating voltage is anti-symmetrical within the RF cavity, as shown in figure 3.4. Thus, for  $N$  accelerating gaps and the RF peak voltage  $V_0$ , the energy gain per turn  $\Delta E$  of an ion with the charge  $q$  is

$$\Delta E = NqV_0 \sin\left(h\frac{\alpha}{2}\right). \quad (3.5)$$

In the Bern cyclotron, with a RF peak voltage of 30 kV, this leads to an energy gain per turn of 60 keV and 100 keV for  $H^-$  and  $D^-$  ions, respectively. These values correspond to 300 and 90 turns to reach the extraction energy for  $H^-$  and  $D^-$  ions, respectively.

The  $H^-$  ion source of the Bern cyclotron is an internal cold-cathode Penning Ionization Gauge (PIG) source [23]. It consists of two opposing cathodes and a surrounding cylindrical anode (chimney) with a small aperture called the slit, as shown in figure 3.5. The cathodes emit the electrons which ionize the hydrogen gas and create the plasma. The cyclotron magnetic field is along the axis of the anode and enhances confinement of the electrons in the plasma and therefore the level of ionization of the gas. The electrons oscillate between the two cathodes and move on a spiral trajectory around the vertical magnetic field. The arc current is initiated by raising the cathode voltage to a few kV. Once a plasma exists, the cathodes are self-heated by ionic bombardment

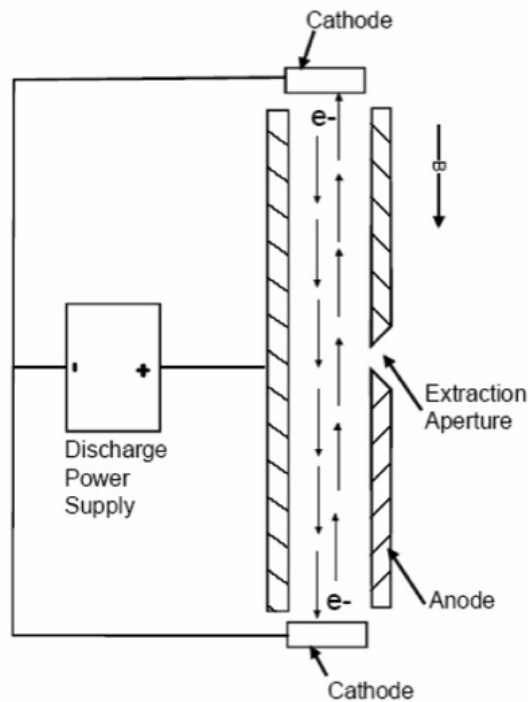


Figure 3.5 – Schematic drawing of a cold-cathode PIG ion source [23].

and the arc voltage decreases with increasing arc current. Usually, an operating voltage of a few hundred volts is obtained, which is enough to ionize the gas atoms. Due to the high electron bombardment in the central region of the plasma, which prohibits the weak-bonded  $H^-$  ions from remaining stable, these ions mainly exist in the plasma's periphery near the slit. They are extracted from the source via the slit by means of the electric field that exists in between the chimney and the so-called puller. This puller is at the same electric potential as the RF accelerating structure as it is mechanically connected to the RF cavities.

### 3.2 Beam transport line

The Beam Transport Line (BTL) of the Bern cyclotron has been designed to carry out multi-disciplinary research in parallel with daily radioisotope production, which is rare for a hospital-based facility. Many research activities are carried out there, for example, accelerator physics studies, developments of novel particle detectors, cross-section measurements, radiation hardness studies, production of novel PET

### 3.2. Beam transport line

radioisotopes, and radiobiological experiments. Due to the variety of different applications, various beam sizes and intensities are needed. The BTL is able to deliver beams from a few mm to a few cm diameter on target of the intensities from pA to the maximum current of  $150 \mu\text{A}$ . A schematic view of the BTL is presented in figure 3.6. The beamline is 6.5 m long and ends in a separate bunker, allowing for research ac-

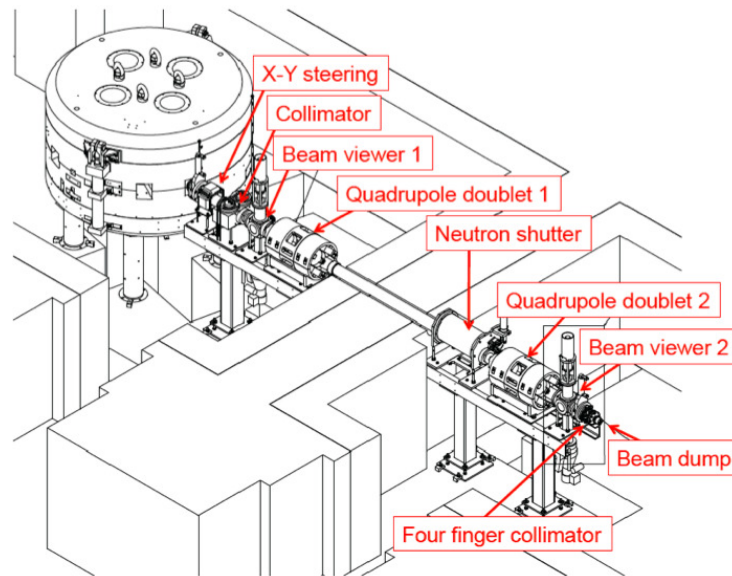


Figure 3.6 – Schematic view of the Beam Transport Line (BTL), where all the main components are highlighted.

tivities and radioisotope production running in parallel. Its FODO lattice is realized by two horizontal-vertical (HV) quadrupole doublets, the former located in the cyclotron bunker and the latter in the bunker of the BTL. To minimize the penetration of neutrons into the second bunker, a movable cylindrical neutron shutter is located inside the beam pipe when the BTL is not in use. To allow for corrections of the beam direction after the extraction, the BTL is equipped with an XY steering magnet able to bend the 18 MeV beam of maximum  $\pm 7$  mrad horizontally or vertically. Two beam viewers are used to measure the beam current and to provide an image of the beam on a fluorescent plate by means of a CCD readout. In order to center the beam on a target at high currents, a “four finger” collimator with four-channel readout can be used. The BTL is terminated with a water-cooled beam dump, which can be replaced for any experimental set-up. The vertical and horizontal alignments are realized with the use of lasers. The beamline with some experimental set-up during alignment is

shown in figure 3.7.



Figure 3.7 – Photograph of the BTL during the alignment of an experimental set-up.

### 3.3 Low current beams

Some research activities, such as cross-section measurements, studies in radiation biology, PIXE and PIGE ion beam analysis, require low beam currents from tens of nA down to the pA range, while PET cyclotrons are designed and optimized for operation above  $10 \mu\text{A}$ . In order to extend the research potential of the Bern cyclotron, our group at the Laboratory for High Energy physics developed a method to reach stable pA proton beams. A study of the low current performance of the Bern cyclotron, to which I significantly contributed, is reported in reference [24] and is reprinted in the Appendix. The method is based on the tuning of the ion source, the RF, and the current in the main coil. For a precise measurement of the beam current, a high-sensitivity Faraday cup [25] was used, as shown in figure 3.8. The effect due to secondary electrons was reduced to a negligible level by applying a polarization potential exceeding 50 V. The produced signal was read out by means of a digital electrometer with a sensitivity of about 1 pA.

The minimum beam currents on target, obtainable by reducing only the arc current of



Figure 3.8 – High-sensitivity Faraday cup installed at the end of the BTL for low current performance studies.

the ion source, are as low as a few  $\mu\text{A}$ . The arc current cannot be lower than 1 mA to maintain stability of the plasma inside the ion source. This minimum value and the standard quadrupole settings, optimized for the irradiation of solid targets with the maximum transmission efficiency, were kept during the whole study. The accelerating peak voltage of the 42 MHz RF system can vary from 26.5 to about 36 kV. A decrease in the beam current is expected when the RF voltage is lowered [23]. This effect is mostly due to the fact that the puller is able to extract fewer  $\text{H}^-$  ions from the chimney of the source, when the electric field acting on the periphery of the plasma is smaller. The beam current was measured as a function of the RF peak voltage and the results are shown in figure 3.9. A smooth decrease of more than a factor of four was observed when moving from 36 kV to 26.5 kV. For this measurement, the current of the main coil was set to 137.05 A, which corresponds to the optimal isochronism and, consequently, to the maximum extracted current. With the variation of the RF peak voltage, the Twiss parameters of the initial beam change from the ion source to the injection to the cyclotron. It may also lead to a decrease in the intensity due to transverse mismatching causing beam losses. In order to examine this effect, the beam width was measured in the horizontal and vertical planes as a function of the RF peak voltage. At values below 30 kV, a decrease to the beam size was observed reaching a maximum of about

50 % for the lowest voltage of 27 kV.

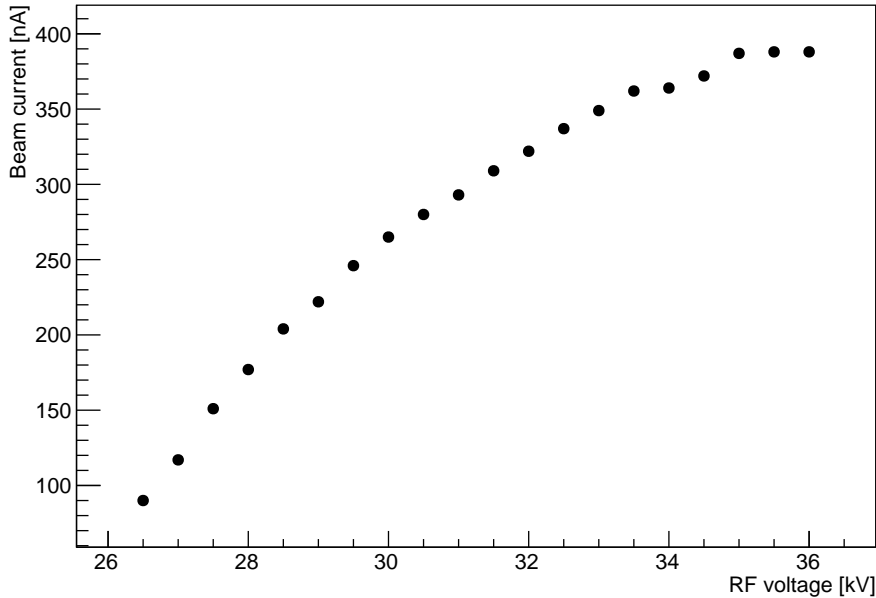


Figure 3.9 – Beam current measured by the Faraday cup as a function of the RF peak voltage [24]. The error bars are not visible due to the small uncertainties.

A further decrease of the extracted current was obtained by operating the cyclotron with a magnetic field which did not correspond to the optimal isochronism. The beam current on target was measured as a function of the current in the main coil. Several consecutive series of measurements were performed and good agreement was found between them. Two of them are shown in figure 3.10: the circles and triangles correspond to increasing and decreasing the main coil current, respectively. A smooth decrease of the beam current was observed when the main coil current was changed from optimal isochronism towards lower values. In this region, stable currents of a few pA were reached. When going from the isochronism condition towards higher values of the main coil current, the extracted current decreases and presents a kink at about 137.4 A. Here the beam is unstable, and therefore, this region is less suitable for low current operation. This effect may occur due to the interception of the beam by the body of the second ion source or to a resonant condition producing beam losses.

The lowest current obtained during the study was  $(1.5 \pm 0.5)$  pA. The uncertainty includes the precision of the electrometer and effects due to beam instabilities. The

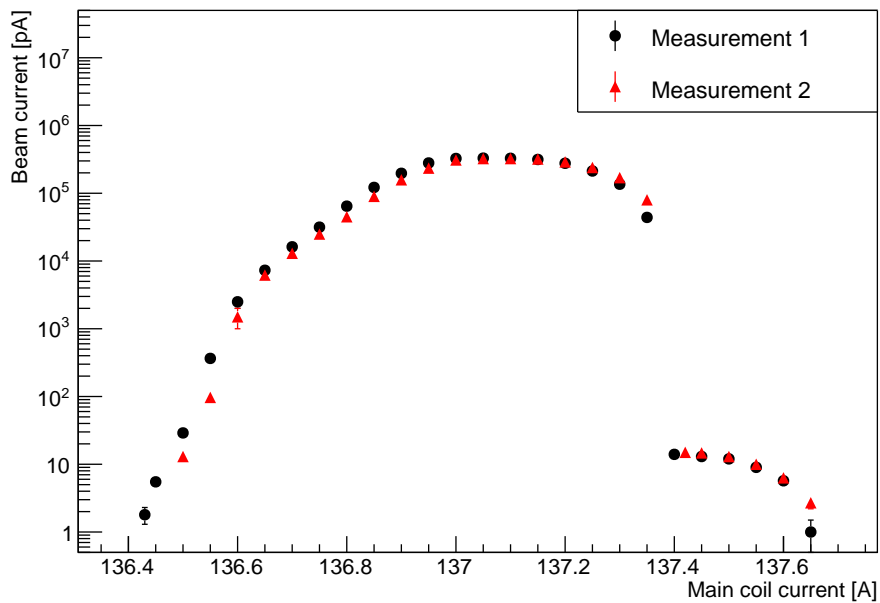


Figure 3.10 – Beam current measured by the Faraday cup as a function of the current in the main coil of the cyclotron [24]. The circles and triangles correspond to two different series of measurements.

stability of the beam current within the uncertainty was observed for a period of about ten minutes. The minimum current reached by using the described method is seven orders of magnitude lower than the minimum stable current, for which the cyclotron was optimized. Moreover, in further experiments with an electrometer of a higher sensitivity, beam currents slightly below 1 pA were produced.



## 4 A system for online measurement of the transverse beam emittance

In this chapter, I present a system for online measurement of the transverse beam emittance, which I developed. It is named  ${}^4\text{PrOB}\epsilon\text{aM}$ , which stands for 4-Profiler Online Beam Emittance Measurement. The core of the system is the UniBEaM detector, whose name *UniBEaM* stands for *Universal Beam Monitor*. This detector has been developed at AEC-LHEP in the University of Bern with my major contribution. I worked on its design from the very beginning, as a summer student at AEC-LHEP.

The first section is devoted to UniBEaM and is divided in five subsections. In the first subsection, the principles of the detector operation are explained. The second subsection presents the performance of UniBEaM with 18 MeV proton beams of different intensities. The third subsection is devoted to a specific mode of the UniBEaM operation, in which non-doped silica fibers are used. In the fourth subsection, I present first tests of a special version of the detector with high-energy proton and pion beams. The last subsection contains a brief description of the commercial UniBEaM.

In the second section, I describe the  ${}^4\text{PrOB}\epsilon\text{aM}$  system, which is composed of four UniBEaM detectors. The basic features are discussed and specific software for measuring the emittance online is presented.

### 4.1 The UniBEaM detector for monitoring ion beams

In this section, a detector based on silica doped fibers designed to monitor the profile of particle accelerator beams is presented. The first proof-of-concept prototype is described in reference [26]. The UniBEaM beam profiler represents a simple, robust, and compact device to be installed along beam transport lines or other critical locations, such as beam injection and extraction points. It is suitable for monitoring both pulsed and continuous beams, and can operate in a wide beam intensity range from 1 pA to tens of  $\mu\text{A}$ . Therefore, the detector is versatile and can be employed in monitoring beams for hadrontherapy (order of 1 nA or less), as well as production of radioisotopes (more than 10  $\mu\text{A}$ ). It is also suitable for research activities, such as radiobiology, particle detector or materials science developments, requiring low intensity beams, down to the pA range.

Since the UniBEaM profiler is the essential part of the  $^4\text{PrOB}\epsilon\text{aM}$  system for transverse beam emittance measurement, I reprint in the Appendix three papers on the UniBEaM detector, which I co-authored. Reference [27] describes the instrument, and reports on measurements performed with a proton beam from the 18 MeV Bern medical cyclotron for beam currents ranging from 1 pA to 20  $\mu\text{A}$ . In reference [28], of which I am the corresponding author, monitoring of high-energy proton and pion beams with a specific version of the UniBEaM detector is reported. Reference [29] provides a description of the commercial version of the UniBEaM detector, which was developed with my significant contribution in collaboration with D-Pace Inc. (Canada).

#### 4.1.1 Principles of operation

The UniBEaM detector is based on a single doped silica fiber moving transversally across the beam. A photograph of UniBEaM installed on the BTL of the Bern cyclotron, with the main components highlighted, is shown in figure 4.1. Charged particles pass through an approximately 8 cm long sensing fiber and cause scintillation. The produced light is transported to a photon detector through a commercial multi-mode optical fiber, which is coupled to the scintillating fiber. In this way, the optical signal can be transported over more than 20 meters with negligible losses. The sensing fiber

#### 4.1. The UniBEaM detector for monitoring ion beams

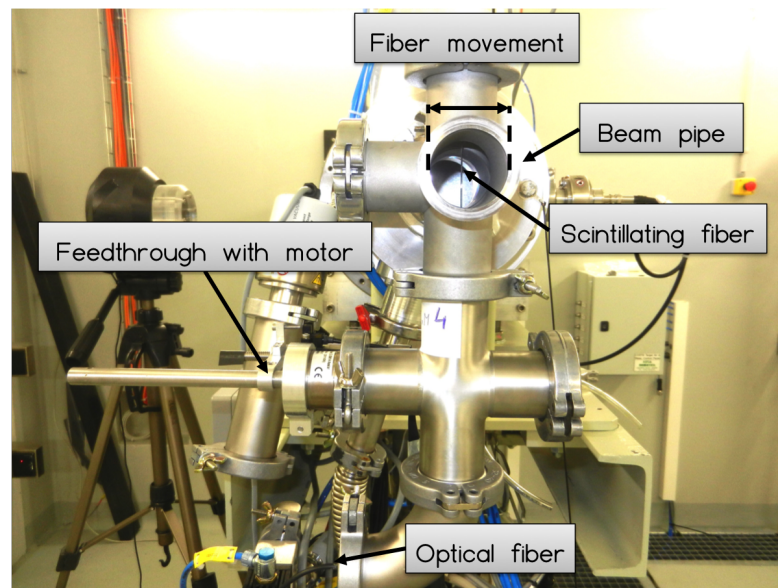


Figure 4.1 – The UniBEaM detector installed on the BTL of the Bern cyclotron. The main components are highlighted.

has a diameter ranging from  $200\ \mu\text{m}$  to  $400\ \mu\text{m}$ , while the diameter of the core of the optical fiber is  $400\ \mu\text{m}$  ( $200\ \mu\text{m}$  in newer versions of the device). The coupling between the fibers uses two standard SMA905 connectors, to which the fibers are glued. The centering is provided by an SMA mating sleeve, to which the connectors are screwed. To minimize light losses, the surfaces of the fibers are polished and an optical grease is used. The inner part of the optical fiber, which stays under vacuum, terminates with another SMA905 connector and is coupled with the outer part of the optical fiber by means of a vacuum tight SMA feedthrough. The sensing fiber is moved across the beam by a vacuum tight linear motion feedthrough attached to a spindle drive and a brushless motor. The motor communication port and data acquisition module are integrated in a Raspberry Pi 2 board and are controlled by dedicated software which I developed. The step size, range, and speed of the motion are adjustable. A typical beam scan consists of a series of  $250\ \mu\text{m}$  motor steps. At each position of the fiber, the light intensity is measured. The electric signal of a photon detector (photodiode or photomultiplier) is digitized and plotted online as a function of the position. The data are stored in a file and can be used for further analysis. The typical experimental set-up of the UniBEaM detector is shown in figure 4.2. The laboratory version of UniBEaM, which is described here, allows the beam profile to be measured only in

## Chapter 4. A system for online measurement of the transverse beam emittance

one plane (horizontal or vertical). To perform the complementary measurement for another plane, the whole device must be turned by 90 degrees. The detector allows beam profiles to be measured in a non-destructive way and without affecting the operation of the accelerator. Moreover, all the radiation sensitive devices are located outside the bunker, which allows UniBEaM to be used in presence of intense radiation fields.

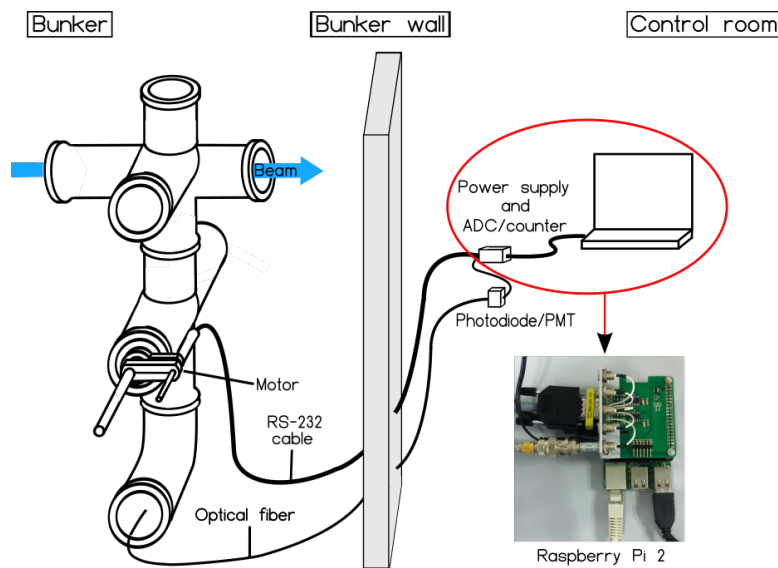


Figure 4.2 – Typical experimental set-up of the UniBEaM detector.

### 4.1.2 Performance of UniBEaM with 18 MeV proton beams

The profiles of 18 MeV proton beams were measured for different currents at the Bern medical cyclotron. The UniBEaM detector was installed on the BTL and was followed by a Faraday cup, as shown in figure 4.3. The beam current was measured by means of the Faraday cup and a high-precision electrometer. The fiber response with respect to the local beam intensity was also studied, since only a linear dependence guarantees an accurate estimation of the beam width. For each current range, the integrals of beam profiles, collected for different total beam currents, were calculated.

## 4.1. The UniBEaM detector for monitoring ion beams



Figure 4.3 – The UniBEaM detector and the Faraday cup installed on the BTL of the Bern cyclotron.

### Beam currents in the pA range

For the measurements in the pA range,  $\text{Ce}^{3+}$  doped silica fibers were used due to their good scintillation properties [26, 30] and large light yield. Because the light yield is limited for such low currents, a specific read-out system was designed. It comprises an ultra low noise single-photon counter (IDQ ID100-MMF100ULN), a NIM discriminator, and a 100 MHz counting rate CAMAC scaler. The single-photon counter is based on a solid state photomultiplier and allows a time resolution of 40 ps to be obtained, with a maximum counting rate of 20 MHz and a dark count rate of 20 Hz. The beam profile measurements consisted of photon counting for a duration of 100 ms at each position of the scintillating fiber. Beam profiles obtained for currents of 1 pA and 50 pA are shown in figure 4.4 [27]. The signal due to the beam is clearly visible with a signal-to-noise ratio of 10 and 320 at 1 pA and 50 pA, respectively. A good linearity of the fiber response in the pA range was found, as shown in figure 4.5 [27]. This allows the UniBEaM detector to be used for measuring the beam current with an accuracy of  $\sim 1\%$ .

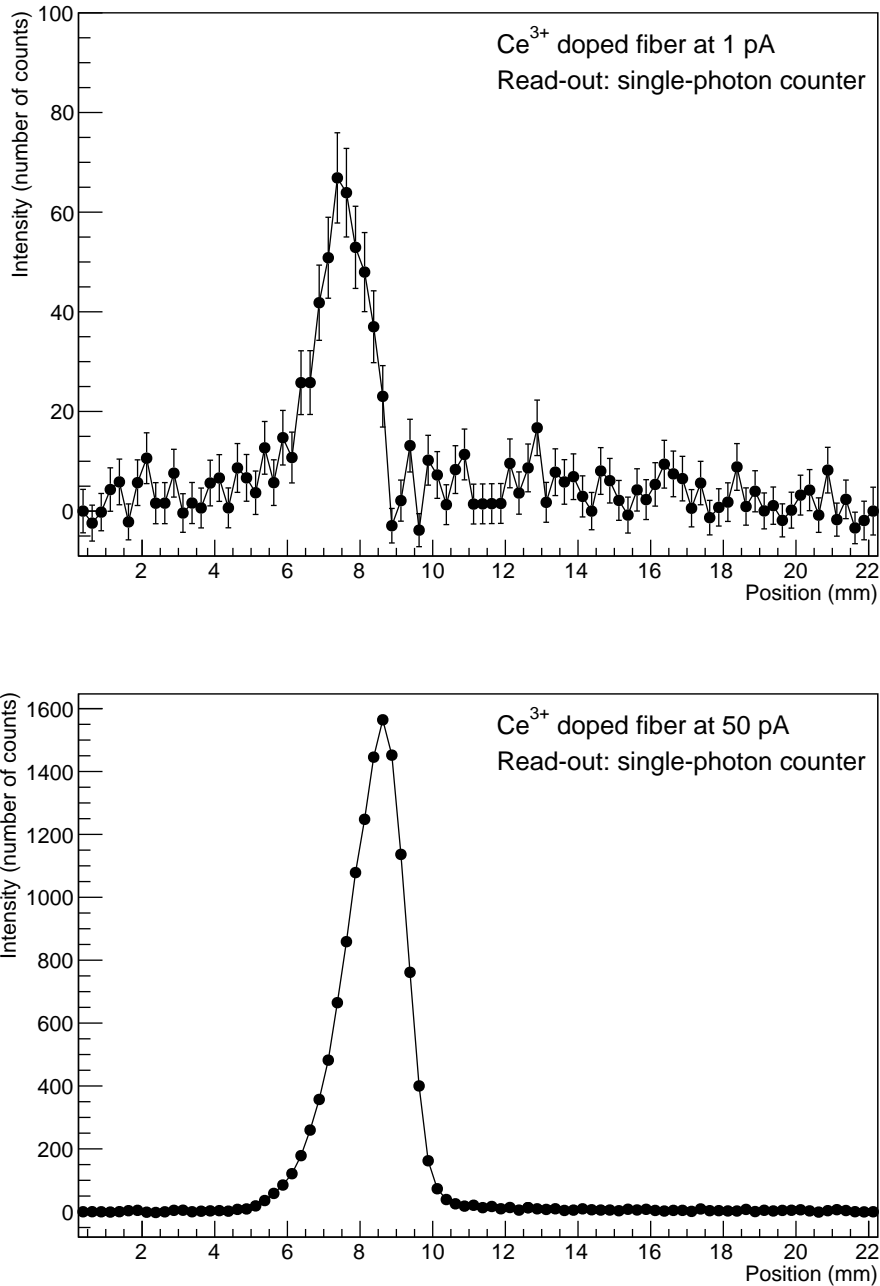


Figure 4.4 – Profiles of a 1 pA proton beam (top) and a 50 pA proton beam (bottom) measured with a Ce<sup>3+</sup> doped silica fiber [27].

#### Beam currents in the nA and $\mu$ A range

In the nA range, the measurements were performed with both Sb<sup>3+</sup> [26, 31] and Ce<sup>3+</sup> [26, 30] doped fibers. To read out the signal, a photodetector based on a silicon

#### 4.1. The UniBEaM detector for monitoring ion beams

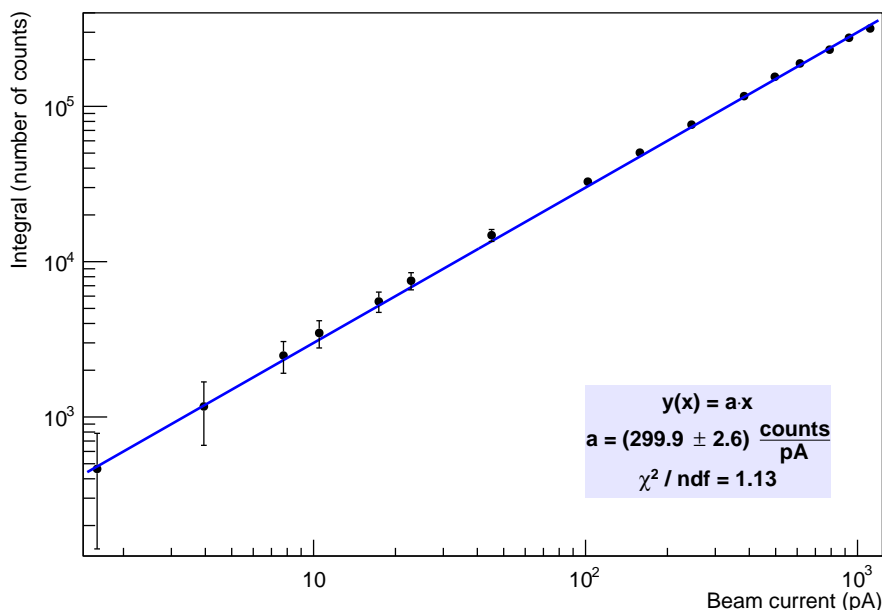


Figure 4.5 – Profile integral as a function of beam current in the pA range [27]. Both axes are shown in a logarithmic scale. The parameters of a linear fit are given in the inset.

photodiode and another using a photomultiplier tube (PMT) were used. These two devices are less sophisticated and less expensive than the read-out system used for the measurements in the pA range. Moreover, the single-photon counter, depending on the efficiency of the sensing fiber, tends to saturate for currents exceeding 100 nA. However, this problem can be solved by using optical attenuators, and this method is applied in the current laboratory version of UniBEaM. The wavelength spectrum of  $\text{Ce}^{3+}$  doped fibers peaks at 490 nm, which matches the responsivity of the PMT but not of the silicon photodiode. Therefore, only the PMT was used with this kind of fiber. In the case of  $\text{Sb}^{3+}$  doped fibers, the wavelength spectrum presents two peaks at 695 nm and 755 nm, which makes them suitable for both read-out devices. As an example, a beam profile measured at 50 nA with an  $\text{Sb}^{3+}$  doped fiber is shown in figure 4.6. The signal due to the beam is clearly visible with a signal-to-noise ratio of 90. For an  $\text{Sb}^{3+}$  doped fiber, the linearity was also studied. A good linearity was found for beam currents up to 3  $\mu\text{A}$ , as presented in figure 4.7 [27]. In this range, UniBEaM can be used to measure the beam current with an accuracy of  $\sim 1\%$ .

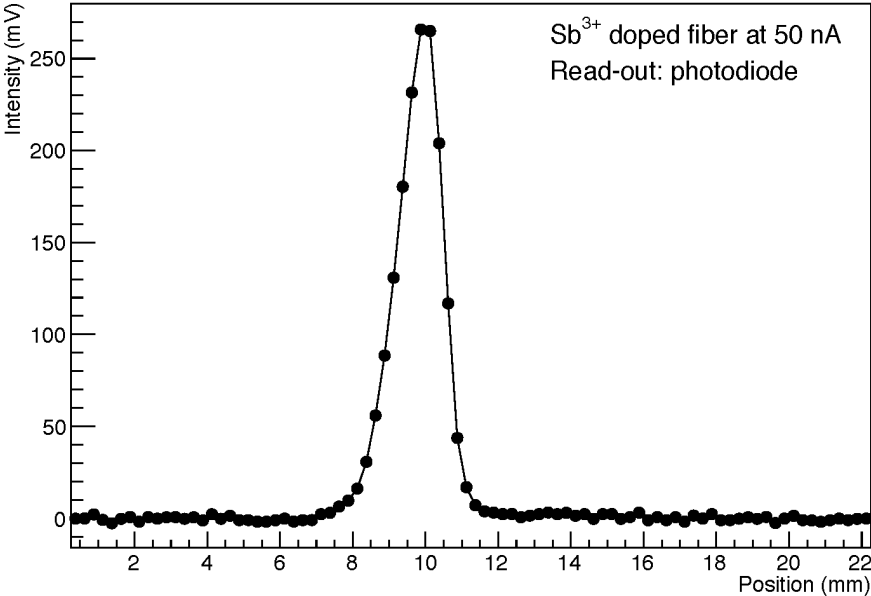


Figure 4.6 – Profile of a 50 nA proton beam measured with an  $Sb^{3+}$  doped silica fiber [27].

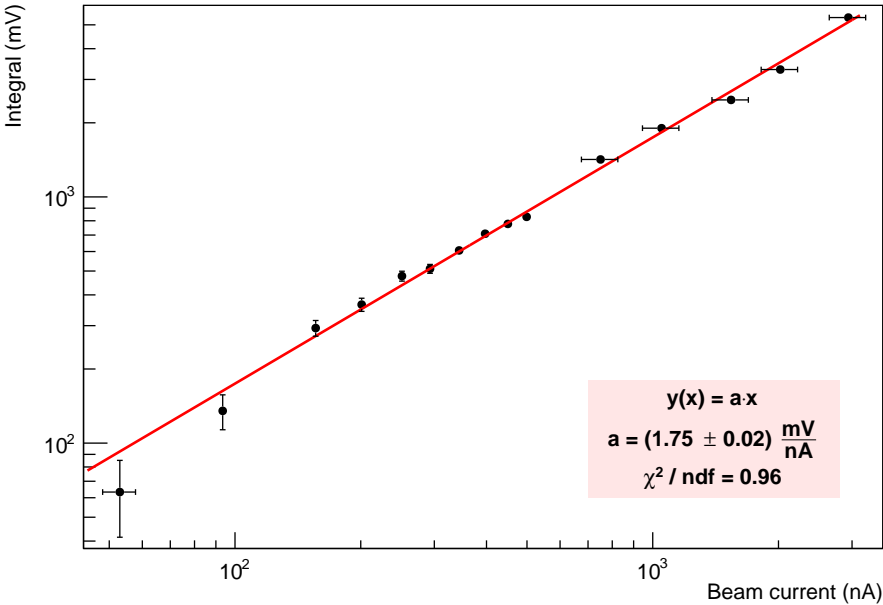


Figure 4.7 – Profile integral as a function of beam current in the nA and  $\mu A$  range [27]. The parameters of a linear fit are given in the inset.

#### 4.1. The UniBEaM detector for monitoring ion beams

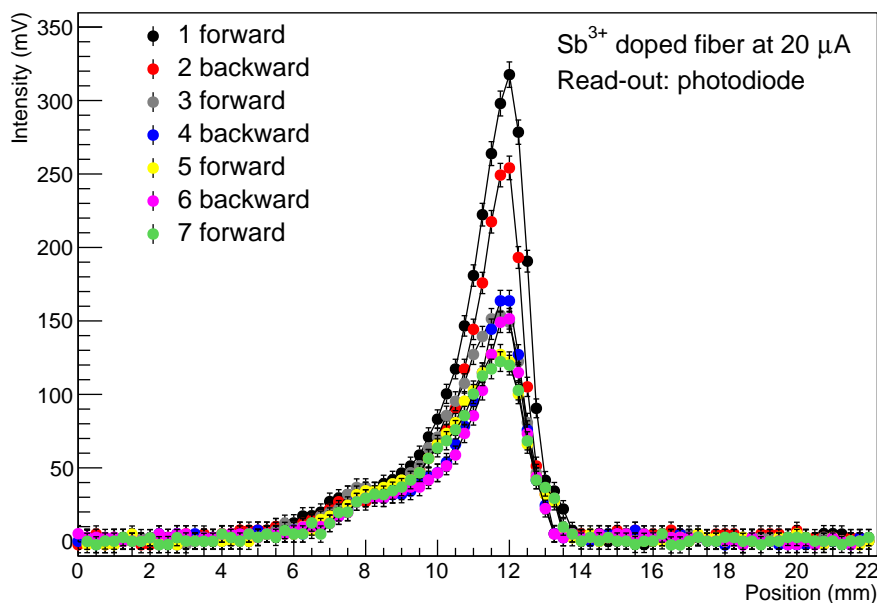


Figure 4.8 – Seven consecutive beam profiles measured at a current intensity of  $20 \mu\text{A}$  [27].

The linearity was found to be lost for currents exceeding a few  $\mu\text{A}$ , as a result of thermal effects [26]. Due to the changes in the emission and transmission properties of the fiber, some distortions of the beam profile are observed, as shown in figure 4.8 [27]. Seven consecutive profiles were measured at a beam current of  $20 \mu\text{A}$  with an  $\text{Sb}^{3+}$  doped fiber. Each beam scan took about 3 seconds. The signal maximum was found to decrease significantly during the first three scans. Since the conditions of the fiber stabilize after some time, the signal decrease is less pronounced for the following scans. The scintillating properties of the sensing fiber can be recovered by keeping it outside the beam for a few minutes. The thermal effects limit the performance of the UniBEaM detector, since the beam width cannot be assessed accurately. However, for many applications, such as radioisotope production, the knowledge of the beam position and an approximate estimation of the beam size are enough to optimize the irradiation. Furthermore, the system is still sensitive to such effects as asymmetries in the beam profile due to beam extraction effects. This is visible in figure 4.8, where the left-side tail of the profile is due to the fact that not all of the  $\text{H}^-$  ions reach the

stripper at the same turn, and thus, stripping occurs at several energies.

### 4.1.3 Beam monitoring with non-doped silica fibers

Scintillation also occurs in non-doped optical fibers due to the presence of impurities. The feasibility of using an optical fiber for both producing and transmitting scintillation light was demonstrated [27]. Such a solution leads to a further simplification of the detector. In the nA range, it can be adopted with a single-photon counter due to the limited light yield, whereas in the  $\mu\text{A}$  range a silicon photodiode can be used. Beam profiles obtained for currents of 1 nA with a single-photon counter and for 1  $\mu\text{A}$  measured with a silicon photodiode [27] are shown in figure 4.9. Signal-to-noise ratios of 55 and 120 were obtained for the former and the latter profile, respectively. A good linearity of the fiber response was found for the currents up to 300 nA, as shown in figure 4.10. The read-out based on single-photon counter saturates at currents exceeding 300 nA. The intensity range can be extended by using optical attenuators. In the  $\mu\text{A}$  range, the linearity is lost at a few  $\mu\text{A}$  due to thermal effects, as previously discussed.

4.1. The UniBEaM detector for monitoring ion beams

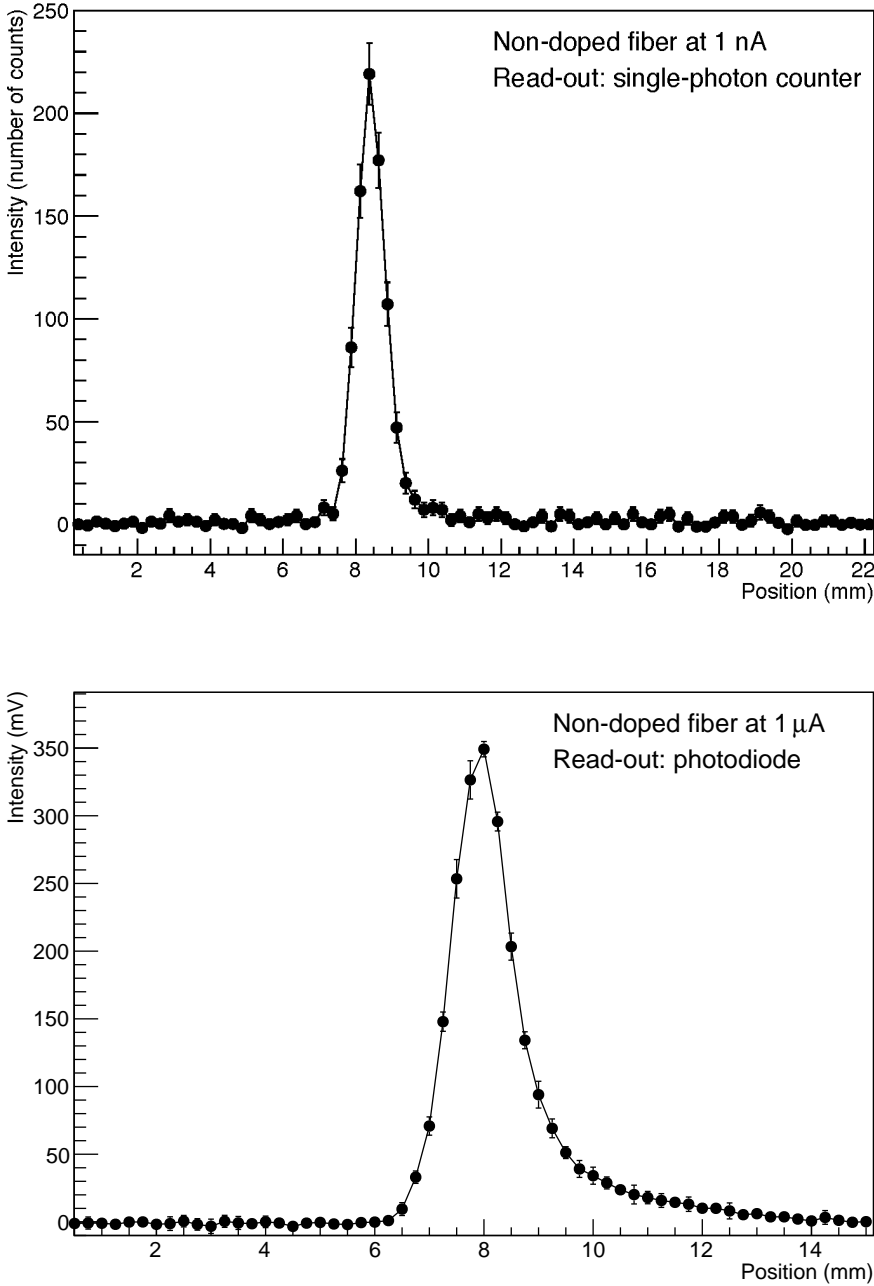


Figure 4.9 – Profiles of a 1 nA proton beam (top) and a 1 μA proton beam (bottom) [27] measured with a non-doped silica fiber.

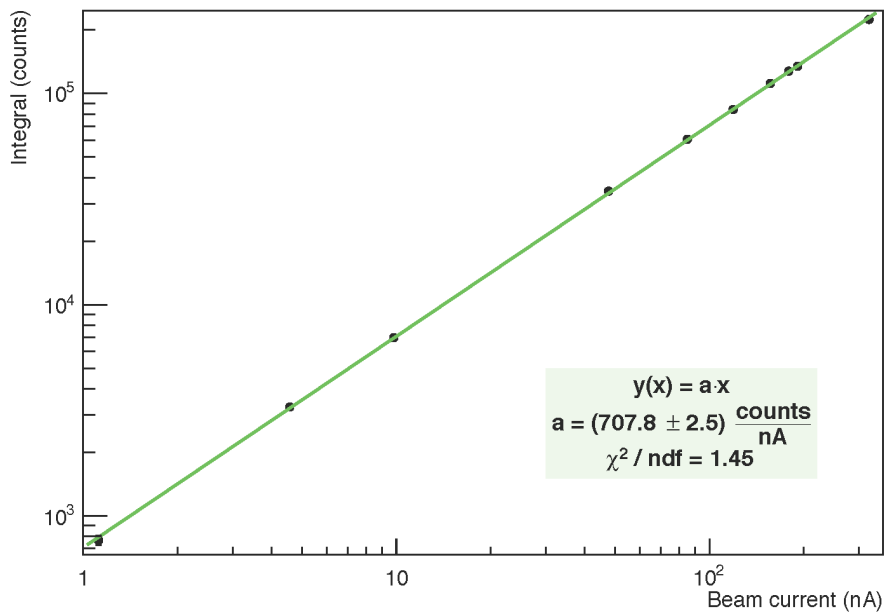


Figure 4.10 – Profile integral as a function of beam current for a non-doped optical fiber. The parameters of the linear fit are given in the inset.

### 4.1.4 Monitoring of high-energy proton and pion beams

In order to detect high-energy proton and pion beams, a specific version of the UniBEaM detector was developed [28]. This detector was tested at the CERF (CERN-EU high energy Reference Field) facility [32] at CERN with the aim of optimizing the position of the primary beam. CERF was designed to provide reference neutron fields, mostly for radiation protection studies. Neutrons are produced by colliding a mixed proton and pion beam on a metallic target. Since the energy of the beam is 120 GeV, the UniBEaM detector can operate in air, as shown in figure 4.11. The de-bunched beam is extracted for periods of 5 seconds, the so-called spills, according to the duty cycle of the Super Proton Synchrotron (SPS), which provides the primary proton beam. The number of particles per spill varies between 10<sup>6</sup> and 10<sup>8</sup>. Pions account for about one third of the beam, and protons for two thirds. The beam current ranges between 32 fA and 3.2 pA, while the diameter of the beam spot is a few centimeters. Since the beam intensities are extremely low and the energy deposited in the sensing fiber is very limited for such a high-energy beam, special scintillating fibers, providing a high

#### 4.1. The UniBEaM detector for monitoring ion beams

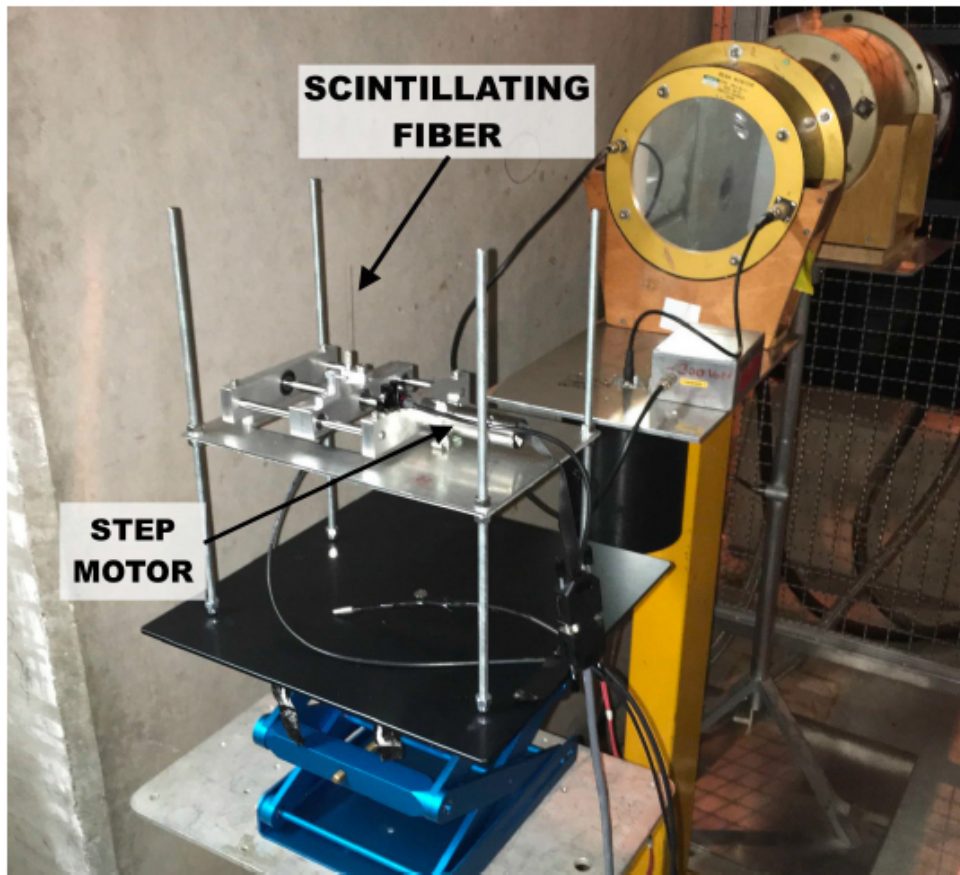


Figure 4.11 – The UniBEaM detector located in the air after the exit window of one of the SPS secondary beam lines at CERN.

light yield, were employed. They consist of a 600  $\mu\text{m}$  diameter core and 75  $\mu\text{m}$  thick fluorinated silica cladding. The emission spectrum of these fibers peaks at 450 nm due to a radiative transition of  $\text{Ce}^{3+}$  [33]. The Ce-doped fiber is moved transversally to the beam by means of a motor and is connected to a standard multimode optical fiber, as in the case of the standard UniBeaM detector. The read-out system is identical to the one used for measuring proton beam currents in the pA range. It is based on an ultra low noise single-photon counter.

The first measurements were performed at about 1/3 of the maximum intensity of the extracted beam. The beam profile, obtained by counting signals over a period of five minutes at each fiber position, is shown in figure 4.12 [28]. The step of the fiber movement was set to 1 mm. The background was estimated by performing a fit and

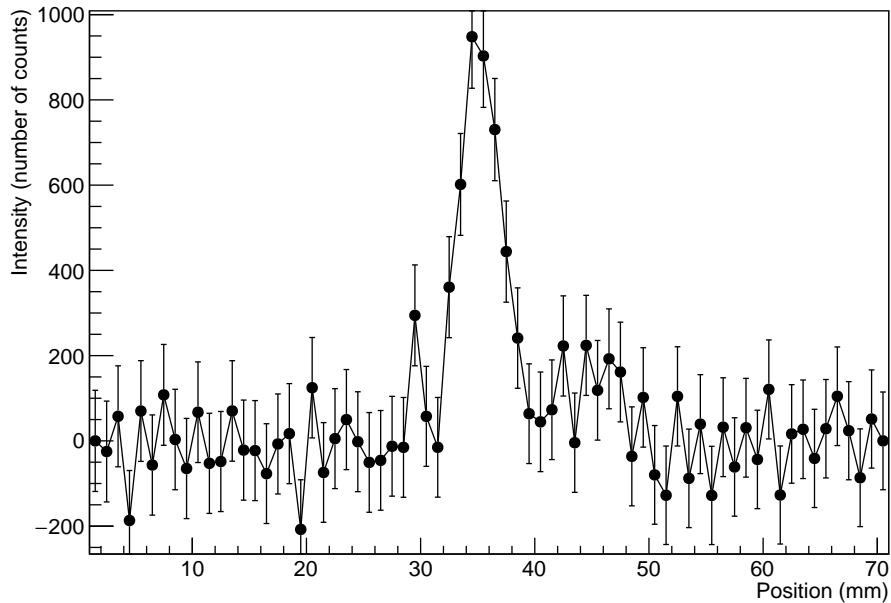


Figure 4.12 – Beam profile of the hadron beam measured with the in-air UniBEaM detector at the CERF facility [28].

then subtracted from the data. A second series of measurements was performed to optimize the overall acquisition time and the noise level. The fiber was kept at each position for 2 minutes and the number of counts was recorded every second. In this way, the time structure of the beam can be monitored, as presented in figure 4.13 [28]. In this figure, the typical synchrotron spill pattern can be seen. The noise was subtracted by means of a fit procedure.

Further measurements at the CERF facility are planned. Among the improvements to be implemented are new types of scintillating fibers and a triggering algorithm. The algorithm will allow counting to be performed only in the presence of the beam. The trigger signal will be obtained directly from the SPS feedback loop. This will lead to a better signal-to-noise ratio and to reducing the time to make a profile measurement.

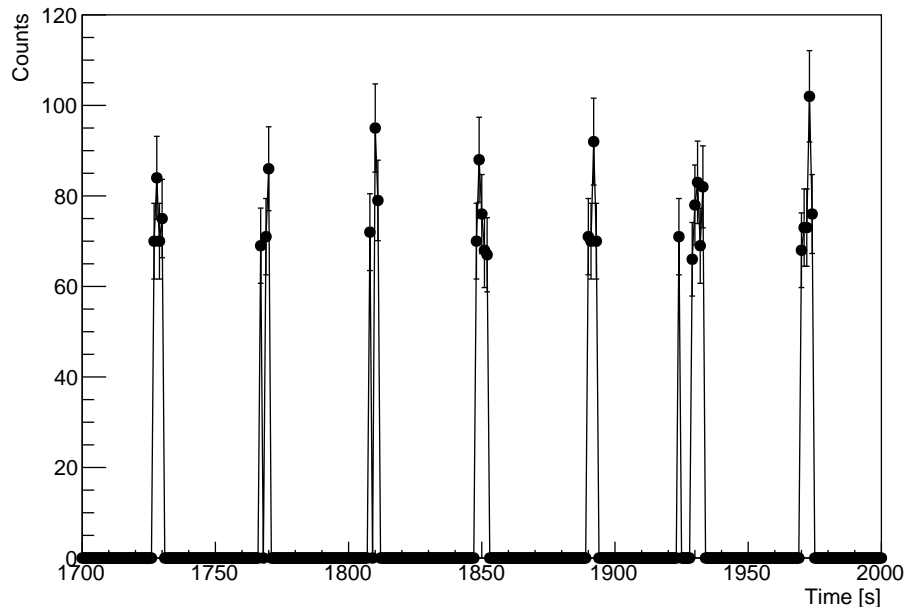


Figure 4.13 – Intensity of successive spills of the SPS synchrotron at CERN [28].

### 4.1.5 Commercial UniBEaM detector

A commercial version of the UniBEaM detector has been developed by D-PACE Inc. (Canada) and our group at AEC-LHEP in the University of Bern. Its design and beam tests with proton and  $H^-$  beams are reported in reference [29]. The commercial UniBEaM features two probes; one for horizontal X-profiles and one for vertical Y-profiles, as shown in figure 4.14 [29]. The sensor fibers are moved through the beam by stepper motor actuators. The probes do not contain electronic components, being radiation resistant. Two ports in each probe provide access to replace the fibers by specifically designed cartridges. The instrument can be installed at any beamline with standard KF or CF flanges. The whole device has an insertion length of only 70 mm. The commercial UniBEaM installed on the BTL is presented in figure 4.15. The sensing fibers are made by the University of Milano-Bicocca's Department of Materials Science using the sol-gel process. The silica fibers are doped with  $Ce^{3+}$  ions as luminescent activators [33, 34]. The 200  $\mu m$  diameter sensing fibers are coupled to 200  $\mu m$  hard-clad optical fibers within the probe by means of SMA in-vacuum connectors. These fibers

## Chapter 4. A system for online measurement of the transverse beam emittance

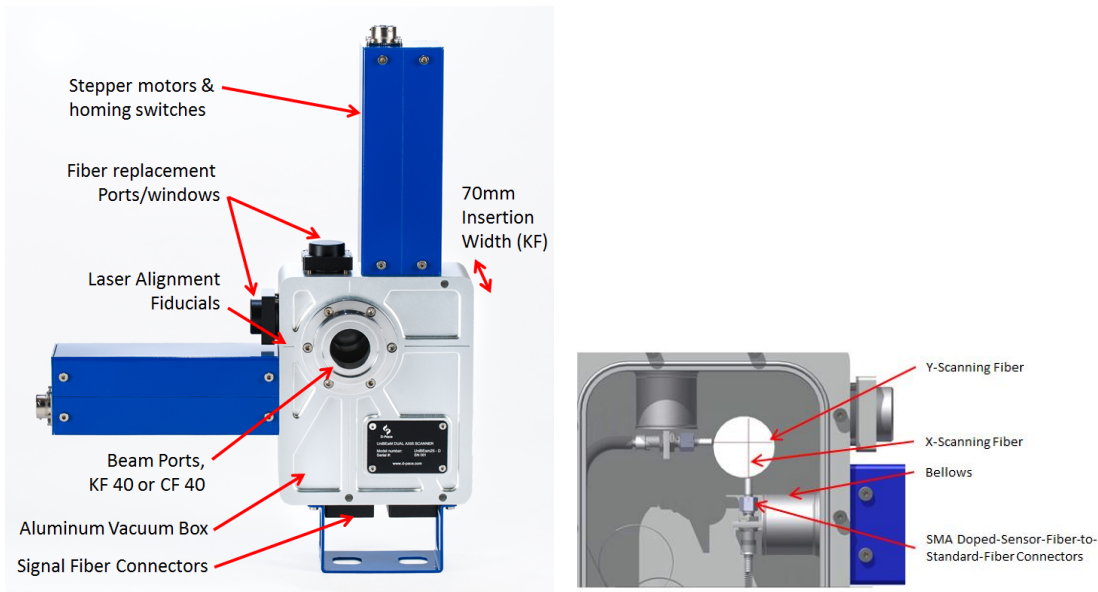


Figure 4.14 – D-Pace’s commercial UniBEaM dual axis probe (top) and its internal view (bottom) [29]. The main components are highlighted.

pass through vacuum feedthroughs and are connected on the atmosphere side to another two  $400\ \mu\text{m}$  fiber-optic patch cables. The optical signal is transmitted through them to a silicon photomultiplier located in the UniBEaM controller. Beam profiles are acquired and analyzed by the UniBEaM software, which allows user to adjust beam scan parameters, such as scanning speed, as well as to choose the operation mode - single or continuous scanning, or intensity measurement at fixed position. The user interface of the UniBEaM software is shown in figure 4.16 [29].

The limitations of the commercial UniBEaM detectors are similar to the ones of the laboratory version. The beam tests with 18 MeV protons showed that for beam currents exceeding tens of  $\mu\text{A}$ , the linear response is reduced due to thermal effects. For the  $20\ \mu\text{A}$  beam of about 5 mm diameter, the responsivity decreased by 25 % following a 3 second pass of the fiber through the beam. The corresponding maximum absorbed power density of the fiber was estimated to be about  $0.9\ \text{W}\cdot\text{mm}^{-2}$ .

Tests of the commercial UniBEaM with different types of beam, such as 3-8 MeV deuteron beams, are foreseen. Our group is continuing to work in collaboration with D-PACE on extending the range of applications of the detector.

4.1. The UniBEaM detector for monitoring ion beams

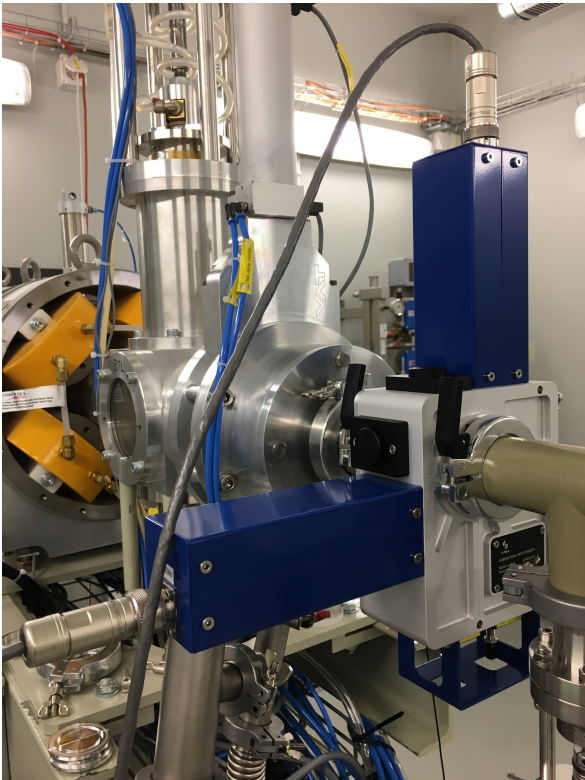


Figure 4.15 – D-Pace’s commercial UniBEaM installed on the BTL.

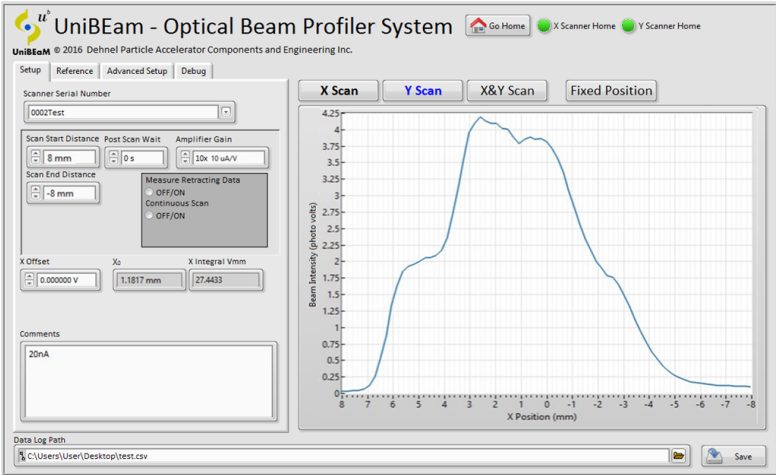


Figure 4.16 – User interface of the commercial UniBEaM detector [29].

## 4.2 <sup>4</sup>PrOBεaM: a system for online measurement of the transverse beam emittance

The <sup>4</sup>PrOBεaM system was conceived to measure the transverse beam emittance in a simple and efficient way using the multiple beam profiler method, described in chapter 2. In the contrary to, for instance, the quadrupole variation method, the use of multiple beam profiler does not require any prior knowledge of the optical elements of the beamline. The use of <sup>4</sup>PrOBεaM for making emittance measurements is reported in references [35, 36], reprinted in the Appendix, of which I am the first author. The system consists of four UniBEaM detectors (figure 4.17) and its total length is 54 cm, which allows <sup>4</sup>PrOBεaM to be installed at any location along beamlines or directly at the accelerator outpost. The distance between the sensing fibers is



Figure 4.17 – The <sup>4</sup>PrOBεaM system for online measurement of the transverse beam emittance.

13.5 cm. Depending on the beam current range, different fibers are used. For currents exceeding 1 nA, non-doped optical fibers are usually used. For an accurate estimation of the width of each beam profile, the linear response of the fiber must be provided. For this reason, <sup>4</sup>PrOBεaM is currently used with beam intensities ranging from 1 pA

## 4.2. <sup>4</sup>PrOBεaM: a system for online measurement of the transverse beam emittance

to  $5 \mu\text{A}$ . The signal from each UniBEaM detector is transmitted to a single photon-counter (ID Quantique SA) and digitized. All four fibers are moved simultaneously through the beam in order to minimize the influence of possible beam instabilities. At each position of the fibers, photon counting is performed over a period of 100 ms and the number of counts is plotted online as a function of the position and stored in a data file. The whole data acquisition process consists of one full beam scan and is controlled by a Raspberry Pi 2 module with software I developed in the C++ programming language. The readout system is placed outside of the beamline bunker and is shown in figure 4.18.

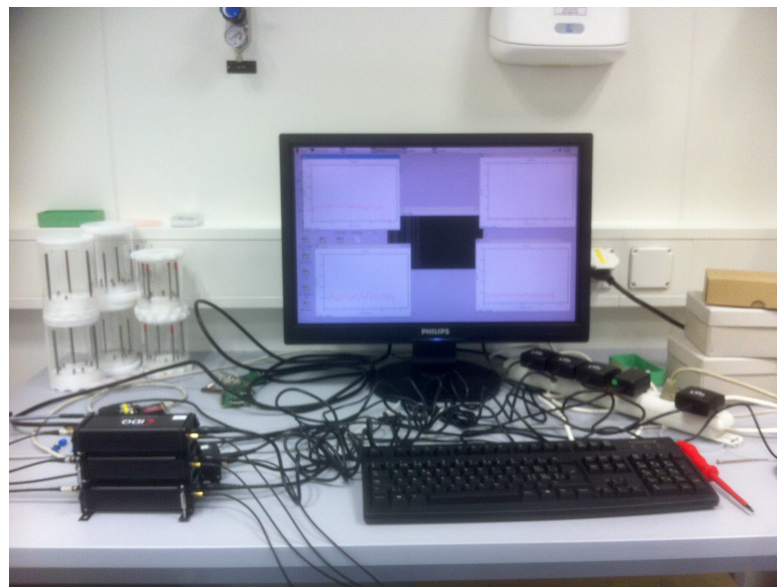


Figure 4.18 – Readout system of <sup>4</sup>PrOBεaM located in the control room.

When the beam scan is complete, a ROOT [37] script is automatically launched, in which the whole data analysis is implemented. All four beam profiles are plotted in a separate window as histograms (figure 4.19) and saved in a pdf file. The user has the possibility to limit the region of interest by choosing the minimum and maximum considered position for each profile. This is especially useful when the signal-to-noise ratio is relatively low or the differences between the width of four profiles are small. In these cases, indicating the region in which the signal is due to the beam increases accuracy of the beam width evaluation. The background is mostly due to the noise of the readout devices and is subtracted using a measurement performed without

## Chapter 4. A system for online measurement of the transverse beam emittance

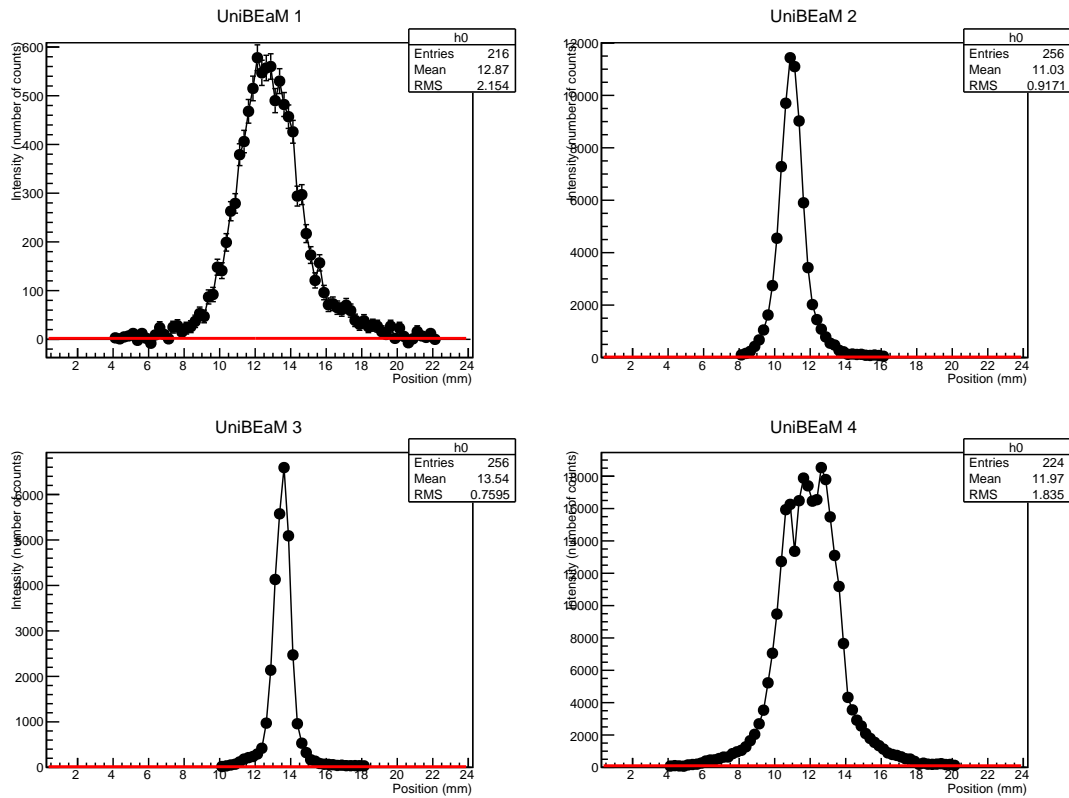


Figure 4.19 – Four beam profiles measured with the  $^4\text{PrOB}\epsilon\text{aM}$  system. The region of interest is defined by the user, and the red line corresponds to the subtracted background.

beam in stable conditions. For each histogram of the beam profile, an estimate of the variance ( $\text{RMS}^2$ ) and the corresponding uncertainty are calculated. The estimates of the variance are plotted as a function of the distance from the first UniBEaM detector, and a quadratic fit is performed. The plot with the corresponding best fit is displayed in another window (figure 4.20) and saved in a separate pdf file. The user obtains, as an output, the value of the RMS transverse emittance with its uncertainty, as well as all the fit parameters representing the beam matrix components at the location of the first UniBEaM detector. The total time to make one measurement of the beam emittance is about 1 minute.

The current version of  $^4\text{PrOB}\epsilon\text{aM}$  allows measurements of the beam emittance to be performed in one plane at a time. To measure the emittance in another plane, the

## 4.2. <sup>4</sup>PrOBεaM: a system for online measurement of the transverse beam emittance

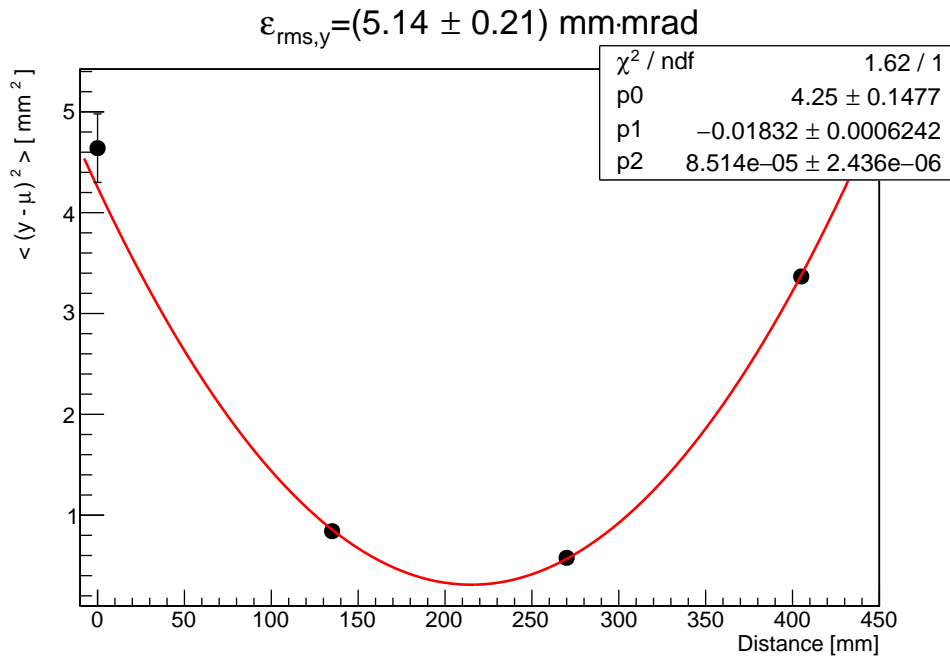


Figure 4.20 – Variance as a function of the distance from the first UniBEaM detector obtained with the <sup>4</sup>PrOBεaM system. The red line corresponds to the best fit and the fit parameters are given in the inset.

whole system must be rotated by 90 degrees. Simultaneous scanning in both planes is planned in a new version of the system, currently under development. Future optimization will be also focused on easier alignment of <sup>4</sup>PrOBεaM by fitting all the fibers in a single vacuum chamber. To simplify the process of beam optimization for the emittance measurement, the drift space between fibers will be adjustable. The multiple profiler method works best if the beam comes to a waist between the first and the last profiler. For a fixed distance between the fibers, this condition can be obtained only by tuning the settings of quadrupole magnets. The commercialization of <sup>4</sup>PrOBεaM is also considered in the near future.



## 5 Characterization of proton beams

In this chapter, work on the characterization of proton beams is presented. An extensive experimental study, reported in the first section, was conducted at the Beam Transport Line (BTL) of the 18 MeV Bern medical cyclotron. The transverse RMS beam emittance has been measured as a function of some cyclotron parameters, such as the magnetic field, RF peak voltage, and azimuthal angle of the stripper. For this purpose, the  ${}^4\text{PrOB}\epsilon\text{aM}$  system, described in the previous chapter, was employed. For the standard cyclotron settings, the RMS transverse beam emittance was also measured using a method based on variations of the quadrupole strength, and the results obtained with both techniques have been compared. The longitudinal beam dynamics were characterized by measuring the proton energy distribution. For this study, I proposed a method based on aluminum absorbers of different thickness, a UniBEaM detector, and a Faraday cup. Based on the results of the beam emittance measurements, I developed a simulation of the BTL. This tool allows machine parameter to be tuned online to optimize the beam characteristics for specific applications. The studies carried out at the BTL of the Bern cyclotron are reported in references [35, 36] reprinted in the Appendix, of which I am the first author.

In the second section, I report measurements of the RMS transverse beam emittance taken at the TR24 cyclotron in Strasbourg. For these measurements, the  ${}^4\text{PrOB}\epsilon\text{aM}$  was again deployed. The beam emittance has been measured for two different proton energies and three different azimuthal angles of the stripper.

## 5.1 Beam characterization of the 18 MeV Bern cyclotron

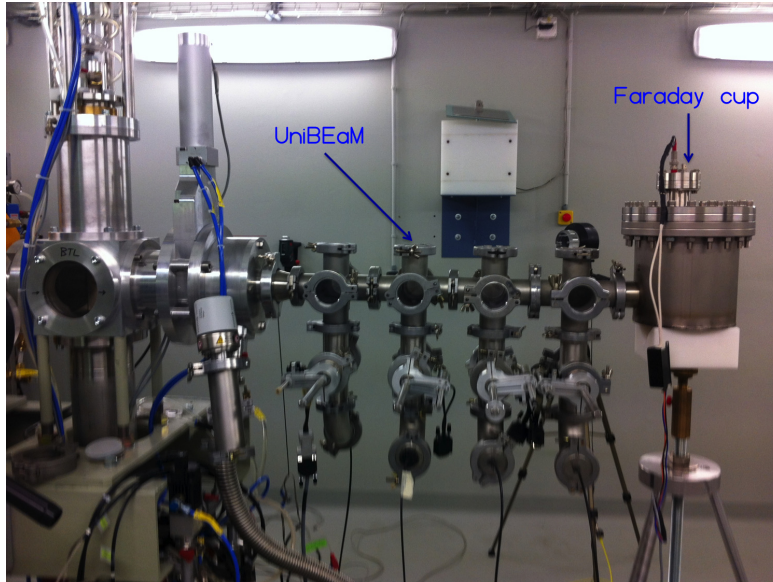


Figure 5.1 – The  ${}^4\text{PrOB}\epsilon\text{aM}$  system and a Faraday cup installed on the BTL.

### 5.1.1 Transverse RMS beam emittance as a function of the cyclotron parameters

The Bern cyclotron can be operated in two modes automatic and manual. The automatic mode is used for radioisotope production to optimize the machine performance aiming at high beam currents. For research purposes, the manual mode is used. This mode of operation is based on tuning the cyclotron parameters in order to obtain beams according to specific needs. In particular, the settings which produce non-optimal isochronism operation are deliberately selected when low current beams are required, as reported in [24]. To keep the same beam intensity over the course of long irradiations, the cyclotron parameters have to be continuously tuned. Therefore, the influence of a few important parameters on the beam emittance was studied by measuring the transverse RMS emittance as a function of the varied parameter. The  ${}^4\text{PrOB}\epsilon\text{aM}$  system, which can make a single emittance measurement in a short time, was employed. A Faraday cup was installed at the end of the beamline to measure the beam current.  ${}^4\text{PrOB}\epsilon\text{aM}$  and the Faraday cup installed on the BTL are shown in

## 5.1. Beam characterization of the 18 MeV Bern cyclotron

figure 5.1. For the measurements in the complementary plane,  ${}^4\text{PrOB}\epsilon\text{aM}$  was rotated by 90 degrees. The parameters studied include the main coil current, RF peak voltage, and azimuthal stripper angle. The standard cyclotron settings used for irradiations at the BTL, corresponding to the maximum beam transmission, are reported in table 5.1.

Table 5.1 – The standard settings of the cyclotron parameters used for research purposes.

Cyclotron parameter	Value
Main coil	136.9-137.2 A
RF peak voltage	32 kV
Stripper angle	84.2°
Ion source	1 mA

### Variation of the main coil current

Control of the main coil current is essential for obtaining low intensity beams down to pA range, since it allows the cyclotron to be operated in the region of non-optimal isochronism. The set point corresponding to the optimal isochronism also has the tendency to change towards higher values of the main coil current during long cyclotron runs. In order to study the influence of the main coil current on the transverse beam emittance, the current of the main coil was gradually increased and the corresponding RMS emittance values were measured. The other cyclotron parameters were kept at their standard values (table 5.1). The minimum and maximum main coil currents were defined by producing the minimum beam intensity of the order of 1 nA. Since the value of the main coil current corresponding to the optimal isochronism depends on the operation time, the main coil scans for horizontal and vertical planes were performed first for a “cold” machine, meaning the cyclotron had not been operated before the measurement for at least a few hours. The results for the horizontal and vertical plane are presented in figure 5.2 [35]. In the horizontal plane, the value of the beam emittance, after an initial drop, increases with the main coil current until the optimal isochronism is reached. Then, the emittance reaches a plateau defining the region of the standard operation of the cyclotron. After that, the emittance decreases reaching a local minimum. This is followed by another increase with a local maximum at a current of about 137.3 A. In this region, the beam is unstable and this effect may

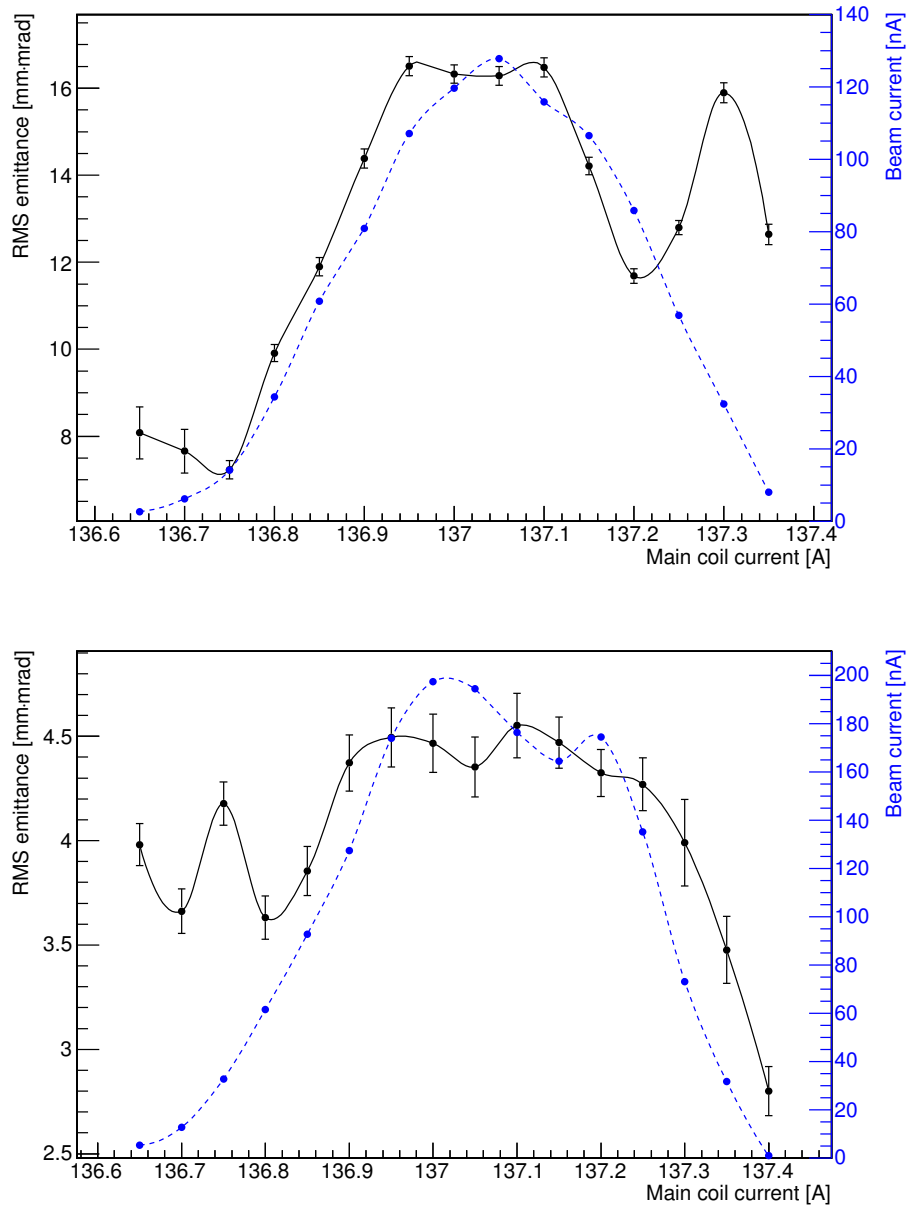


Figure 5.2 – The horizontal (top) and vertical (bottom) transverse RMS emittance as a function of the main coil current for cold machine [35]. The right vertical axis and blue dashed curve correspond to the beam current.

be due to the interception of the beam by the body of the second ion source or to a resonant condition producing beam losses, as reported in reference [24]. In the vertical plane, the variation of the emittance is much smaller and the plateau region is wider, as there is no acceleration in this plane. The measurements were performed

## 5.1. Beam characterization of the 18 MeV Bern cyclotron

several times in consecutive days giving similar results.

The full main coil scan was repeated for both planes when the machine was “warm”, after a few hours of operation. A comparison of the results for the horizontal and vertical plane is presented in figure 5.3 [35]. An offset of the curve corresponding

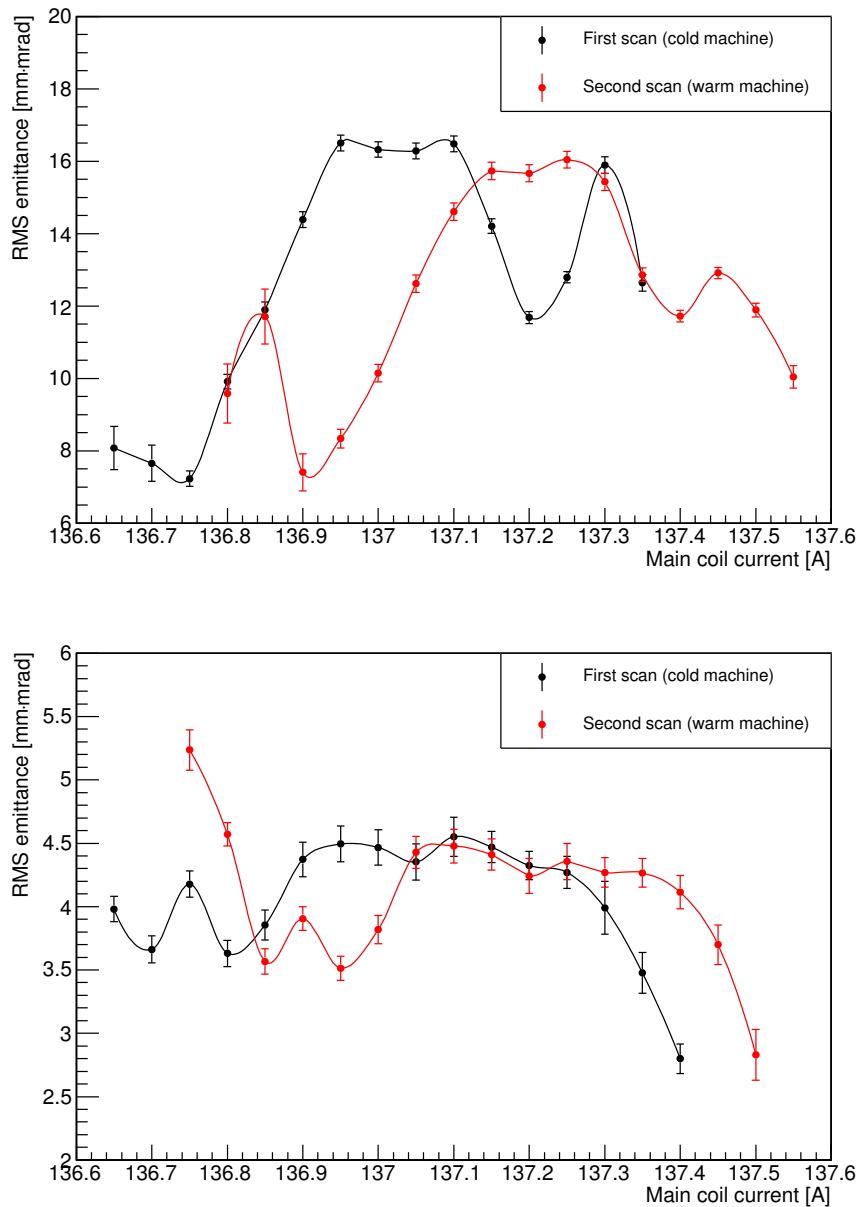


Figure 5.3 – Comparison of the dependency of the horizontal (top) and vertical (bottom) RMS transverse emittance on the main coil current for cold and warm machine [35].

## Chapter 5. Characterization of proton beams

---

to the second scan (for a warm machine) is clearly visible for both the horizontal and vertical planes. This offset is due to the warm-up of the machine showing the tendency of the optimal isochronism to drift towards higher values of the main coil current over the course of the cyclotron operation. The curves for both scans present differences mostly for the extreme values of the main coil current. This is probably due to the fact that change in the range of the main coil operation extends measurable non-isochronous region. Moreover, the regions of very low and very high values of the main coil current are the most unstable.

### Variation of the RF peak voltage

The RF peak voltage of the 42 MHz RF system is responsible for the acceleration and extraction of  $H^-$  ions from the chimney of the ion source. The RF peak voltage was varied from 27 kV to 37 kV with a step of 0.5 kV. The beam current was again monitored by means of a Faraday cup installed at the end of the beamline. The main coil current was set to 137.05 A and 137.00 A for the horizontal and vertical plane, respectively. These values of the main coil current provided operation in the region of the emittance stability (figure 5.2). The results for the horizontal and vertical plane are presented in figure 5.4 [35]. In both planes, oscillations of the measured emittance occur, while the emittance values at the local minima tend to increase. An exact explanation of the observed effects is very difficult, since the centering of the beam is unknown, as there is no differential radial probe inside the machine. Also, the phase of the radial betatron oscillations is not controlled. The changes of the emittance measured at the chosen stripper azimuthal angle are caused by a superposition of the RF voltage modification, beam off-centering, and phase of the betatron oscillations. The total emittance of the extracted beam is a sum of emittances of beam parts extracted at the turns  $N, N + 1, N + 2, \dots$ . One may expect that higher RF voltages reduce the number of turns during acceleration and at the same time enlarge the accepted range of initial RF phases passing from the ion source to the stripper foil. This may be the reason for observing slightly larger beam emittances for larger values of the RF peak voltage.

## 5.1. Beam characterization of the 18 MeV Bern cyclotron

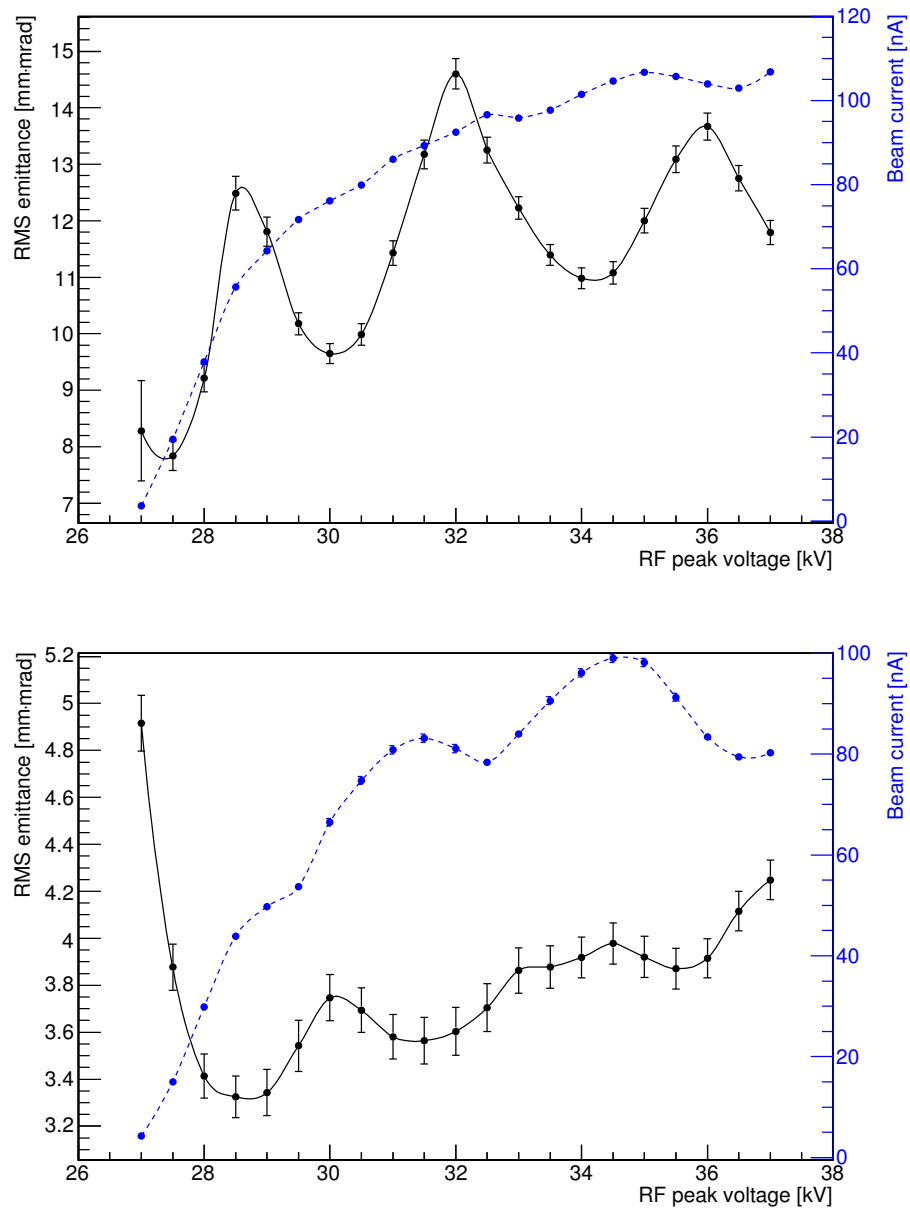


Figure 5.4 – The horizontal (top) and vertical (bottom) transverse RMS emittance as a function of the RF peak voltage [35]. The right vertical axis and blue dashed curve correspond to the beam current.

### Variation of the stripper angle

The stripper angle was varied from the nominal value of  $84.2^\circ$  to  $96.4^\circ$ . The RF peak voltage and the main coil current were set for these measurements to 32 kV and

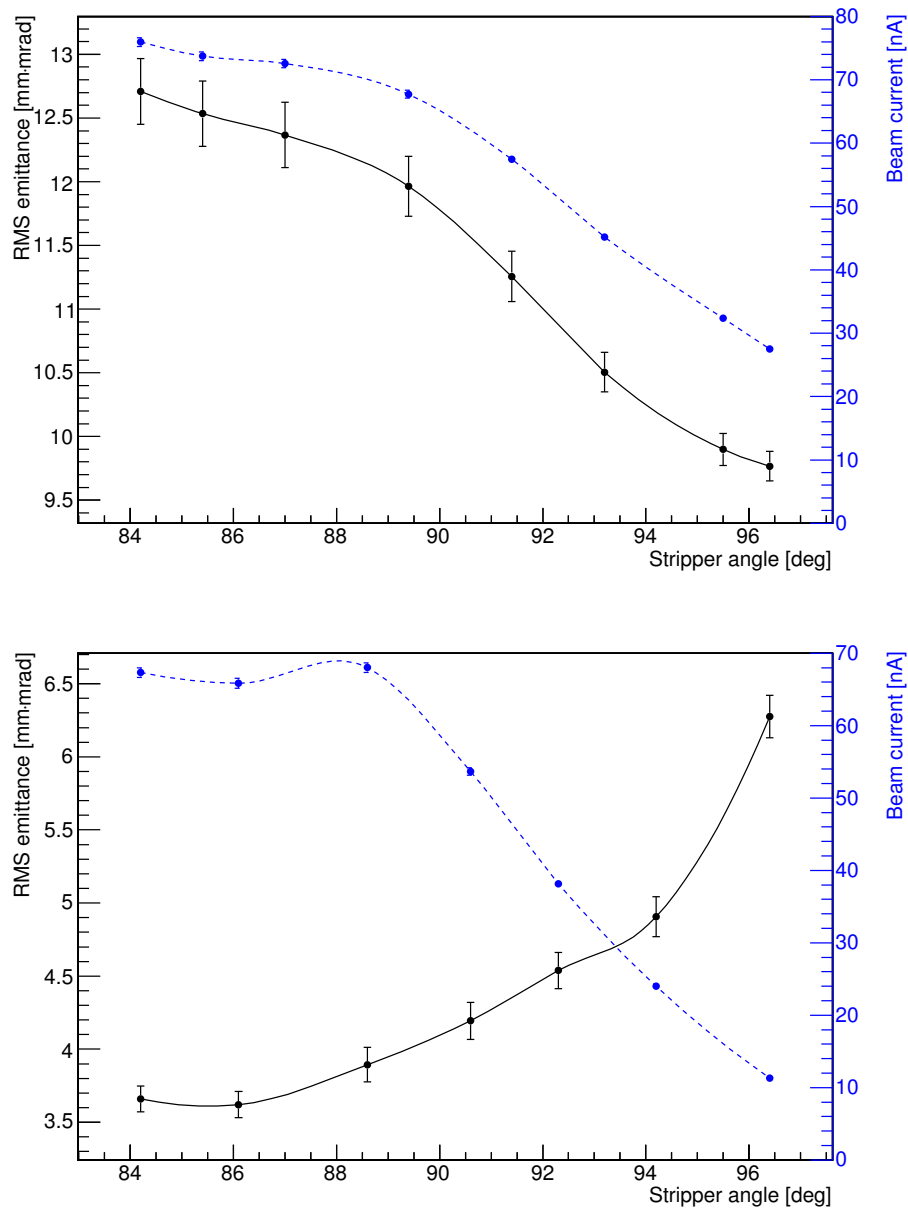


Figure 5.5 – The horizontal (top) and vertical (bottom) transverse RMS emittance as a function of the stripper angle [35]. The right vertical axis and blue dashed curve correspond to the beam current.

137.05 A, respectively. Since the nominal value of the stripper angle is chosen such that the beam intensity is maximal, the beam current monitored by a Faraday cup decreased with increasing angle. The transverse RMS emittance was found to decrease in the horizontal plane (figure 5.5 (top)) and increase in the vertical one (figure 5.5 (bot-

## 5.1. Beam characterization of the 18 MeV Bern cyclotron

tom)) [35]. The interpretation of the obtained result is difficult. It is likely that these changes of the beam emittance would not be observed if the beam was well centered and passed through the stripper in a single turn. Therefore, the results indicate imperfections in the studied machine.

### 5.1.2 Transverse RMS beam emittance for the standard cyclotron settings

For the standard cyclotron settings (table 5.1), the transverse RMS beam emittance was measured with two methods and the results were compared [35, 36]. The first method was the quadrupole variation, described in chapter 2. The strength of the last BTL quadrupole magnet, defocusing in the horizontal plane and focusing in the vertical, was varied and the profiles of the beam were measured with the UniBEaM detector at the known distance from the magnet. The UniBEaM monitor was rotated by 90 degrees for the corresponding measurements in the vertical plane. The second method was the use of multiple beam profilers, for which the <sup>4</sup>PrOBεaM system was again employed. For all the measurements, the standard cyclotron parameters were kept and the beam current, monitored by means of a Faraday cup, was about 250 nA.

For the quadrupole variation method, the estimated variance as a function of the quadrupole current together with the fitted curve, for both horizontal and vertical plane, is reported in figure 5.6 [36]. The fit results for both planes and the corresponding emittance values are reported in table 5.2 [36].

Table 5.2 – Fit parameters and the RMS emittance values obtained by quadrupole variation for both horizontal and vertical planes [36].

Fit parameter	Horizontal plane	Vertical plane
$\sigma_{11}$ [mm <sup>2</sup> ]	$200.23 \pm 0.08$	$21.59 \pm 0.36$
$\sigma_{12}$ [mm·mrad]	$-322.66 \pm 0.08$	$-2.98 \pm 0.07$
$\sigma_{22}$ [mrad <sup>2</sup> ]	$520.80 \pm 0.22$	$1.02 \pm 0.02$
$\tilde{\chi}^2$	0.98	1.04
$\epsilon_{rms}$ [mm·mrad]	$13.08 \pm 0.16$	$3.63 \pm 0.04$

For the multiple beam profiler method, the estimated variance as a function of the

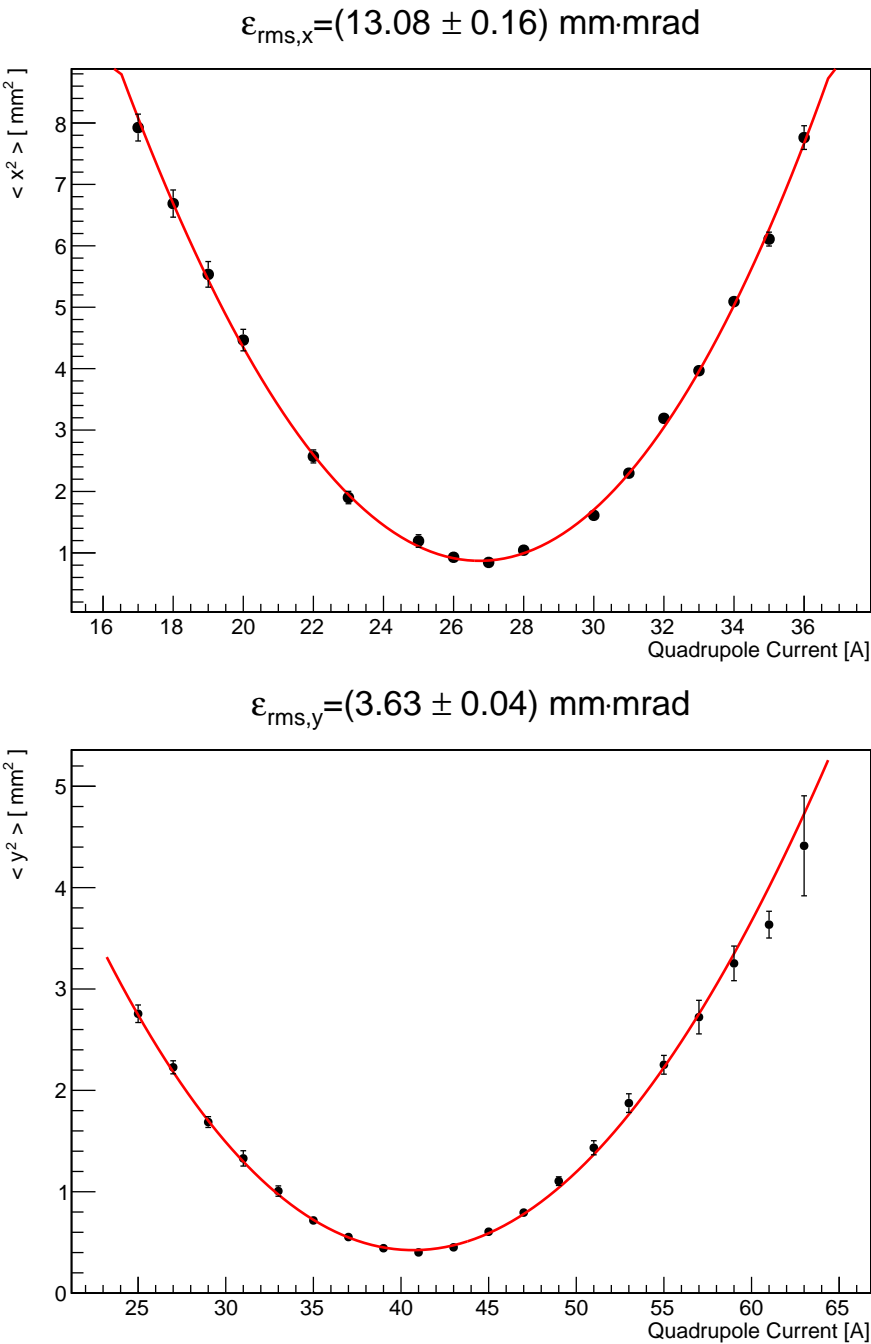


Figure 5.6 – Variance as a function of the quadrupole current obtained for the horizontal (top) and vertical (bottom) planes [36]. The red line corresponds to the best fit.

## 5.1. Beam characterization of the 18 MeV Bern cyclotron

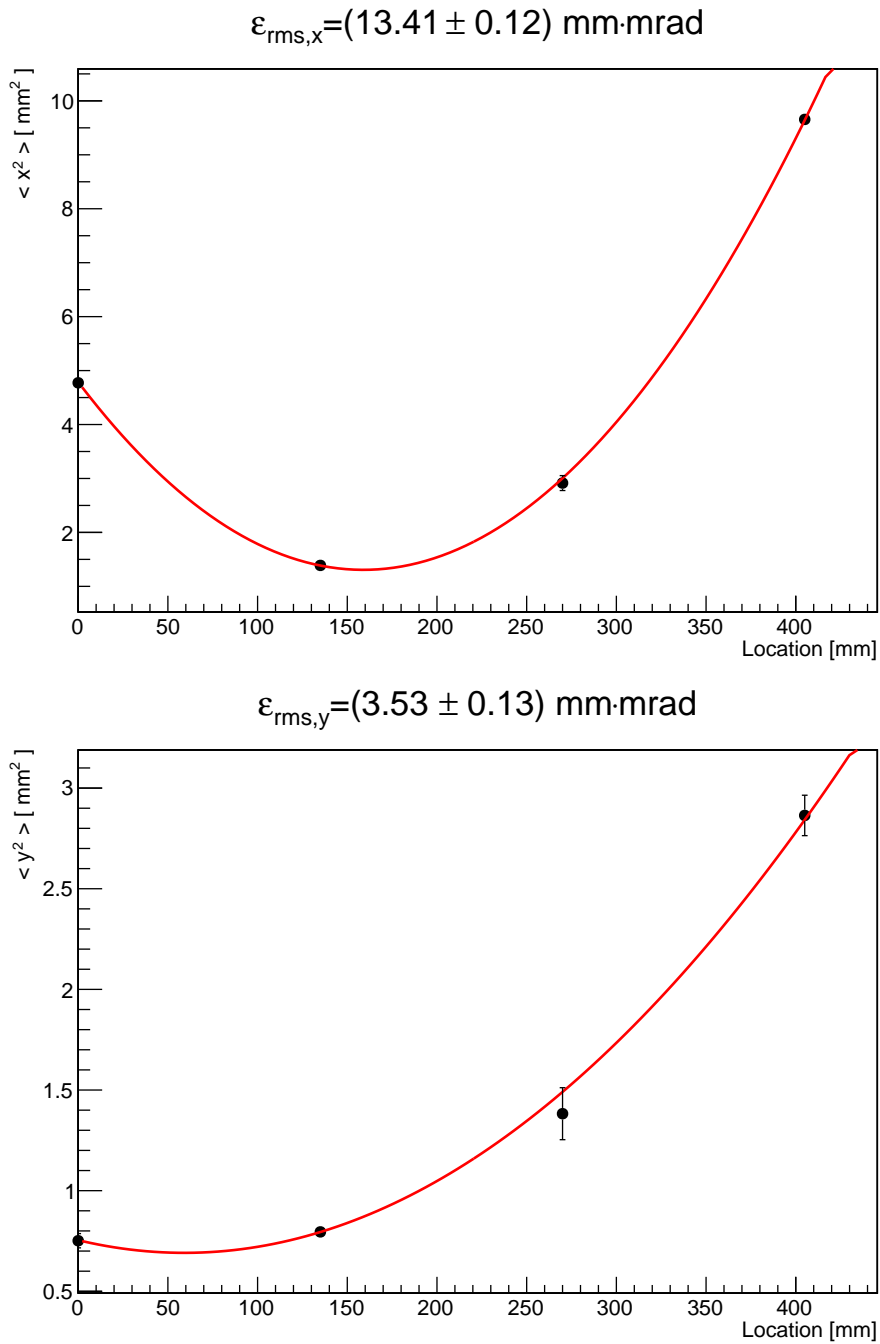


Figure 5.7 – Variance as a function of the location obtained for the horizontal (top) and vertical (bottom) planes [36]. The red line corresponds to the best fit.

## Chapter 5. Characterization of proton beams

---

Table 5.3 – Fit parameters and the RMS emittance values obtained by using multiple profilers for both horizontal and vertical planes [36].

Fit parameter	Horizontal plane	Vertical plane
$\sigma_{11}$ [mm <sup>2</sup> ]	$4.79 \pm 0.09$	$0.75 \pm 0.04$
$\sigma_{12}$ [mm·mrad]	$-21.90 \pm 0.48$	$-1.06 \pm 0.19$
$\sigma_{22}$ [mrad <sup>2</sup> ]	$137.72 \pm 2.06$	$17.99 \pm 1.15$
$\tilde{\chi}^2$	0.47	0.76
$\varepsilon_{rms}$ [mm·mrad]	$13.41 \pm 0.12$	$3.53 \pm 0.13$

location  $s$  together with the fitted curve, for both horizontal and vertical planes, is shown in figure 5.7 [36]. The fit results for both planes and the corresponding emittance values are reported in table 5.3 [36].

The results obtained by employing both methods were found to be in agreement within  $1.65\sigma$  and  $0.71\sigma$  for the horizontal and vertical plane, respectively. The transverse RMS beam emittance in the horizontal plane is almost 4 times bigger than in the vertical plane. This is due to acceleration in the horizontal plane, which causes an increase of the particle position spread along the  $x$ -direction.

### 5.1.3 Proton energy distribution

The energy distribution of particles is an important characteristic of any accelerator. In particular, medical cyclotrons are used for production of radioisotopes where the purity of the product can depend on the energy of incident particles. Therefore, the knowledge of the mean beam energy and its spread allows the production to be more efficient. An example is given in reference [38] for the production of novel PET radioisotopes with the use of solid targets. The energy spread is also an important parameter for the transverse beam dynamics along beamlines. As discussed in chapter 2, it may have a significant influence on the beam envelope. Therefore, to perform a reliable simulation of a beamline, the energy spread of the beam should be assessed.

The nominal energy of the Bern cyclotron is 18 MeV, and the energy spread is caused mostly due to extraction by stripping. Not all of the accelerated  $H^-$  ions are stripped in the same turn. Thus, the difference in radii of the extracted protons result in a

## 5.1. Beam characterization of the 18 MeV Bern cyclotron

Table 5.4 – List of absorbers used for the measurement of the proton energy distribution.

#	Thickness [mm]	Max. proton energy [MeV]
1	1.42	16.0
2	1.50	16.5
3	1.58	17.0
4	1.67	17.5
5	1.75	18.0
6	1.84	18.5
7	1.93	19.0
8	2.02	19.5
9	2.11	20.0

distribution of energies. To characterize the energy distribution of the Bern cyclotron, I used a set of Al absorbers of different thicknesses. Each thickness corresponded to a different maximum beam energy that could be stopped within the absorber (table 5.4), determined by performing a SRIM [39] simulation. For each absorber, a profile of the incident beam was measured by a UniBEaM detector and the intensity of the transmitted beam by a Faraday cup, as illustrated in figure 5.8. The UniBEaM detector was located in front of the absorber and was used to normalize the measured beam current. For the  $i$ -th absorber, the beam profile integral  $S_i$  was calculated and the intensity  $I_i$  of the transmitted beam was obtained from an electrometer. The profile integral holds a linear dependence on the beam current [27]. A reference measurement was performed without any absorber, giving the integral  $S_0$  and the beam current  $I_0$ . The fraction of the beam that was transmitted for each absorber  $T_i$  was calculated with the formula:

$$T_i = \frac{S_0}{S_i} \cdot \frac{I_i}{I_0} \quad i = 1, 2, \dots, 9. \quad (5.1)$$

The probability  $P_{i,i+1}$  of finding a proton with energy between the maximum proton energies of absorbers  $i$  and  $i + 1$  is given by the expression:

$$P_{i,i+1} = T_i - T_{i+1} \quad i = 1, 2, \dots, 8. \quad (5.2)$$

The results are shown in figure 5.9 [35], where the probability density is shown in

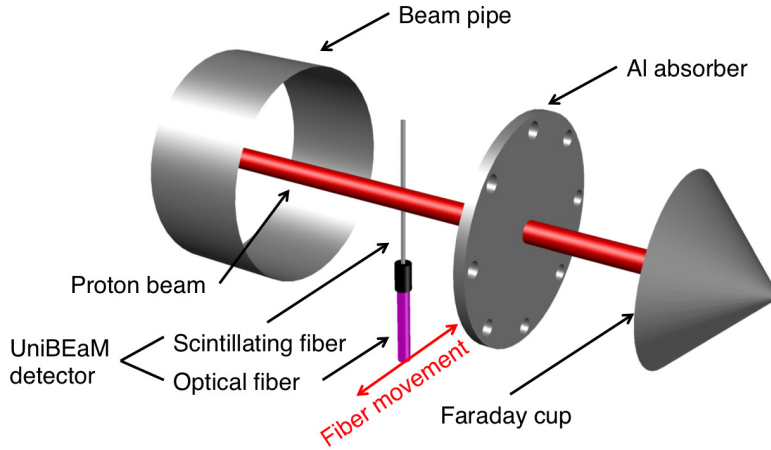


Figure 5.8 – Schematic of the experimental method of the proton energy distribution measurement.

0.5 MeV bins. The mean energy and the RMS of the distribution were found to be  $(18.3 \pm 0.3)$  MeV and  $(0.4 \pm 0.2)$  MeV, respectively. This translates into a fractional energy spread  $\Delta E/E_0$  of 0.02 and the corresponding fractional momentum spread  $\Delta E/E_0$  of 0.01. Additionally, a fit of the Verhulst function was performed with  $\tilde{\chi}^2 = 0.6$ . The Verhulst function was chosen due to a skewness of the measured distribution and it is defined as [40]:

$$P(x) = \frac{1}{A \cdot B} \cdot \frac{(2^A - 1) \cdot \exp\left(\frac{x-C}{B}\right)}{\left(1 + (2^A - 1) \cdot \exp\left(\frac{x-C}{B}\right)\right)^{\frac{A+1}{A}}}, \quad (5.3)$$

where  $A, B$ , and  $C$  are fit parameters. For the best fit, they were found to be:  $A = 0.13 \pm 0.03$ ,  $B = 0.24 \pm 0.02$  MeV, and  $C = 18.76 \pm 0.02$  MeV.

A better resolution of the measurement can be achieved in the future by using a rotating aluminum plate instead of a set of absorbers. The thickness of the material seen by a proton beam would be then defined by the angle between the plate and the beam axis. By this upgrade of the experimental set-up more points could be measured giving a more accurate assessment of the distribution.

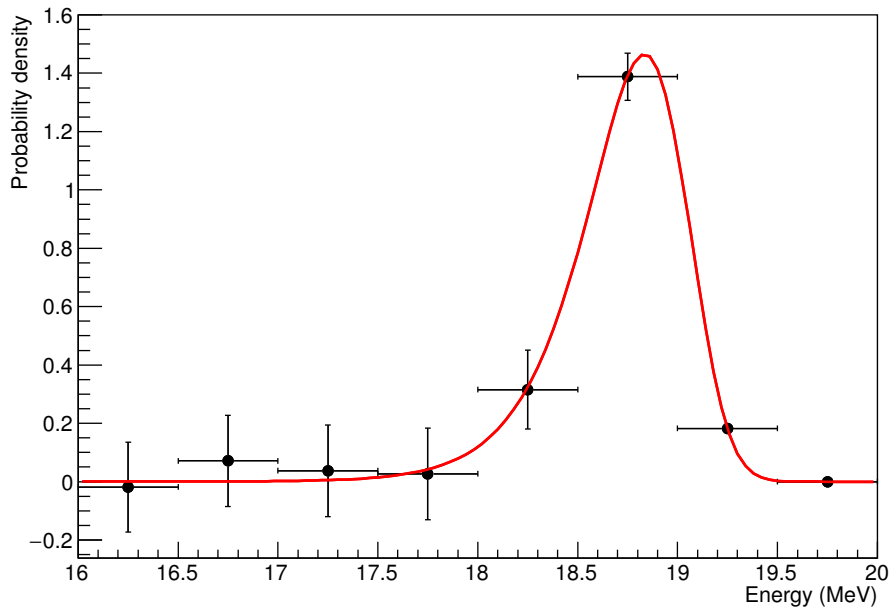


Figure 5.9 – Distribution of the proton energy [35]. Red line corresponds to the best fit of the Verhulst function.

### 5.1.4 Simulation of the Beam Transport Line

Many research activities carried out at the BTL of the Bern cyclotron require a specific shape and size of the beam at different locations along the beamline. Beam optimization is also essential for production of radioisotopes with the use of solid targets [38]. For these purposes, I developed a simulation of the BTL, for which the transverse beam emittances measured with  $^4\text{PrOB}\epsilon\text{aM}$  were an input. The Twiss parameters were calculated at the location of the first beam profiler and transported back to the beginning of the BTL by means of linear beam transport algebra. In this way the beam phase space at the injection point to the BTL was reconstructed assuming Gaussian distributions of  $(x, x')$  and  $(y, y')$ , leading to phase space ellipses. As an example, the  $1\sigma$ -ellipses for the standard cyclotron settings are reported in figure 5.10. Since the energy spread of the proton beam produced by the Bern cyclotron was found to be only 2 %, the beam envelope correction, as described in chapter 2, is not implemented. All the drift lengths and quadrupole characteristics are based on the detailed documentation provided by the manufacturer and additional measurements performed by

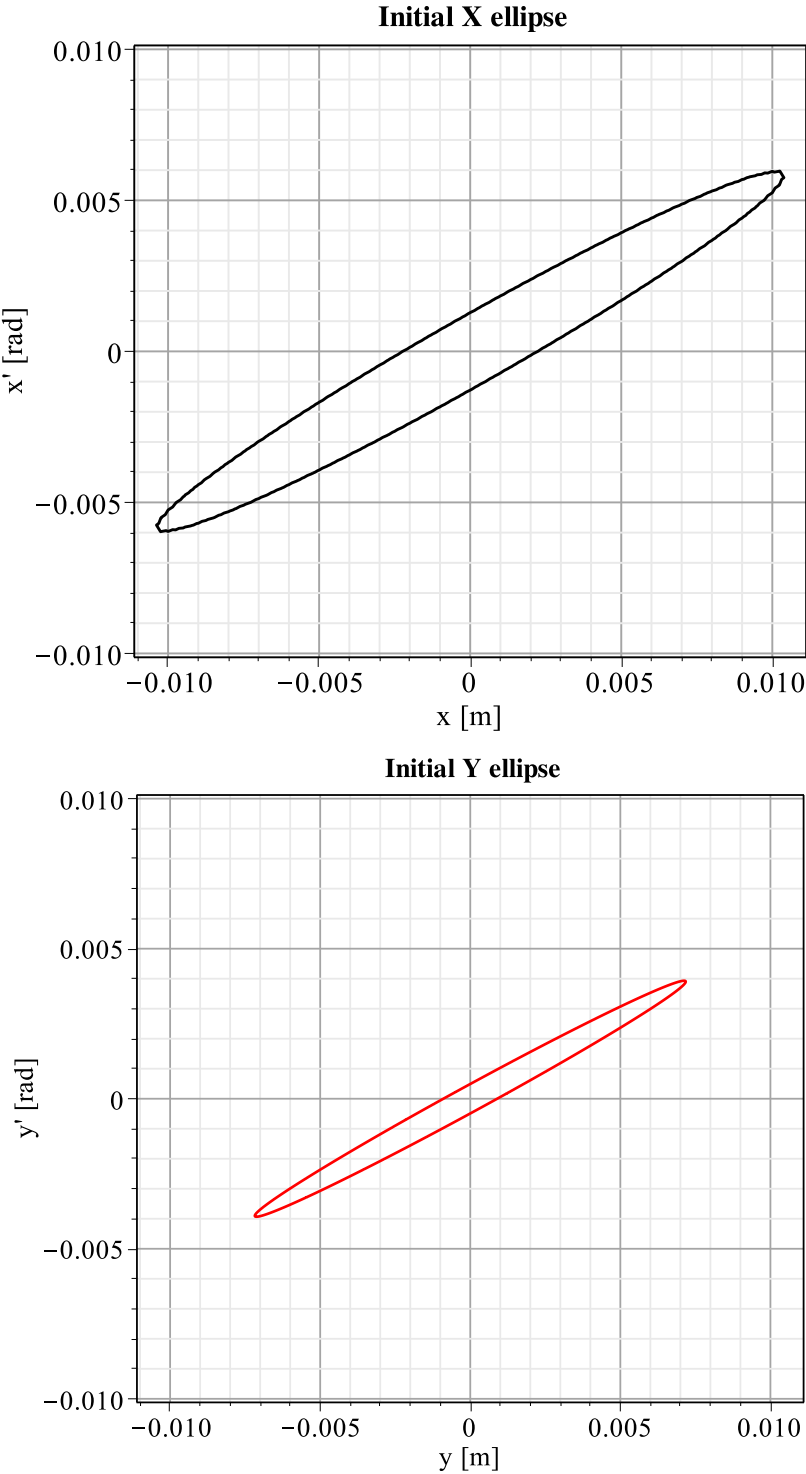


Figure 5.10 – The horizontal (top) and vertical (bottom)  $1\sigma$ -phase-space ellipses at the injection to the BTL.

## 5.1. Beam characterization of the 18 MeV Bern cyclotron

me. The simulation has been implemented in Maple [41] and Methodical Accelerator Design (MAD-X) [42]. The former is a symbolic and numeric computing environment, as well as a multi-paradigm programming language and was developed by Waterloo Maple Inc.. The latter is a multi-purpose tool for charged-particle optics design and studies in alternating-gradient accelerators and beamlines developed and maintained by the Beams Department at CERN.

The simulation implemented in Maple is an easy to use tool for online tuning of the cyclotron parameters. The user, by turning the knobs, can adjust the current at each quadrupole, as illustrated in figure 5.11. The beam envelopes in both planes are then calculated with the beam transport linear algebra and displayed. Additionally, the evolution of the phase space ellipse can be tracked with a corresponding animation. Apart from the calculation of the beam envelope, the user can choose the number of particles to be simulated (multi-particle mode in figure 5.11) and tracked through the beamline. The particles are generated from a Gaussian source corresponding

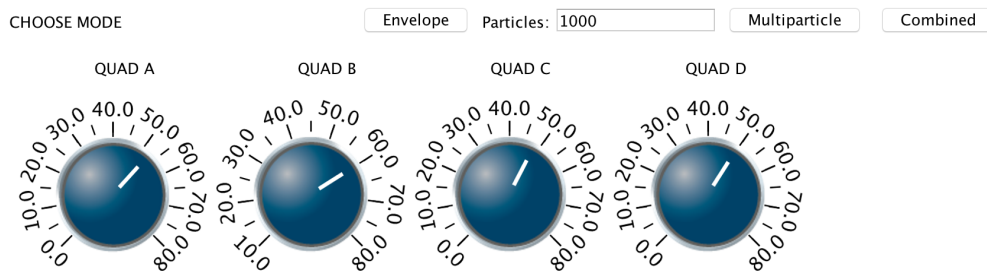


Figure 5.11 – User interface of the BTL simulation in Maple. Three different modes of operation can be chosen. Each knob corresponds to the current at one quadrupole of the BTL.

to the reconstructed phase space at the injection to the BTL. The combined mode (figure 5.11) can also be chosen, in which both the calculation of the beam envelope and the particle tracking are performed simultaneously. As an example, the output of the combined mode for 1000 particles for the horizontal plane is shown in figure 5.12. A numerical value of the calculated beam size at each beamline element can be easily accessed and stored. The same applies to the positions of tracked particles. When the multi-particle, or combined, mode is chosen, the histogram representing the beam profile at previously defined location along the beamline is automatically plotted, as

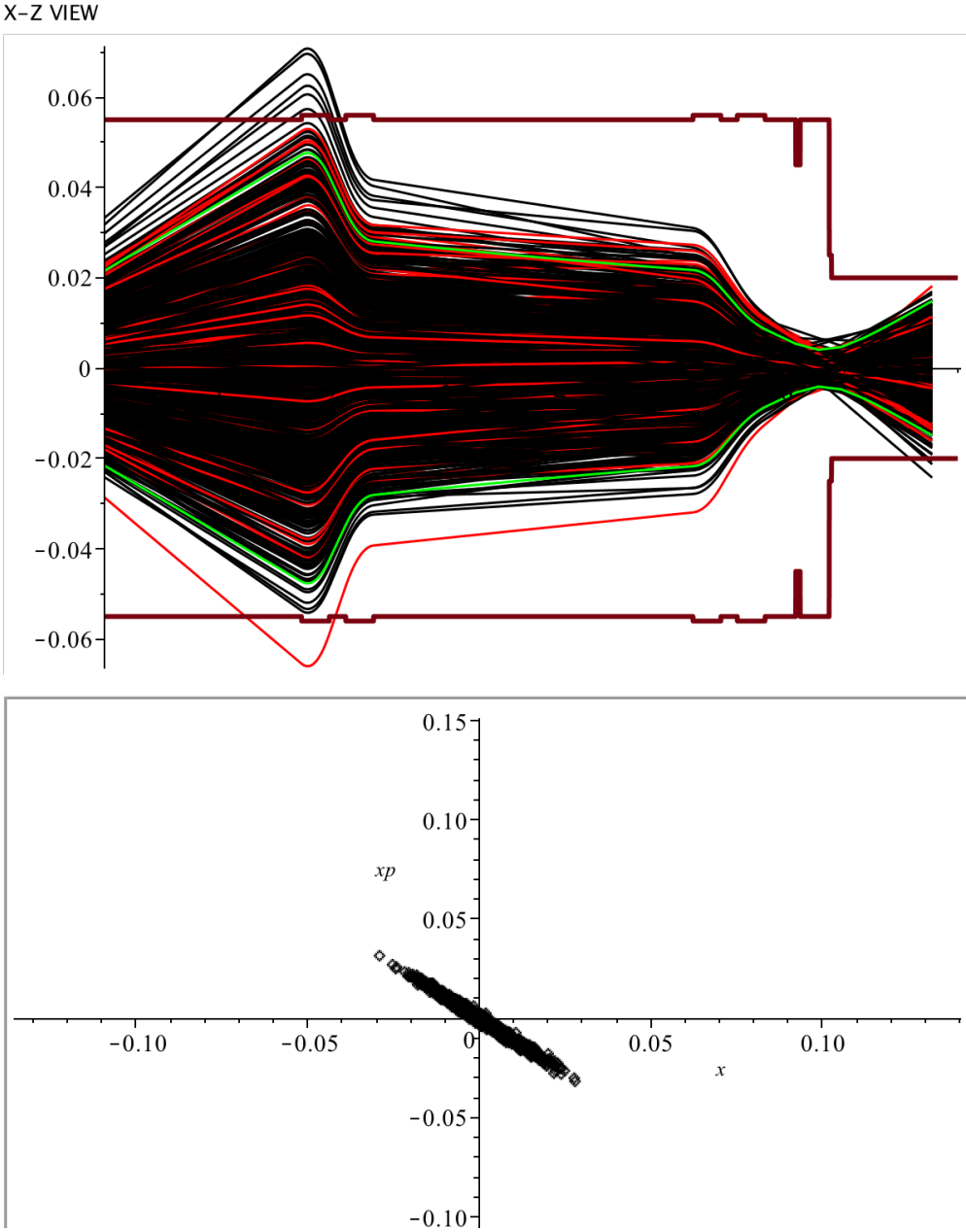


Figure 5.12 – Output of the BTL simulation in Maple for the horizontal plane. The black and red rays correspond to 1000 tracked particles, the green line represents the beam envelope. On the bottom, the phase space evolution is shown. All the positions are given in meters, and the angles in radians.

shown in figure 5.13.

The simulation implemented in MAD-X consists of a beamline defined as a sequence of beam optics component. The Twiss parameters at their locations are calculated. An

## 5.1. Beam characterization of the 18 MeV Bern cyclotron

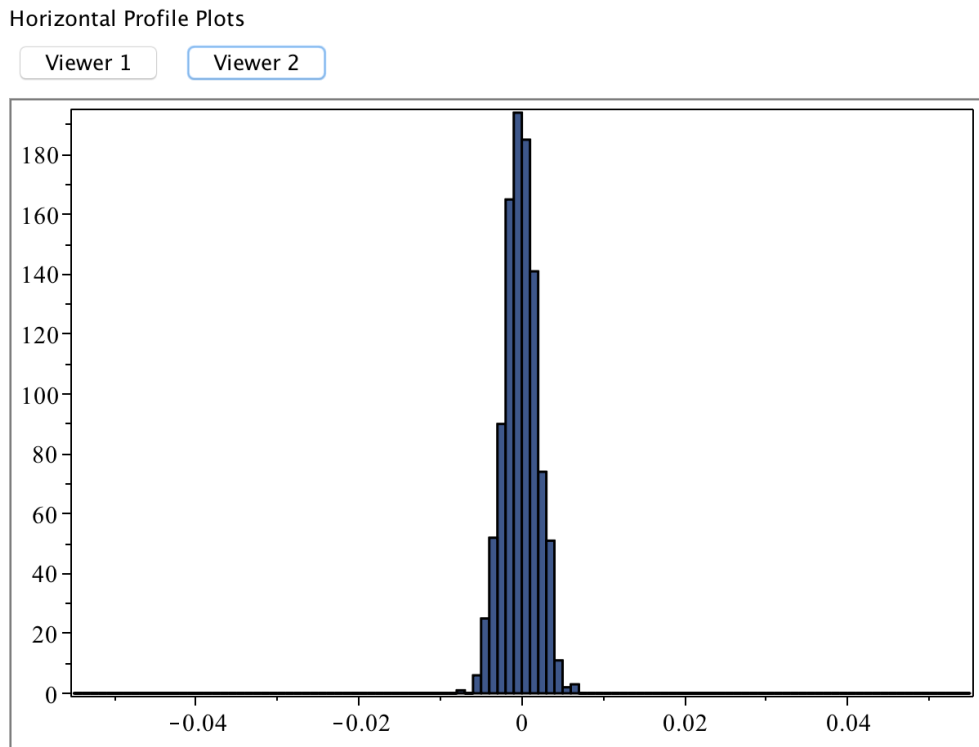


Figure 5.13 – Histogram representing a beam profile at a chosen location along the BTL. The entries correspond to 1000 simulated particles. The position is given in meters.

advantage of the MAD-X simulation, with respect to the one developed in Maple, is the possibility of finding optimal quadrupole settings by defining constraints which correspond to the beam size required at a chosen location. The values of the quadrupole currents are then obtained as an output of the MAD-X matching algorithm. Although the beam envelope correction corresponding to the energy spread is usually not used due to its negligible value for the BTL, it can be easily added in the configuration file. In figure 5.14, the simulated beam envelope in both horizontal and vertical planes for the standard cyclotron parameters and standard quadrupole settings is presented. The disadvantages of the MAD-X simulation are a certain complexity of its use and the lack of the graphical interface.

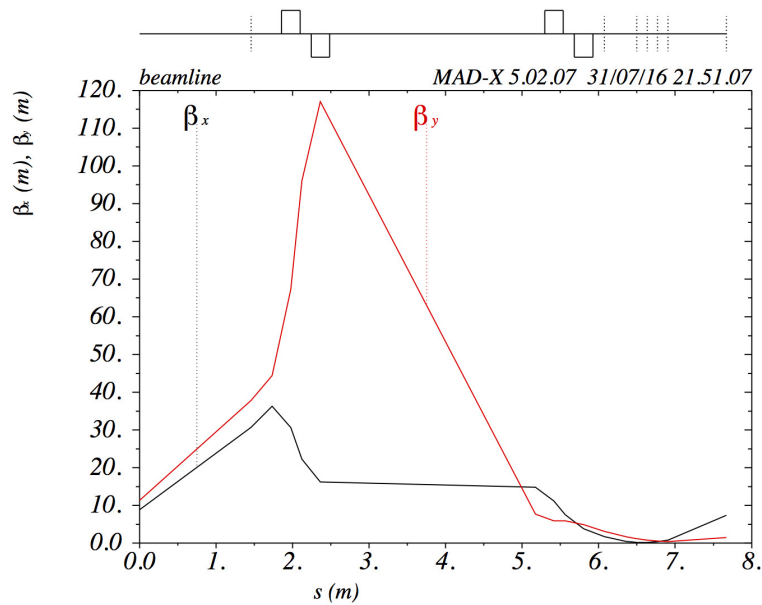


Figure 5.14 – Simulated beam envelope in both horizontal and vertical planes.

## 5.2 Transverse beam emittance of the TR24 Strasbourg cyclotron

The CYRCé cyclotron (CYclotron pour la ReCherche et l'Enseignement) is installed at IPHC (Institut Pluridisciplinaire Hubert Curien) in Strasbourg (France), designed for the development of new radiolabeled molecules based on the research and production of radioisotopes for medical diagnostics and treatments. The heart of the facility is the TR24 cyclotron, shown in figure 5.15, produced by ACSI (Canada), which delivers a 16-25 MeV proton beam to two extraction ports with intensities ranging from fractions of a pA to 500  $\mu$ A. Such a wide beam intensity range is possible due to the external CUSP  $H^-$  ion source with an axial injection beamline [43, 44].

Some preliminary assessments of the transverse beam emittance of the Strasbourg cyclotron have already been performed [45]. However, there was still a need for a fast and reliable emittance measurement for the two most frequently used energies, 18 and 25 MeV, and different settings of the stripper azimuthal angle. I performed these measurements with the  $^4\text{PrOB}\epsilon\text{aM}$  system installed on the long beamline attached to the one of the cyclotron outputs, as shown in figure 5.16. The measurements were

## 5.2. Transverse beam emittance of the TR24 Strasbourg cyclotron



Figure 5.15 – The TR24 cyclotron and its beamline at IPHC in Strasbourg.



Figure 5.16 – The  $^4\text{PrOBaM}$  system installed on the beamline of the TR24 cyclotron in Strasbourg.

taken in both the horizontal and vertical planes by turning the system by 90 degrees around the beam axis. The beam current was kept at about 10 nA and monitored by a Faraday cup, which terminated the beamline.

The RMS transverse emittance was measured for three different positions of the

## Chapter 5. Characterization of proton beams

stripper at both beam energies, 18 MeV and 25 MeV. As an example, the measurement performed for the 18 MeV proton beam with the typical position of the stripper is presented in figure 5.17.

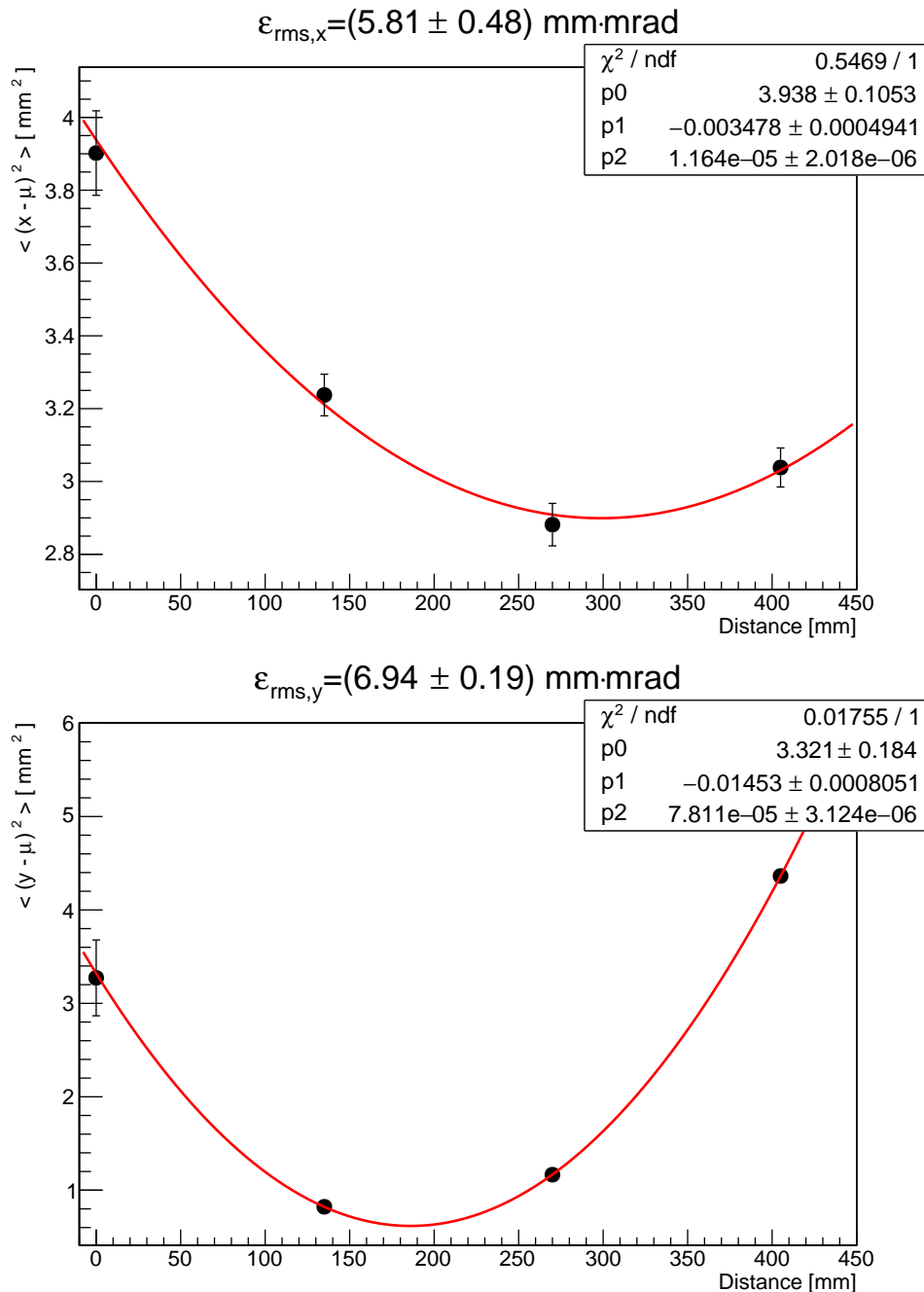


Figure 5.17 – Variance as a function of the location obtained for the horizontal (top) and vertical (bottom) planes. The fit parameters are given in the inset.

## 5.2. Transverse beam emittance of the TR24 Strasbourg cyclotron

---

The results of the emittance measurements for different stripper positions are shown in figures 5.18 and 5.19 for beam energies of 18 MeV and 25 MeV, respectively. The stripper positions chosen are those, which are used most often at IPHC and are given by a numerical parameter. For 18 MeV protons, the horizontal emittance varied from  $5.01 \pm 0.28$  mm·mrad to  $5.81 \pm 0.48$  mm·mrad, increasing by 16 % with the change of the stripper position. The vertical emittance varied from  $5.04 \pm 0.17$  mm·mrad to  $6.94 \pm 0.19$  mm·mrad, increasing by 38 % with the change of the stripper position. For 25 MeV protons, the dependence on the stripper position is weak. This, however, cannot be directly compared with the measurements for the 18 MeV beam, since the range in which the stripper positions was changed is different. In the horizontal plane, the emittance varied from  $2.79 \pm 0.21$  mm·mrad to  $3.03 \pm 0.22$  mm·mrad, increasing by 8 % with the change of the stripper position. The vertical emittance varied from  $5.76 \pm 0.18$  mm·mrad to  $5.96 \pm 0.16$  mm·mrad, increasing by 4 % with the change of the stripper position. The measured value of the vertical RMS beam emittance is always larger than the corresponding value of the horizontal one. This is probably due to the axial injection of  $H^-$  ions from the external source. Acceleration from the injection point to the extraction stripper is realized in the horizontal plane, and therefore the axially injected ions must be deflected by 90 degrees, which leads to emittance growth in the vertical plane.

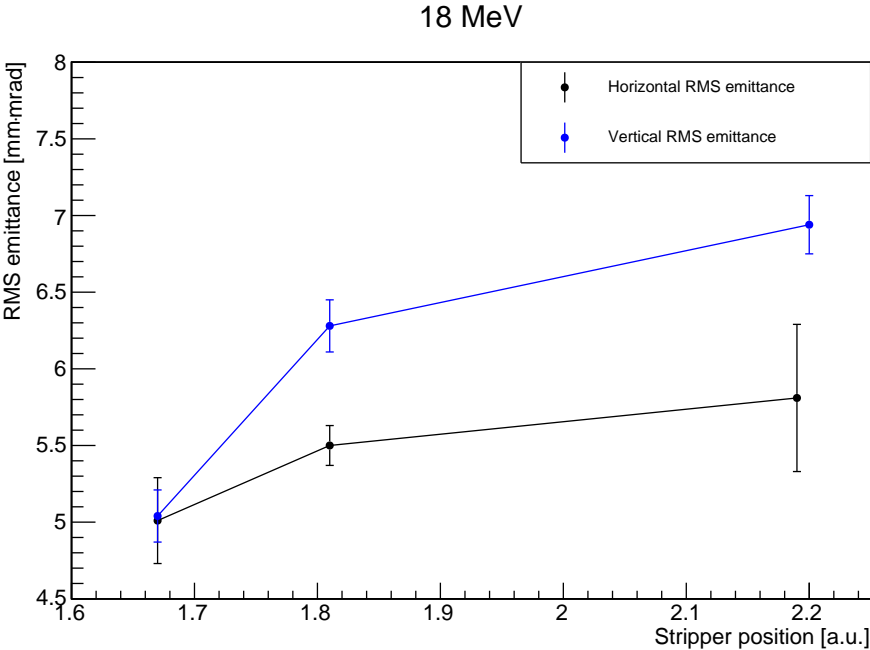


Figure 5.18 – The RMS transverse beam emittance of the 18 MeV proton beam of the TR24 Strasbourg cyclotron as a function of stripper position.

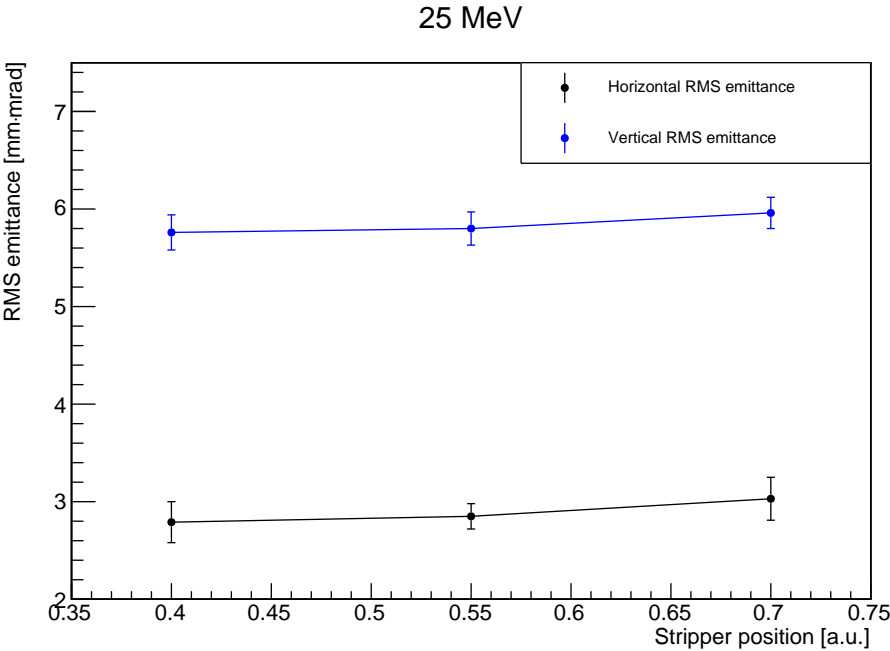


Figure 5.19 – The RMS transverse beam emittance of the 25 MeV proton beam of the TR24 Strasbourg cyclotron as a function of stripper position.

## Conclusions

The work presented in this thesis was focused on the development of a compact system for making online measurements of transverse beam emittance. Since the  ${}^4\text{PrOB}\epsilon\text{aM}$  system is based on the UniBEaM detector for monitoring ion beams, the achievements of this work encompass the development of this beam profiler, its successful beam tests, and its commercialization. The UniBEaM monitor can operate in a wide intensity range and with various ion beams. The results obtained at the Bern medical PET cyclotron show good performance of this compact and simple device with continuous proton beams for currents from 1 pA to 20  $\mu\text{A}$ . A specific version of the detector was also employed in monitoring high-energy proton and pion beams, which is the first step towards extension of its possible applications. The commercial version of the UniBEaM is already deployed for beam diagnostics in a few laboratories around the world. Both laboratory and commercial versions of the profiler are used in many ongoing research activities at the Bern cyclotron laboratory, such as the assessment of radiation hardness of electronic components, cross-section measurements or production of novel PET radioisotopes with solid targets.

The  ${}^4\text{PrOB}\epsilon\text{aM}$  system, which consists of four UniBEaM profilers, is an easy-to-use instrument for making measurements of transverse beam emittance quickly. It can be installed along any beamline or directly at the outport of an accelerator. Since the measurement technique is based on the use of multiple beam profilers, prior knowledge of the beam optics elements of the beamline is not necessary. This feature is especially important at some accelerator facilities, which are not focused on research in the field of accelerator physics, and thus information on, for instance, quadrupole characteristics is limited. I developed the  ${}^4\text{PrOB}\epsilon\text{aM}$  system together

## Conclusions

---

with dedicated software for its operation and online data analysis. This system allows one measurement of the beam emittance to be performed in less than a minute. Fast monitoring of the beam emittance is useful for beamline commissioning and studies of machine imperfections. This was shown in the study of the transverse beam emittance as a function of various cyclotron parameters, carried out at the BTL of the Bern cyclotron. These measurements indicate imperfections of the machine, characterize different operation conditions, and allow irradiations to be optimized accordingly. On the basis of the measurements performed with  $^4\text{PrOB}\epsilon\text{aM}$  at the Bern cyclotron laboratory, I developed a simulation of the BTL, which is important for conducting multi-disciplinary research activities. To complete the characterization of the Bern cyclotron, I also proposed a method based on aluminum absorbers different thickness, a UniBEaM detector, and a Faraday cup to measure the proton energy distribution. The results obtained are important for some experiments, for instance, the production of new PET radioisotopes.

The  $^4\text{PrOB}\epsilon\text{aM}$  system was also deployed for the measurements of the transverse beam emittance at the TR24 cyclotron at IPHC in Strasbourg. The results of this study will be used for further accelerator physics and beamline developments in the CYRCé laboratory. One could well envisage the use of the system in other research facilities, and eventually its commercialization.

# A Appendix

In this appendix, I reprint the publications related to the presented thesis. I am the first author of papers 5 and 6, and the corresponding author of paper 3.

1. M. Auger, K. P. Nesteruk et al., *Low current performance of the Bern medical cyclotron down to the pA range*, Meas. Sci. Technol. **26**: 094006, 2015
2. M. Auger, K. P. Nesteruk et al., *A detector based on silica fibers for ion beam monitoring in a wide current range*, JINST **11**: P03027, 2016
3. M. Auger, K. P. Nesteruk (*corresponding author*) et al., *UniBEaM: a silica fiber monitor for charged particle beams*, Proceedings of WTTC16, Santa Fe (NM), USA, AIP Conf. Proc. **1845**:020015, 2016
4. D. E. Potkins, K. P. Nesteruk et al., *A low-cost beam profiler based on cerium-doped silica fibers*, Proceedings of CAARI-16, Fort Worth (TX), USA, Physics Procedia (*submitted*)
5. K. P. Nesteruk et al., *A system for online beam emittance measurements and proton beam characterization*, JINST (*submitted*, Ref. JINST\_102P\_0517, arXiv:1705.07486)
6. K. P. Nesteruk et al., *Study of the transverse beam emittance of the Bern medical cyclotron*, Proceedings of IBIC2015, Melbourne, Australia, MOPB041:134-138, 2015, <http://www.jacow.org>



# Low current performance of the Bern medical cyclotron down to the pA range

M Auger<sup>1</sup>, S Braccini<sup>1</sup>, A Ereditato<sup>1</sup>, K P Nesteruk<sup>1</sup> and P Scamporrì<sup>1,2</sup>

<sup>1</sup> Albert Einstein Center for Fundamental Physics, Laboratory for High Energy Physics, University of Bern, Sidlerstrasse 5, CH-3012 Bern, Switzerland

<sup>2</sup> Department of Physics, University of Napoli Federico II, Complesso Universitario di Monte S. Angelo, I-80126, Napoli, Italy

E-mail: [antonio.ereditato@lhep.unibe.ch](mailto:antonio.ereditato@lhep.unibe.ch)

Received 14 November 2014, revised 6 July 2015

Accepted for publication 7 July 2015

Published 30 July 2015



## Abstract

A medical cyclotron accelerating  $H^-$  ions to 18 MeV is in operation at the Bern University Hospital (Inselspital). It is the commercial IBA 18/18 cyclotron equipped with a specifically conceived 6 m long external beam line ending in a separate bunker. This feature is unique for a hospital-based facility and makes it possible to conduct routine radioisotope production for PET diagnostics in parallel with multidisciplinary research activities, among which are novel particle detectors, radiation biophysics, radioprotection, radiochemistry and radiopharmacy developments. Several of these activities, such as radiobiology experiments for example, require low current beams down to the pA range, while medical cyclotrons are designed for high current operation above  $10 \mu A$ . In this paper, we present the first results on the low current performance of a PET medical cyclotron obtained by ion source, radio-frequency and main coil tuning. With this method, stable beam currents down to  $(1.5 \pm 0.5)$  pA were obtained and measured with a high-sensitivity Faraday cup located at the end of the beam transport line.

Keywords: particle accelerator, medical cyclotron, low beam current

(Some figures may appear in colour only in the online journal)

## 1. Introduction

The establishment of a cyclotron laboratory at the Bern University Hospital (Inselspital) was made possible by a partnership between the Inselspital, the University of Bern (Physics and Radiochemistry) and private investors. This new centre [1] has a twofold purpose. It was principally conceived for top-level radioisotope production for positron emission tomography (PET) by means of the most advanced industrial good manufacturing practice (GMP) technologies. In addition, it was decided to exploit the high potential of this kind of facility for research activities in different fields [2]. Only rarely is a research and development programme pursued with a PET medical cyclotron, apart from clinical studies performed with the produced radiotracers. Nevertheless, valuable developments on accelerator physics, novel particle detectors, radiation protection, radiation biophysics and materials science can be performed, provided that regular access to the beam area is possible without limiting the routine use

of the accelerator. Considering the severe restrictions due to radiation protection in radioisotope production machines, an external beam transport line (BTL) terminating in a separate bunker was included in the design of the facility [3]. Although more complex and unusual for a hospital-based accelerator, this solution allows the continuation of radioisotope production and multidisciplinary research activities in an independent and efficient way. Furthermore, several of the above mentioned research activities need low beam currents down to the pA range, while PET cyclotrons are designed and optimised for operation above  $10 \mu A$ . To the authors' knowledge only the cyclotron of the University of Coimbra is operating a PET cyclotron for radiobiological applications [4]. There, low currents were obtained by long drift distances and without the use of a beam transport line.

The Bern cyclotron laboratory started operation at the end of 2012 and since then studies on particle detectors and air contamination have successfully been performed [5–8], and many other scientific activities are underway. A study on the



**Figure 1.** The Bern cyclotron opened during commissioning. The part of the BTL located in the cyclotron bunker is visible, pointing towards the wall separating the two bunkers.

possibility of reducing the beam currents down to the nano-ampere and even picoampere range was performed and is presented in this paper. It has to be remarked that the stable operation of the IBA 18/18 cyclotron is only guaranteed above  $10 \mu\text{A}$ . Furthermore, specific low irradiation conditions have to be reached without interfering with the daily radioisotope production for PET imaging. In this framework, low current performances were studied by acting in combination only on the ion source arc current, on the radio-frequency peak voltage and on the current in the main coil. On this basis, the beams can be further reduced in intensity and shaped by using collimators and compensators according to the specific need.

## 2. The Bern cyclotron and its beam transport line

The core of the facility is the IBA Cyclone 18 MeV cyclotron shown in figure 1. It is equipped with two  $\text{H}^-$  ion sources, a redundancy aimed at maximising the efficiency for daily medical radioisotope production. It provides large beam currents up to  $150 \mu\text{A}$  in single or dual beam mode. Extraction is achieved by stripping the negative ions with  $5 \mu\text{m}$  thick pyrolytic carbon foils. In dual beam mode, the beam is extracted by two strippers located at an angular distance of about  $180^\circ$  from each other. The position of the last orbit can be tuned such that different currents can be extracted in the two out-ports. Although difficult to obtain, this feature was required for the Bern cyclotron in order to run two targets at the same time and produce two different radioisotopes. The main technical data of the Bern cyclotron are summarised in table 1.

When operating at high beam currents, optimised vertical focusing and longitudinal phase stability are essential. This is realised by alternating along the accelerator circumference four  $60^\circ$  sectors at high magnetic field (*hills*) with four  $30^\circ$  sectors at low magnetic field (*valleys*). This implies that the particle orbits are not circular and that, during the construction, a complex and iterative mapping procedure is required

**Table 1.** Main characteristics of the Bern cyclotron and its beam transport line.

Constructor	Ion beam applications (IBA), Belgium
Type	Cyclone 18/18 HC
Accelerated particles	$\text{H}^-$ ( $\text{D}^-$ on option)
Energy	18 MeV (9 MeV for $\text{D}^-$ )
Maximum current	$150 \mu\text{A}$ ( $40 \mu\text{A}$ for $\text{D}^-$ )
Number of sectors	4
Angle of the dees	$30^\circ$
Magnetic field	1.9 T on the hills and 0.35 T on the valleys
Radio frequency	42 MHz
Weight	24 000 kg
Dimensions	2 m diameter, 2.2 m height
Ion sources	2 internal PIG $\text{H}^-$
Extraction ports	8 (one of which connected with the BTL)
Extraction	Carbon foil stripping (for single or dual beam)
Strippers	Two per extraction port on a rotating carousel
Isotope production targets	4 $^{18}\text{F}^-$ ( $^{15}\text{O}$ , $^{11}\text{C}$ and solid target are foreseen)
BTL	6.5 m long; two quadrupole doublets (one in each bunker); XY steering magnet; upstream collimator; 2 beam viewers; neutron shutter

to obtain a precise magnetic field. It has to be noted that a fine tuning of the cyclotron can be performed only on site by measuring the accelerated beam. In particular, the magnetic field of the Bern cyclotron was carefully set in the central region to obtain the optimal transmission of the low energy ions produced by the source. An iterative procedure was

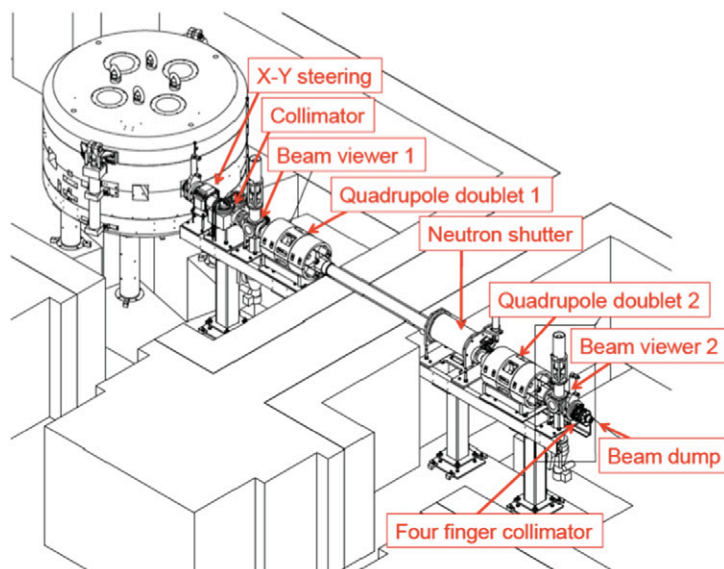


**Figure 2.** Schematic view of the Bern cyclotron facility, where all the main elements of the BTL are highlighted.

applied aimed at modifying the gap of the magnet in the central region (*shimming*).

The radioisotope production performance of the Bern cyclotron is excellent when compared with modern standards [9, 10]. In particular, 500 GBq of  $^{18}\text{F}$  can be produced with dual beam irradiation in less than 70 min. Considering the total efficiency of the chemical synthesis (usually about 60%), this corresponds to a production of about 250 GBq of fluoro-deoxyglucose (FDG) in a single run. With this apparatus, even larger productions would be possible, but 500 GBq is the legal radiation protection limit for a laboratory of this type (classified as B) in Switzerland.

As already mentioned, a 6 m long BTL ending in a separate bunker is installed in Bern, which is quite uncommon for a PET medical cyclotron. These accelerators are usually equipped only with targets located right after the strippers and very rarely with one  $\sim 2$  m long beam line, dedicated to the bombardment of solid targets and located in the same bunker as the cyclotron. The BTL is able to transport the maximum current of  $150\ \mu\text{A}$  with more than 95% transmission efficiency and was designed, realised and commissioned with contributions from our group. High transmission is crucial to limiting unwanted activation and to protecting scientific equipment sensitive to radiation. Furthermore, this performance is important in view of future developments since remarkable progress is presently ongoing on targets that can withstand very large currents. At the same time, currents down to fractions of nA are needed for research purposes, and beams of different sizes ranging from a few millimetres to a few centimetres in diameter on target have to be obtained. Examples are radiation biology (flat beams of  $\sim 1\ \text{cm}^2$ ,  $\sim 1\ \text{pA}$ ), PIXE and PIGE ion beam analysis (beams of  $\sim 1\ \text{mm}^2$ ,  $\sim 1\ \text{pA}$ ), cross section measurements (beams of  $\sim 10\ \text{mm}^2$ ,  $\sim 10\ \text{nA}$ ). To fulfill these goals, specific solutions were implemented and the initial industrial design was modified accordingly [4].

A schematic view of the BTL is shown in figure 2. The alternate focusing and defocusing of the BTL is realised

by two horizontal–vertical (H–V) quadrupole doublets, the former located in the cyclotron bunker and the latter in that of the BTL. An unavoidable design constraint is represented by the distance between the two quadrupole doublets due to the 180 cm thick wall separating the two bunkers. This thickness is due to radiation protection issues since considerably fast neutron fluxes are generated during radioisotope production, for example, via (p,n) reactions. For the same reason, a movable cylindrical neutron shutter is located inside the beam pipe when the BTL is not in use. In this way, the penetration of neutrons to the second bunker through the beam pipe is minimised. Taking into account the space needed for the vacuum pumps, beam diagnostics, collimators and other devices, the beam line is 6.5 m long. For scientific activities, experimental equipment such as particle detectors or specific target stations are installed at the end of the BTL.

### 3. Experimental set-up

The study presented in this paper is based on the tuning of the ion source, the radio-frequency (RF) and the current in the main coil as well as on the precise measurement of the beam current at the end of the BTL. Since currents in the nA and pA range are uncommon for PET cyclotrons, commercial instrumentation is not standard. For this reason, a specific apparatus was developed by our group.

For the measurement of the beam current in the BTL, the two viewers and the beam dump shown in figure 2 are equipped with a read-out device integrated in the control system of the cyclotron. When one of the viewers is lowered to intercept the beam, it acts as a Faraday cup and the beam current can be measured by an ammeter. With this method, a sensitivity, namely the minimal measurable current, of the order of 10 nA can be reached. This system is therefore not suitable for the investigation of the intensity range (from a few pA to a few nA) we are aiming at in this work. For this purpose, a



**Figure 3.** The high sensitivity Faraday cup installed at the end of the BTL for low current performance studies.

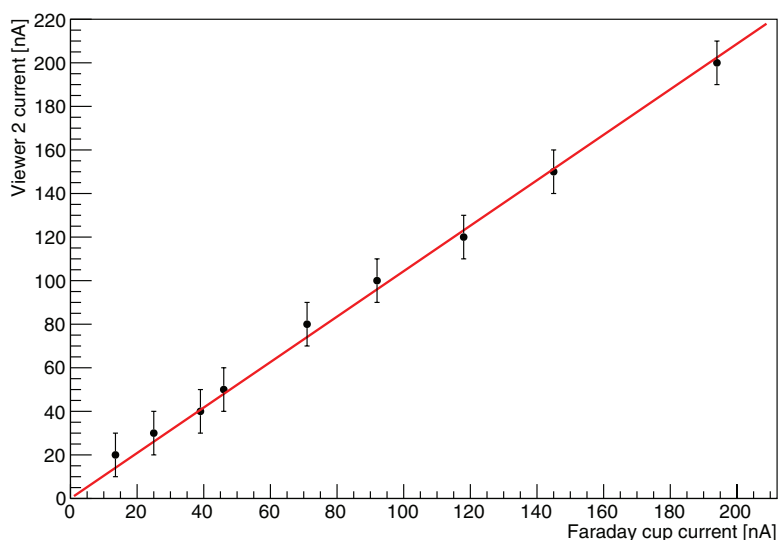


**Figure 4.** Beam current measured with the integrated read-out device at the second BTL viewer as a function of the current measured by the Faraday cup. The line represents the result of a linear fit.

high-sensitivity Faraday cup [11] was used, as shown in figure 3. To reduce the effects due to secondary electrons to a negligible level, a polarisation potential of 1000V was applied to a guard ring preceding the cup. The dependency of the measured current on the polarisation potential shows that most of the secondary electrons are stopped at 50V. Any voltage above this value guarantees operation in the plateau region. To avoid ground loops, the cup on which the protons impinged was not connected with the ground potential of the accelerator and was left floating. The diameter of the cup is 40 mm. The produced signals were sent to a digital electrometer (Keithley model 616) with a sensitivity of about 1 pA. The values of the current obtained using both the second viewer and the Faraday cup were compared for currents above 10 nA. A good agreement between the two measurements was found, as reported in figure 4. The current measured with the read-out device at the second BTL viewer was found to be a linear function of

the current measured with the Faraday cup. The function was fitted to the data with the slope  $a = 1.04 \pm 0.03$ . The settings of the quadrupoles were optimised to eliminate beam losses between the second viewer and the cup.

#### 4. Experimental results

In order to obtain currents as low as a few  $\mu\text{A}$ , the arc current of the ion source can be reduced without changing any other parameter with respect to the set-up used for routine radioisotope production with intensities of about  $70 \mu\text{A}$  in single beam mode. In general, the arc current needed to have a given current on target depends on the performance of the ion source. For radioisotope production, the ion source is set to 300–600 mA for currents on target in the range 70–150  $\mu\text{A}$ . To obtain stable beam conditions at low currents, the plasma inside the source has to be stable. For this reason, the

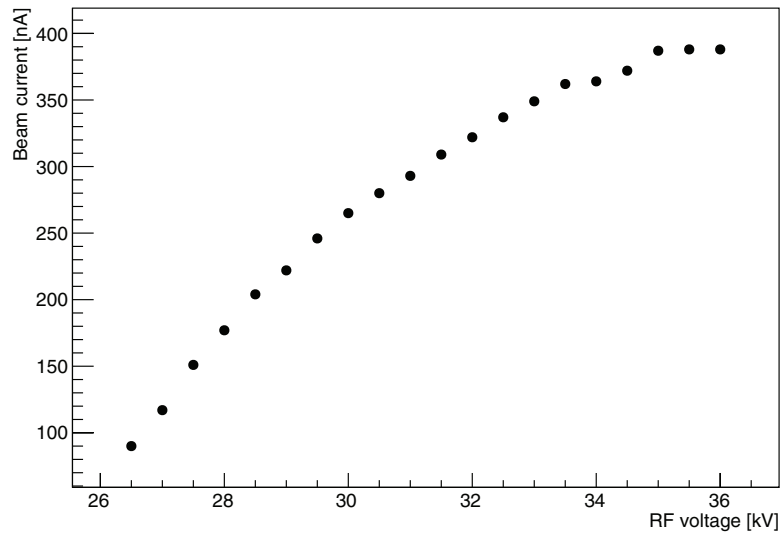


**Figure 5.** Beam current measured by the Faraday cup as a function of the RF peak voltage. The error bars are not visible due to the small uncertainties.

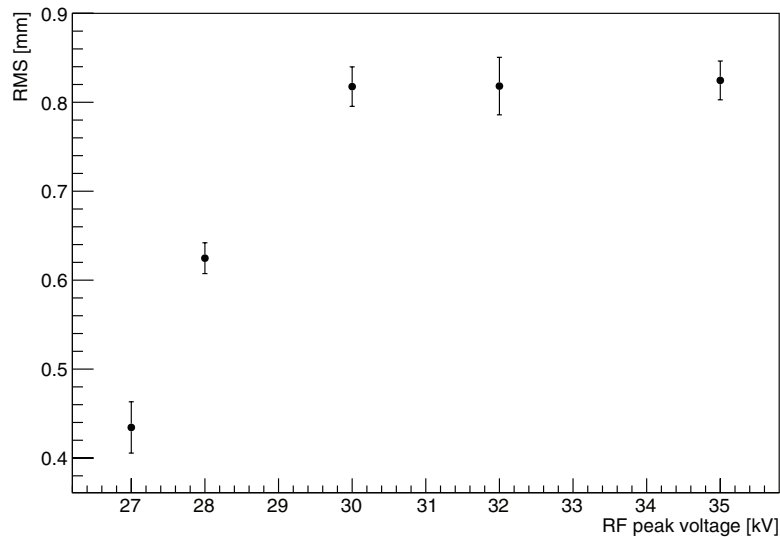


**Figure 6.** The RMS of the horizontal beam distribution measured as a function of the RF peak voltage.

minimum possible arc current is set to 1 mA, producing about  $0.5 \mu\text{A}$  on target. This minimum setting of the arc current of the ion source was kept constant for all the measurements described in this paper. For the quadrupole doublets and the XY steering magnet of the BTL, the standard configuration optimised for the irradiation of solid targets was used. It guarantees a transmission efficiency higher than 95% from the stripper to the Faraday cup [4].

The accelerating peak voltage provided by the 42 MHz RF system can range from 26.5 to 36 kV. A decrease in the current on target is expected when the RF peak voltage is decreased [12]. This effect is mostly due to the fact that the puller is able to extract more  $\text{H}^-$  ions from the chimney of the ion source for larger values of the electric field acting on the periphery of the plasma. To study this effect in detail, the beam current was measured as a function of the RF peak voltage. The results are reported in figure 5. A smooth decrease of more than a factor of four was observed when passing from 36 kV to 26.5 kV. For these measurements, the current of the main coil was set

to 137.05 A, which corresponded to the optimal isochronism and, consequently, to the maximum extracted current. The decrease in the intensity may also have been due to a change of the initial beam Twiss parameters from the ion source to the injection to the cyclotron. This would lead to transverse mismatching with consequent beam losses. To examine this effect, the RMS of the beam distribution in the horizontal plane was evaluated as a function of the RF peak voltage by means of a beam profile detector [5], as reported in figure 6. This detector was located at the end of the BTL, just in front of the Faraday cup. At values of the RF peak voltage below 30 kV, a decrease in the beam size was observed. A maximum decrease in the beam width was measured to be about 50% at the lowest voltage of 27 kV.

To further decrease the extracted current, it is possible to operate the cyclotron with a magnetic field which does not correspond to the optimal isochronism. Therefore, the beam current at the end of the BTL was studied as a function of the current in the main coil ( $I_{MC}$ ). Several consecutive sets

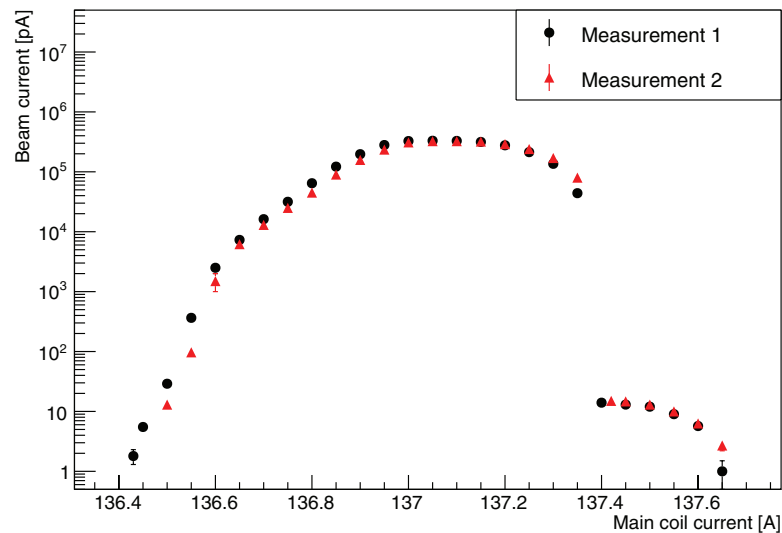


**Figure 7.** Beam current measured by the Faraday cup as a function of the current in the mail coil of the cyclotron. The circles and the triangles correspond to two different sets of measurements.

of measurements were performed and good agreement was found thus demonstrating the reproducibility of the obtained values. Two series of collected data are shown in figure 7, where the circles and triangles correspond to measurements performed by increasing and decreasing the current in the main coil, respectively. A smooth increase in the beam current was observed when going from low values of  $I_{MC}$  towards the isochronism condition. In this region, stable currents of a few pA were obtained. The slope of the curve is such that small variations of  $I_{MC}$  do not have a large influence on the current on target. After the isochronism condition, the extracted current decreases and shows a kink at about  $I_{MC} = 137.4$  A. Here the beam is unstable. This effect may be due to the interception of the beam by the body of the second ion source or to a resonant condition producing beam losses. Due to the presence of a discontinuity, the part of the curve above the optimal isochronism is therefore less suitable for stable low current operation.

With the goal of obtaining the lowest current, the value of  $(1.5 \pm 0.5)$  pA was reached. The uncertainty includes the precision of the electrometer and effects due to beam instabilities. This is at the limit of the sensitivity of the electrometer used for our measurements. The mean current read by the device while the system is operational but the beam is interrupted before the Faraday cup is of  $(-2.0 \pm 0.5)$  pA. This negative current value can be explained by the slight induction caused by the stoppage of the beam just in front of the Faraday cup. This clearly shows that our lowest measured current is not part of the system's baseline noise. The stability of the beam current was observed for a period of about ten minutes within the uncertainty.

## 5. Conclusions

The study presented in this paper demonstrates for the first time the possibility of using a medical cyclotron to produce stable currents from a few pA to a few nA only by acting on the ion source, radio-frequency and main coil tuning. With this method, stable beam currents down to  $(1.5 \pm 0.5)$  pA

were obtained. This represents a reduction of seven orders of magnitude with respect to the design range of beam currents needed for radioisotope production. The obtained results open the way for several multidisciplinary scientific activities usually not performed with this kind of accelerators such as, for example, radiation biophysics.

## References

- [1] Braccini S et al 2011 The new Bern cyclotron laboratory for radioisotope production and research *Proc. of IPAC 2011 (San Sebastian, Spain)* p 3618
- [2] Braccini S 2013 Particle accelerators and detectors for medical diagnostics and therapy *Habilitationsschrift* Universität Bern
- [3] Braccini S 2013 The new Bern PET cyclotron, its research beam line, and the development of an innovative beam monitor detector *AIP Conf. Proc.* **1525** 144–50
- [4] Ghithan S et al 2015 Development of a PET cyclotron based irradiation setup for proton radiobiology *J. Instrum.* **10** P02010
- [5] Braccini S et al 2012 A beam monitor detector based on doped silica and optical fibres *J. Instrum.* **7** T02001
- [6] Häberli M 2014 Beam diagnostics and characterization of a medical cyclotron transport line *Master Thesis* Universität Bern
- [7] Kirillova E 2014 Study and test of a beam monitor detector for the Bern medical cyclotron *Master Thesis* Universität Bern
- [8] Braccini S et al 2015 Study of the radioactivity induced in air by a 15 MeV proton beam *Radiat. Prot. Dosim.* **163** 269–75
- [9] IAEA 2008 *Cyclotron Produced Radionuclides: Principles, Practice (IAEA Technical Report vol 465)* (Vienna: International Atomic Energy Agency)
- [10] IAEA 2009 *Cyclotron Produced Radionuclides: Physical Characteristics, Production Methods (IAEA Technical Report vol 468)* (Vienna: International Atomic Energy Agency)
- [11] Raich U 2006 Beam diagnostics *CERN Accelerator School, Small Accelerator (CERN vol 06–12)* ed D Brandt (Geneva: CERN) p 297
- [12] Kleeven W 2006 Injection and extraction for cyclotrons *CERN Accelerator School, Small Accelerator (CERN vol 06–12)* ed D Brandt (Geneva: CERN) p 271

## A detector based on silica fibers for ion beam monitoring in a wide current range

M. Auger,<sup>a</sup> S. Braccini,<sup>a,1</sup> T.S. Carzaniga,<sup>a</sup> A. Ereditato,<sup>a</sup> K.P. Nesteruk<sup>a</sup> and P. Scamporrà<sup>a,b</sup>

<sup>a</sup>Albert Einstein Center for Fundamental Physics (AEC),  
Laboratory for High Energy Physics (LHEP), University of Bern,  
Sidlerstrasse 5, CH-3012 Bern, Switzerland

<sup>b</sup>Department of Physics “E. Pancini”, University of Napoli Federico II,  
Complesso Universitario di Monte S. Angelo, I-80126, Napoli, Italy

E-mail: [saverio.braccini@lhep.unibe.ch](mailto:saverio.braccini@lhep.unibe.ch)

**ABSTRACT:** A detector based on doped silica and optical fibers was developed to monitor the profile of particle accelerator beams of intensity ranging from 1 pA to tens of  $\mu\text{A}$ . Scintillation light produced in a fiber moving across the beam is measured, giving information on its position, shape and intensity. The detector was tested with a continuous proton beam at the 18 MeV Bern medical cyclotron used for radioisotope production and multi-disciplinary research. For currents from 1 pA to 20  $\mu\text{A}$ ,  $\text{Ce}^{3+}$  and  $\text{Sb}^{3+}$  doped silica fibers were used as sensors. Read-out systems based on photodiodes, photomultipliers and solid state photomultipliers were employed. Profiles down to the pA range were measured with this method for the first time. For currents ranging from 1 pA to 3  $\mu\text{A}$ , the integral of the profile was found to be linear with respect to the beam current, which can be measured by this detector with an accuracy of  $\sim 1\%$ . The profile was determined with a spatial resolution of 0.25 mm. For currents ranging from 5  $\mu\text{A}$  to 20  $\mu\text{A}$ , thermal effects affect light yield and transmission, causing distortions of the profile and limitations in monitoring capabilities. For currents higher than  $\sim 1 \mu\text{A}$ , non-doped optical fibers for both producing and transporting scintillation light were also successfully employed.

**KEYWORDS:** Beam-line instrumentation (beam position and profile monitors; beam-intensity monitors; bunch length monitors); Instrumentation for particle accelerators and storage rings - low energy (linear accelerators, cyclotrons, electrostatic accelerators); Instrumentation for particle-beam therapy

<sup>1</sup>Corresponding author.

---

## Contents

<b>1</b>	<b>Introduction</b>	<b>1</b>
<b>2</b>	<b>Materials and methods</b>	<b>2</b>
<b>3</b>	<b>Measurements and results</b>	<b>3</b>
<b>4</b>	<b>Conclusions and outlook</b>	<b>8</b>

---

## 1 Introduction

Beam monitoring is essential for commissioning and operating any kind of particle accelerator. The knowledge of the transverse beam profile is very often crucial. For instance, knowing the position and the profile of a particle beam is required in medical applications encompassing hadrontherapy and production of radioisotopes for diagnostics and therapy. Depending on the specific use of the accelerator, different current ranges and locations for beam monitoring devices have to be considered. In particular, proton or carbon ion beams with currents of the order of 1 nA or less are used in hadrontherapy. The precise and continuous control of the position, intensity and shape of such beams is needed during acceleration, transport and extraction to deliver the prescribed dose to the patient. For the production of radioisotopes, proton beams of high intensity, in the range 10–500  $\mu\text{A}$ , are used and the control of target bombardment provides an efficient, safe and reliable production. Some research activities, such as radiobiology, particle detector or materials science developments, require low intensity beams, down to the pA range. Beam profilers are also fundamental tools for beam dynamics studies, as the measurement of the transverse beam emittance, a key parameter to optimize beam transport according to specific needs. A multi-purpose detector suitable for both low (pA) and high ( $\mu\text{A}$ ) currents would represent an optimal solution to monitor beams in different irradiation conditions. Furthermore, a beam monitor detector should be easy to operate and compact in order to minimize the required space along the beam path.

A beam monitor detector based on doped silica and optical fibers has been conceived and designed at the AEC-LHEP in Bern. The first proof-of-concept prototype was tested with a 2 MeV pulsed beam at an average intensity of 0.8  $\mu\text{A}$  [1]. This beam profiler, named Universal Beam Monitor (UniBEaM), fulfills the requirements of a simple, robust and compact device to be installed along beam transport lines or other critical locations and is suitable to monitor both pulsed and continuous beams. In this paper, we report on further original developments of the UniBEaM detector aimed at exploiting its potential in a wide intensity range from 1 pA to tens of  $\mu\text{A}$ . The results of the tests performed for the first time with a continuous beam extracted from the 18 MeV Bern medical cyclotron are presented.

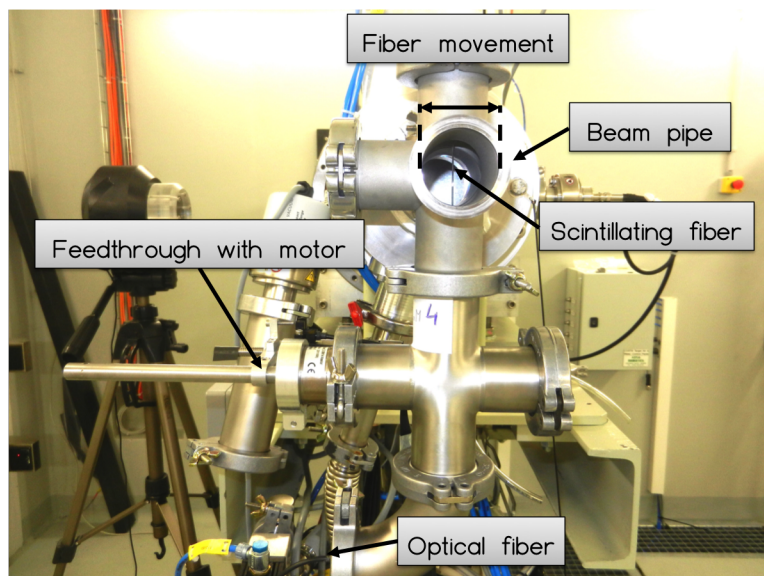


**Figure 1.** The UniBEaM detector installed on the beam transport line (BTL) at the Bern cyclotron laboratory. The main components and the movement of the fiber are highlighted.

## 2 Materials and methods

The UniBEaM detector is based on a single doped silica fiber moving transversally across the beam and is shown in figure 1. Charged particles passing through the fiber cause scintillation and yielded light is transported to a photon detector, whose electric signal is then digitized. For a KF-40 beam pipe, an 8 cm long scintillating fiber is coupled to a commercial optical fiber to transfer the optical signal over more than 20 meters with negligible losses. The sensing fiber has a diameter in the range of 200–400  $\mu\text{m}$ , while the diameter of the core of the optical fiber is 400  $\mu\text{m}$ . The coupling between the sensing and the optical fiber is realized by means of two cylindrical aluminum connectors to which the fibers are glued. The one with the scintillating fiber is screwed to the second one, which holds the optical fiber. This solution provides an optimal centering of the connection between the two polished surfaces of the fibers, thus minimizing light losses. Furthermore, the sensing fiber can be easily replaced. To guarantee a good transmission of the signal, optical grease is used for the connection. The fiber is moved by a vacuum tight linear motion feedthrough (Pfeiffer Vacuum DS040A) attached to a spindle drive and a brushless motor (Faulhaber 2232 S 024 BX4 CSD). The motor communication port and data acquisition module are integrated in a Raspberry Pi 2 board and controlled by a dedicated software. A standard beam scan consists of a series of 250  $\mu\text{m}$  motor steps. The step, range and speed of the motion are adjustable. Each step is followed by the measurement of light intensity. The digitized signal from a photodiode or a photomultiplier is plotted online as a function of the position and stored. The fiber being the only sensing device, space along the beam path can be minimized, and several detectors can be put in sequence, as in the case of  $x - y$  profile measurements. The interference between the fiber and the beam is minimal and profiles are measured in a non-destructive way and without affecting the operation of the accelerator. Furthermore, all the devices sensitive to radiation damage are located outside the bunker, allowing the use of this detector in presence of intense radiation fields.

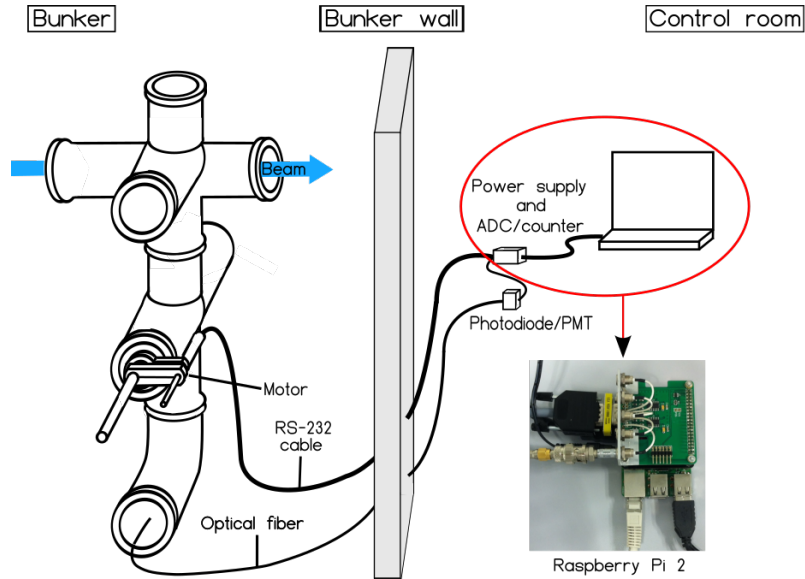


**Figure 2.** Typical experimental set-up of the UniBEaM detector. All the electronic devices are located in the control room.

Scintillation also occurs in non-doped silica fibers due to the presence of impurities. The feasibility of using an optical fiber for both producing and transmitting scintillation light was studied. This solution leads to a further simplification by avoiding the doped-optical fiber coupling.

Monitoring beams below 1 nA is challenging due to the limited yield of scintillation light. To achieve sensitivity to currents down to the pA range, a specific read-out system was designed. It consists of an ultra low noise single-photon counter (IDQ ID100-MMF100ULN), a NIM discriminator (LeCroy 623B), and a 100 MHz counting rate CAMAC scaler (LeCroy 2551). The single-photon counter is crucial for this operation mode. It is based on a solid state photomultiplier and allows to obtain a time resolution of 40 ps with a maximum counting rate of 20 MHz and a dark count rate of 20 Hz. With this system, the number of counts is recorded at each step of the motor for a duration of the order of 100 ms.

Beam tests with a continuous proton beam were performed at the cyclotron laboratory in operation at the Bern University Hospital (Inselspital), where a medical PET cyclotron is equipped with an external beam transport line (BTL). A detailed description of the Bern cyclotron laboratory can be found in [2]. In order to obtain low current beams, the accelerator was operated according to the procedure described in [3]. The experimental set-up is reported in figures 2 and 3. A Faraday cup for measuring the current is installed after the UniBEaM detector at the end of the BTL.

### 3 Measurements and results

For the measurements in the pA range,  $Ce^{3+}$  doped silica fibers were used due to their good scintillation properties [1, 4] and large light yield. The sensing fiber was moved through the beam and photon counting was performed at each position for 100 ms with the read-out system described above. Beam profiles for beam currents of 1 pA and 50 pA are reported in figure 4. The signal due to the beam is clearly visible with a signal-to-noise ratio of 10 and 320, at 1 pA and 50 pA,

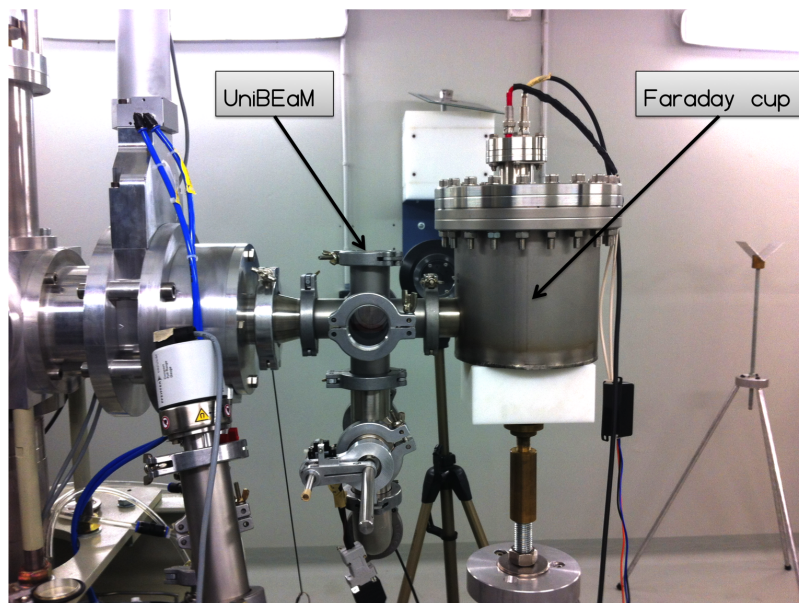


**Figure 3.** The UniBEaM detector and the Faraday cup installed on the BTL at the Bern cyclotron laboratory.

respectively. The profiles were measured with a spatial resolution of 0.25 mm, corresponding to one step of the motor.

The beam profile — the beam width in particular — can be precisely evaluated provided that the fiber response is linear with respect to the local beam intensity. To study this issue, beam profiles were collected for different currents in the pA range and the corresponding integrals calculated. The beam current was measured by the Faraday cup connected to a high-precision electrometer (Keysight B2985A). A good linearity of the response was found, as shown in figure 5. This allows to use the UniBEaM detector to measure the beam current with an accuracy of  $\sim 1\%$ . The system used for these measurements was developed for the pA range and saturates for currents exceeding about 100 nA.

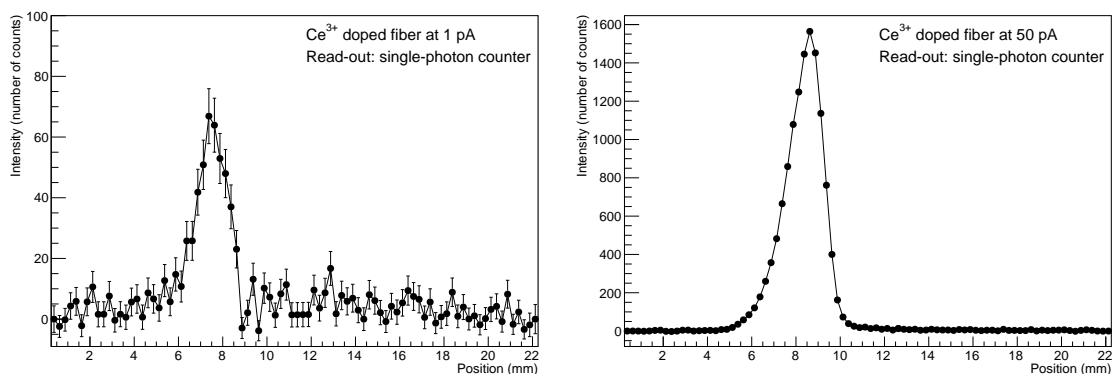


**Figure 4.** Profiles of a 1 pA beam (left) and a 50 pA beam (right).

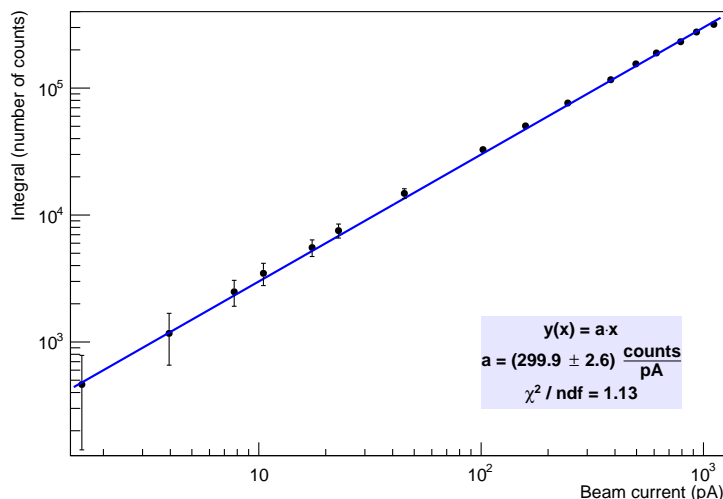


**Figure 5.** Integral of the beam profile as a function of beam current in the pA range. The parameters of the linear fit are reported in the inset.

Beam profile measurements in the nA range were performed with both  $\text{Sb}^{3+}$  [1, 5] and  $\text{Ce}^{3+}$  [1, 4] doped fibers. Two different read-out devices were used: a photodetector based on a silicon photodiode (Thorlabs SV2-FC) and a photomultiplier tube (PMT — Hamamatsu H8443). These two systems are less sophisticated and less expensive than that used for the pA range. The wavelength spectrum of  $\text{Sb}^{3+}$  doped fibers presents two peaks at 695 nm and 755 nm, thus matching the responsivity of both detectors. The photodiode provides sufficient gain to measure beam profiles for currents exceeding 20 nA, while a PMT is used at lower currents. Since the wavelength spectrum of  $\text{Ce}^{3+}$  doped fibers peaks at 490 nm, the responsivity of the silicon photodiode (0.25 A/W at 490 nm) is too low to measure scintillation light. Therefore, only the photomultiplier tube is used with  $\text{Ce}^{3+}$  doped fibers. As examples, beam profiles obtained at 5 nA with a  $\text{Ce}^{3+}$  doped fiber and at 100 nA with an  $\text{Sb}^{3+}$  doped fiber are presented in figure 6. The signal due to the beam is clearly visible with a signal-to-noise ratio of 100 and 170 at 5 nA and 100 nA, respectively. Also with this system, a good linearity of the response was found for currents up to  $3 \mu\text{A}$ , as reported in figure 7.

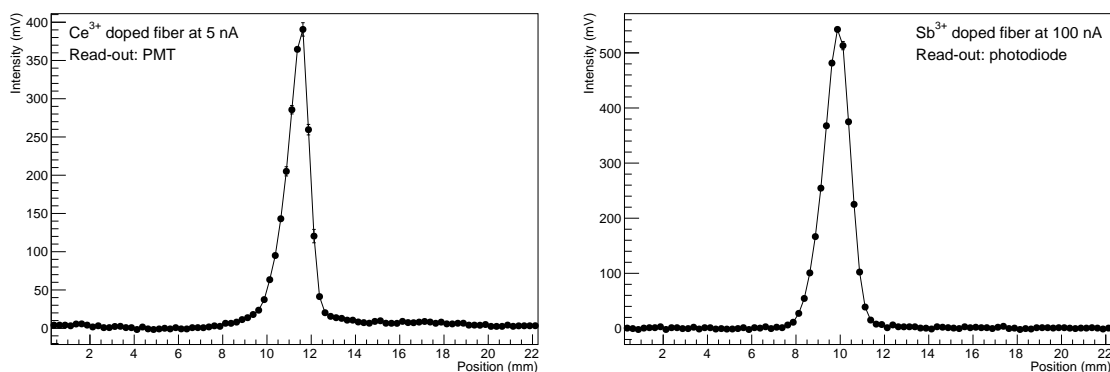


**Figure 6.** Profiles of a 5 nA beam (left) and a 100 nA beam (right) measured with  $\text{Ce}^{3+}$  and  $\text{Sb}^{3+}$  doped silica fibers.

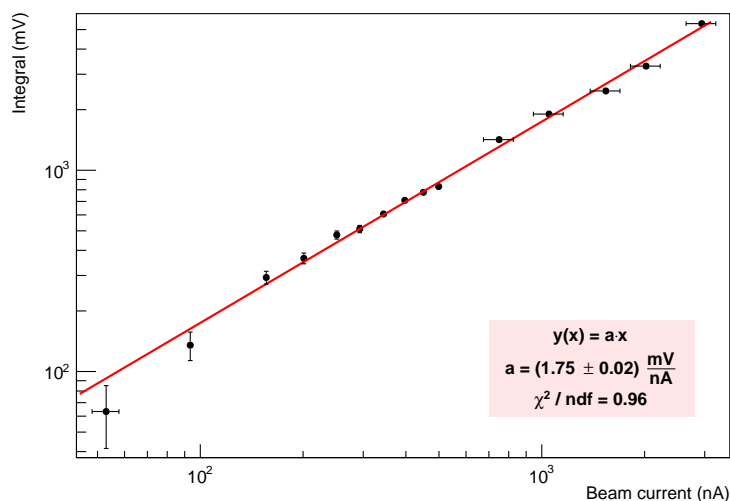


**Figure 7.** Integral of the beam profile as a function of beam current in the nA and  $\mu\text{A}$  range for an  $\text{Sb}^{3+}$  doped fiber. The parameters of the linear fit are reported in the inset.

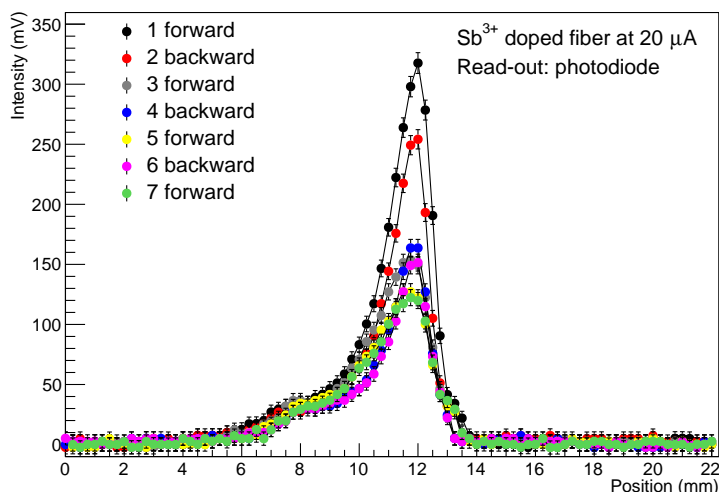


**Figure 8.** Seven consecutive acquisitions of the beam profile at a current intensity of  $20 \mu\text{A}$ .

In this range, the UniBEaM detector can be used to measure the beam current with an accuracy of  $\sim 1\%$ . The position of the maximum and the beam width are determined with a precision of  $0.25 \text{ mm}$ , corresponding to one motor step. Equivalent results were found for both  $\text{Sb}^{3+}$  and  $\text{Ce}^{3+}$  doped fibers.

The linear response of the sensing fiber was lost for currents exceeding a few  $\mu\text{A}$  due to thermal effects. Changes in the emission and transmission properties of the fiber lead to distortions of the beam profile, thus limiting the performance of UniBEaM. However, these effects can be reduced by decreasing the time to pass through the beam. The maximum power delivered to the fiber is reached when it passes through the center of the beam. For the measurements reported in this paper, the maximum power per beam current was estimated to be about  $0.05 \text{ W}/\mu\text{A}$  for beams of about  $5 \text{ mm}$  diameter. Distortion effects on the signal are clearly visible in figure 8, where seven

successive profiles measured at a beam current of  $20\ \mu\text{A}$  using an  $\text{Sb}^{3+}$  sensing fiber are reported. The time of one beam scan is about 3 seconds. These data are in agreement with our previous measurements on the decrease of the light output due to temperature [1]. The maximum of the signal is found to decrease significantly during the first three scans. The signal decrease is less pronounced for the following scans due to the stabilization of the conditions of the fiber. The scintillating properties of the sensing fiber can be recovered by keeping the fiber outside the beam for about five minutes. These effects produce distortions of the profile and an accurate estimate of the beam width is compromised.

However, in some applications, such as radioisotope production, the knowledge of the beam position and an approximate estimation of the beam size are enough to optimize the irradiation. Furthermore, asymmetries of the beam profile can be measured. As an example, the left-sided tail of the profile due to stripping extraction in the cyclotron is visible in figure 8. In fact, not all of the  $\text{H}^-$  ions reach the stripper at the same turn, which results in a slightly higher energy for the protons stripped at larger radii and a slightly different exit angle. Different bending occurs in the quadrupoles of the BTL for off-axis proton beams and, for some settings as in the case of figure 8, the distributions due to particles with different energies do not overlap, giving the tail in the profile.

For currents in the  $\mu\text{A}$  range, the UniBEaM based on a non-doped optical fiber, as described in section 2, was tested for the first time. The minimum observable current is found to be about  $1\ \mu\text{A}$  when a photodiode is used as a read-out device. However, this minimum current depends on the particular kind of fiber, since the amount of impurities causing scintillation is not known. For instance, differences were found for the same type of commercial fibers coming from different production batches. A profile measured at a beam intensity of  $1\ \mu\text{A}$  is shown in figure 9. Also in this case, the tail due to stripping extraction in the cyclotron is clearly visible. As discussed above, the linearity with respect to the beam current does not hold in this current range. However, this simpler solution is proven to be suitable to monitor beams in the  $\mu\text{A}$  range with the same limitations as in the case of doped silica fibers.

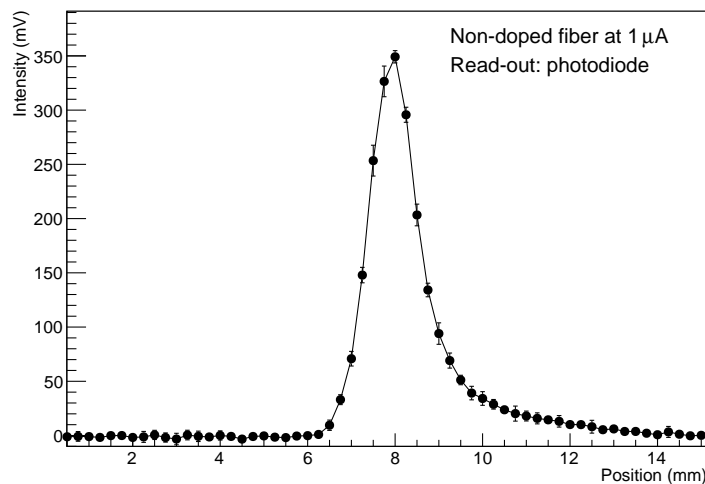


**Figure 9.** Beam profile recorded at  $1\ \mu\text{A}$  with a non-doped silica fiber.

## 4 Conclusions and outlook

The UniBEaM detector was developed as a compact and wide intensity range ion beam monitoring system. It was tested for the first time with a continuous proton beam at the Bern medical PET cyclotron. Beam profiles were measured for currents from 1 pA to 20  $\mu$ A. Profiles down to the pA range were measured with this method for the first time. Fiber response is found to be linear with respect to beam intensity in the range from 1 pA to 3  $\mu$ A, allowing for profile and intensity measurements. At higher currents, the linearity is lost due to thermal effects. Although the beam profiles are distorted in the 5–20  $\mu$ A range, this system still provides information on beam position and width, useful for specific applications such as the production of medical radioisotopes. For currents in the  $\mu$ A range, a non-doped silica fiber was successfully used as a sensor.

Further developments and optimizations are on-going. The UniBEaM detector is employed in several research activities at the Bern cyclotron laboratory, as the assessment of radiation hardness of electronic components or the study of the transverse beam emittance [6]. Read-out systems based on single-photon counting and optical attenuators for currents exceeding 100 nA are currently under study. This solution could potentially lead to a read-out device able to cover the full intensity range from pA to tens of  $\mu$ A. Developments aimed at extending the intensity range above 20  $\mu$ A are being pursued. Furthermore, the industrialization of the UniBEaM detector is on-going in collaboration with the Canadian company D-PACE [7].

## Acknowledgments

We acknowledge contributions from LHEP engineering and technical staff. We are indebted to Valerio Romano and Jonas Scheuner from the Institute of Applied Physics (IAP) of the University of Bern and to Anna Vedda and Norberto Chiodini of the University of Milano-Bicocca for the useful discussions and for providing us with some fibers. We thank ID Quantique SA (Switzerland) and D-PACE Inc. (Canada) for their collaboration.

## References

- [1] S. Braccini et al., *A beam monitor detector based on doped silica and optical fibres*, [2012 JINST 7 T02001](#).
- [2] S. Braccini et al., *The new Bern cyclotron laboratory for radioisotope production and research*, in *Proceedings of IPAC2011*, San Sebastian Spain (2011), THPS080, pg. 3618, <http://jacow.org>; S. Braccini, *The new Bern PET cyclotron, its research beam line, and the development of an innovative beam monitor detector*, *AIP Conf. Proc.* **1525** (2013) 144.
- [3] M. Auger et al., *Low current performance of the Bern medical cyclotron down to the pA range*, *Meas. Sci. Technol.* **26** (2015) 094006.
- [4] N. Chiodini et al., *Ce-doped SiO<sub>2</sub> optical fibers for remote radiation sensing and measurement*, *Proc. SPIE* **7316** (2009) 731616.
- [5] M. Neff et al., *Broadband fluorescence of Sb<sup>3+</sup>-doped silica fibres*, *Opt. Mater.* **33** (2010) 1.
- [6] K.P. Nesteruk et al., *Study of the transverse beam emittance of the Bern medical cyclotron*, in *Proceedings of IBIC2015*, Melbourne Australia (2015), MOPB041.
- [7] [www.d-pace.com](http://www.d-pace.com).



# UniBEaM: a Silica Fiber Monitor for charged Particle Beams

M. Auger<sup>1</sup>, S. Braccini<sup>1</sup>, T. S. Carzaniga<sup>1</sup>, N. Chiodini<sup>2</sup>, A. Ereditato<sup>1</sup>,  
K. P. Nesteruk<sup>1,a)</sup>, P. Scamporrì<sup>1,3</sup> and A. Vedda<sup>2</sup>

<sup>1</sup>*Albert Einstein Center for Fundamental Physics (AEC), Laboratory for High Energy Physics (LHEP),  
University of Bern, Switzerland*

<sup>2</sup>*Department of Materials Science, University of Milano-Bicocca, Italy*

<sup>3</sup>*Department of Physics "E. Pancini", University of Napoli Federico II, Italy*

<sup>a)</sup>Corresponding author: konrad.nesteruk@lhep.unibe.ch

**Abstract.** A beam monitoring detection technique based on silica fibers has been developed by AEC-LHEP. The light signal produced in a doped silica fiber crossing the beam is collected to measure the beam profile. Two types of detectors have been constructed and tested. The first one operates in vacuum and was tested at the 18 MeV medical proton cyclotron at the University Hospital in Bern. It is able to measure currents from a few pA to 20  $\mu$ A. It can be employed to optimize the production of radioisotopes, in particular using solid targets. The second one operates in air and was tested with high-energy pion and proton beams at the CERF facility at CERN. This paper reports on both detectors with focus on the most recent results obtained with the second detector.

## INTRODUCTION

Beam monitoring is essential for operating any kind of particle accelerator. It is crucial in medical applications encompassing hadrontherapy and production of radioisotopes for diagnostics and therapy. In particular, precise knowledge of the beam shape and position is required for the irradiation of solid targets. The same applies for the monitoring of GeV accelerated particles. To match the needs of different applications, a multi-purpose detector suitable for both low (down to  $\approx 1$  pA) and high (up to tens of  $\mu$ A) beam currents would represent an optimal solution. Furthermore, a beam monitor detector should be easy to operate, fitting installation in critical positions of accelerators and beam transport lines, and compact in order to minimize the required space along the beam path. In this context, a detector based on doped silica and optical fibers was developed at AEC-LHEP in Bern to monitor the profile of ion beams of intensity ranging from 1 pA to 20  $\mu$ A [1] produced by medical cyclotrons. It allows monitoring ion beams by measuring the light yield due to charged particles impinging on a scintillating fiber moved through the beam. The detector, named Universal BEam Monitor (UniBEaM), fulfills the requirements of a simple, compact and versatile device for both pulsed and continuous beams. This beam profiler is already employed for particle accelerator studies as beam emittance measurements [2] and for multi-disciplinary research. Its use with solid targets is currently under study. For measurements in air, a detector based on the same principle was recently developed and tested with a proton and pion beam accelerated by the Super Proton Synchrotron (SPS) at CERN in Geneva. This paper summarizes the results obtained with the Bern medical cyclotron and reports on the first preliminary measurements obtained with high-energy beams extracted in air.

## MATERIALS AND METHODS

The UniBEaM detector is based on a single scintillating fiber moving across the beam. Charged particles passing through the fiber cause scintillation and yielded light reaches a photon detector, whose electric signal is digitized. The fiber is moved by means of a remotely controlled motor. The 10 cm short scintillating sensing fiber is coupled to a

WTT16

AIP Conf. Proc. 1845, 020015-1–020015-5; doi: 10.1063/1.4983546  
Published by AIP Publishing. 978-0-7354-1517-1/\$30.00

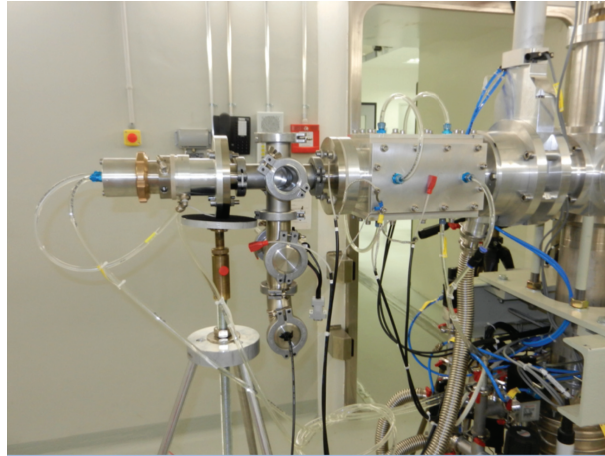


**FIGURE 1.** The UniBEaM detector installed at the end of the beam transfer line of the Bern medical cyclotron. The sensing fiber is under vacuum inside the beam pipe.

commercial optical fiber to transport the optical signal over meters with negligible losses. The motor communication port and data acquisition module are integrated in a Raspberry Pi board and controlled by dedicated software.

Two beam monitoring apparatuses were developed and constructed to be operated in vacuum and in air. The first one (Fig. 1) was tested with the external beam line of the 18 MeV medical cyclotron in Bern [3]. A standard beam scan consists of a series of 0.25 mm motor steps. The step, range and speed of the motion are adjustable. The digitized signals from a photodiode or a photomultiplier are plotted online as a function of the position and stored for offline analysis. The choice of the sensing fiber and read-out device depends on the current intensity range. In the pA range,  $\text{Ce}^{3+}$  [4] [5] doped fibers are used due to their good scintillating properties and large light yield. To achieve the sensitivity needed for these very low intensity currents, an ultra low noise single-photon counter based on a solid-state photomultiplier is used as a read-out. With this system, the number of counts is recorded at each step of the motor for a time interval of the order of 100 ms. In the nA range,  $\text{Ce}^{3+}$  and  $\text{Sb}^{3+}$  [4] [6] doped fibers are typically used with a read-out based on a photomultiplier tube or a silicon photodiode. Due to the wavelength spectrum of  $\text{Ce}^{3+}$  doped fibers (peaked at 490 nm), the responsivity of the silicon photodiode is too low to measure the scintillation light. In the  $\mu\text{A}$  range,  $\text{Sb}^{3+}$  doped fibers are typically used and the read-out system is based on a silicon photodiode. Scintillation also occurs in non-doped optical fibers due to the presence of impurities. This solution was also implemented in the detector operating in vacuum.

The second UniBEaM detector was conceived to be operated in air to detect high-energy beams of extremely low intensity (Fig. 2). For this reason specific high light yield fibres were employed. These fibers feature a 600  $\mu\text{m}$  diameter core and 75  $\mu\text{m}$  fluorinated silica cladding, being 750  $\mu\text{m}$  the fiber overall diameter. The drawn perform was obtained by collapsing a suitable commercial fluorinated silica tube over a  $\text{SiO}_2:500$  ppm Ce cylinder prepared by sol-gel method starting from tetramethoxysilane (TMOS) and  $\text{Ce}(\text{NO}_3)_3$  precursors. The emission spectrum of the fiber consists in the  $5d_1-4f$  allowed radiative transition of  $\text{Ce}^{3+}$  peaking at 450 nm. The scintillating Ce-doped fiber is moved transversely to the beam by means of a servo motor and is mechanically connected to a standard optical fiber that conveys the generated optical signal outside from the measurement bunker and into the control room, where it enters the typical UniBEaM read-out system based on an APD (IDQuantique, Geneve, CH), a counter and a Raspberry Pi computer. This detector was tested at the CERF facility at CERN with the aim of optimizing the position of the primary beam. CERF [7] is an acronym for CERN-EU high energy Reference Field facility. It is conceived to provide reference neutron fields, mostly for radiation protection studies. Neutrons are produced by colliding a mixed proton and pion beam on a metallic target. The energy of the beam is 120 GeV. The beam is extracted for periods of 5 seconds, the so-called spills, according to the duty cycle of the SPS. The number of particles per spill varies between  $10^6$  and  $10^8$ , about one third pions and two thirds protons. The current therefore can range between 32 fA and 3.2 pA. The beam spot diameter is a few centimeters.

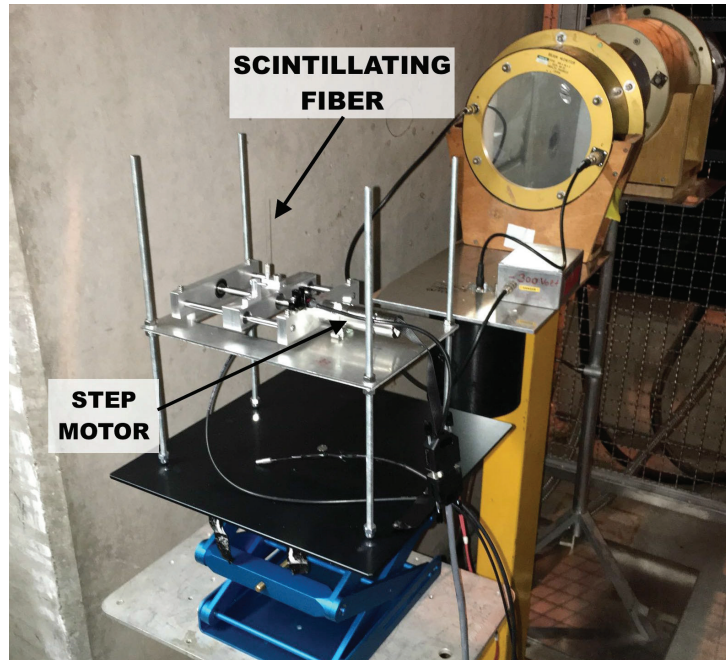


**FIGURE 2.** The UniBEaM detector located in air after the exit window of one of the SPS secondary beam lines at CERN.

## RESULTS

The measurements performed at the Bern medical cyclotron are reported in Ref. [1]. It was proven that the system is sensitive enough to monitor beams down to 1 pA. A good linearity of the response was found in the range 1 pA-1  $\mu$ A with both  $Ce^{3+}$  and  $Sb^{3+}$  doped fibers. Different read-out systems based on a photodiode and on a photomultiplier tube were successfully tested. The feasibility of using an optical fiber for both producing and transmitting scintillation light was also proven. In the nA range, this solution can be adopted with a single-photon counter due to the limited light yield, whereas in the  $\mu$ A range a silicon photodiode can be employed. The use of non-doped fibers brings further simplifications to the system. In particular, the connection between the sensing doped fiber and the optical fiber can be avoided. A good linearity of the fiber response was confirmed also for this solution for the currents up to 300 nA [1]. The linear response of the sensing fiber was lost for currents exceeding a few  $\mu$ A due to thermal effects. Changes in the emission and transmission properties of the fiber lead to distortions of the beam profile, thus limiting the performance of the UniBEaM. However, these effects can be reduced by decreasing the beam crossing time. The maximum power delivered to the fiber per beam current was estimated to be about 0.05 W/mA when the fiber was passing through the center of a beam of 5 mm diameter. These features are important for the use of the UniBEaM detector for radioisotope production, in particular with solid target stations.

The detector operating in air was tested at the CERF facility [7] at CERN (Fig. 2). The first measurements were performed at about 1/3 of the maximum intensity of the extracted beam. The beam profile is shown in Fig. 3. It was obtained by counting the signals over a period of five minutes per position of the fiber. Between two consecutive measurements the fiber was moved by 1 mm. The background was estimated using a fit procedure and subtracted from the data. A second series of measurements was performed to optimize the overall acquisition time and the noise level. The fiber was kept in each position for 2 minutes recoding the number of counts every second. In this way, the time structure of the beam can be monitored. Fig. 4 shows the typical synchrotron spill time pattern. Also in this case, the noise was subtracted by means of a fit procedure.

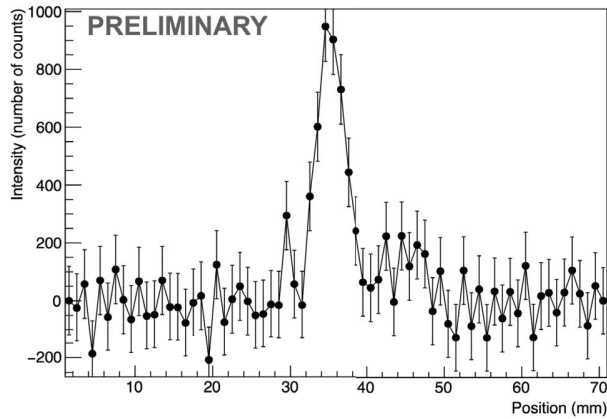


**FIGURE 3.** Beam profile obtained with the UniBEaM detector operating in air with the hadron beam of the CERF facility at CERN.

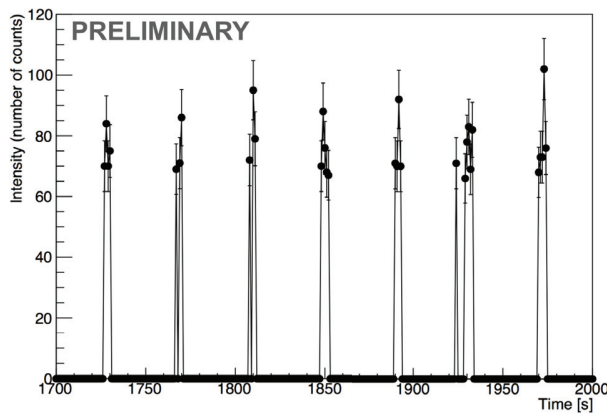


**FIGURE 4.** Intensity of successive spills of the SPS synchrotron at CERN.

## CONCLUSIONS AND OUTLOOK

The UniBEaM detector was conceived as a compact and wide intensity range ion beam monitoring system. Two detectors were designed and built. The first one operates in air and was successfully tested with a continuous 18 MeV proton beam at the Bern medical PET cyclotron in the current range from 1 pA to 20  $\mu$ A. The system is already employed in accelerator physics studies, cross section measurements in view of production of novel PET radioisotopes, and other multi-disciplinary activities. The second detector operates in air and was tested with the 120 GeV proton and pion beam of the CERF facility at CERN. Further developments and optimizations are on-going. In particular, the use of UniBEaM with solid targets and other kind of sensing fibres able to stand higher currents are presently under study. Beam tests with 3-8 MeV deuteron beams are foreseen. The industrialization of the UniBEaM detector is on-going in collaboration with the Canadian company D-PACE [8].

## ACKNOWLEDGMENTS

We acknowledge contributions from LHEP engineering and technical staff. We are indebted to V. Romano and J. Scheuner from the Institute of Applied Physics (IAP) of the University of Bern and M. Silari and N. Dinar from CERN. We thank ID Quantique SA (Switzerland) and D-PACE Inc. (Canada) for their collaboration.

## REFERENCES

- [1] M. Auger et al., “A detector based on silica fibers for ion beam monitoring in a wide current range,” *JINST* **11**, P030027 (2016).
- [2] K. P. Nesteruk et al., “Study of the transverse beam emittance of the bern medical cyclotron,” in *Proceedings of IBIC2015* (2015) pp. 134–8.
- [3] S. Braccini et al., “The new bern cyclotron laboratory for radioisotope production and research,” in *Proceedings of IPAC2011* (2011) pp. 3618–20.
- [4] S. Braccini et al., “A beam monitor detector based on doped silica and optical fibres,” *JINST* **7**, T02001 (2012).
- [5] A. Vedda et al., “Ce<sup>3+</sup> doped optical fibers for remote radiation dosimetry,” *Applied Physics Letters* **85** (2004).
- [6] M. Neff et al., “Broadband fluorescence of sb<sup>3+</sup> doped silica fibers,” *Optical Materials* **33**, 1–3 (2010).
- [7] A. Mitaroff and M. Silari, “The cern-eu high-energy reference field (cerf) facility for dosimetry at commercial flight altitudes and in space,” *Radiation Protection Dosimetry* **102**, 7–22 (2002).
- [8] [www.dpace.com](http://www.dpace.com), Accessed 04.10.2016.





Conference on the Application of Accelerators in Research and Industry, CAARI 2016,  
30 October – 4 November 2016, Ft. Worth, TX, USA

## A Low-Cost Beam Profiler Based On Cerium-Doped Silica Fibers

David Edward Potkins<sup>a\*</sup>, Saverio Braccini<sup>b</sup>, Konrad Pawel Nesteruk<sup>b</sup>, Tommaso Stefano Carzaniga<sup>b</sup>, Anna Vedda<sup>c</sup>, Norberto Chiodini<sup>c</sup>, Jacob Timmermans<sup>a</sup>, Stephane Melanson<sup>a</sup>, Morgan Patrick Dehnel<sup>a</sup>

<sup>a</sup>D-Pace Inc., Suite 305, 625 Front St., Nelson BC V1L4B6, Canada;

<sup>b</sup>Albert Einstein Center for Fundamental Physics, Laboratory for High Energy Physics, University of Bern, Sidlerstrasse 5, Bern, CH-3012, Switzerland; <sup>c</sup>Department of Materials Science, University of Milano-Bicocca, Via Cozzi 55, Milano, 20125, Italy

---

### Abstract

A beam profiler called the Universal Beam Monitor (UniBEaM) has been developed by D-Pace Inc. (Canada) and the Albert Einstein Center for Fundamental Physics, Laboratory for High Energy Physics, University of Bern (Switzerland). The device is based on passing 100 to 600 micron cerium-doped optical fibers through a particle beam. Visible scintillation light from the sensor fibers is transmitted over distances of tens of meters to the light sensors with minimal signal loss and no susceptibility to electromagnetic fields. The probe has an insertion length of only 70mm. The software plots the beam intensity distribution in the horizontal and vertical planes, and calculates the beam location and integrated profile area, which correlates well with total beam current. UniBEaM has a large dynamic range, operating with beam currents of ~pA to mA, and a large range of particle kinetic energies of ~keV to GeV, depending on the absorbed power density. Test data are presented for H<sup>-</sup> beams at 25keV for 500μA, and H<sup>+</sup> beams at 18MeV for 50pA to 10μA. Maximum absorbed power density of the optical fiber before thermal damage is discussed in relation to dE/dx energy deposition as a function of particle type and kinetic energy. UniBEaM is well suited for a wide variety of beamlines including discovery science applications, radio-pharmaceutical production, hadron therapy, industrial ion beam applications including ion implantation, industrial electron beams, and ion source testing.

© 2017 The Authors. Published by Elsevier B.V.

Peer-review under responsibility of the Scientific Committee of the Conference on the Application of Accelerators in Research and Industry.

*Keywords:* Beam-line instrumentation (beam position and profile monitors); Scintillators, Scintillating fiber; Optical wire scanner;

---

\* Corresponding author. Tel.: +1-250-352-5162;  
E-mail address: [dave@d-pace.com](mailto:dave@d-pace.com)

## 1. Introduction

For beamline operators, beam profilers are crucial for verifying beam size and position, as well as the beam intensity distribution shape. Beam profilers allow operators to observe the effects of focusing and steering in real time, and to observe the real-life effects of vacuum quality, space charge and second-order effects causing beam halo. However, the use of beam profilers with industrial accelerator beamlines is often limited or non-existent despite the advantages they provide, often because of budget and space limitations, as noted by Dehnel et al. (2013).

A beam profiler based on doped SiO<sub>2</sub> optical fibers was designed and tested at the Albert Einstein Center for Fundamental Physics (AEC), Laboratory for High Energy Physics (LHEP), University of Bern, Switzerland. This beam profiler, called the Universal Beam Monitor (UniBEaM™), was conceived to meet the requirements for a simple, robust, compact, inexpensive and continuous-monitoring beam profiler. UniBEaM has a large dynamic range, operating with beam currents of ~pA to mA, and a large range of particle kinetic energies of ~keV to GeV, depending on the absorbed power density. Braccini et al. (2012), and Auger et al. (2016) described the use of UniBEaM on their 2MeV and 18MeV proton accelerators. UniBEaM was licensed and commercialized by D-Pace Inc. Canada. This paper describes the commercial UniBEaM design and provides example measurements.

## 2. UniBEaM System Description

UniBEaM is an alternative to conventional wire scanners. Unlike available commercial wire scanners in the same price range, UniBEaM is superior for measuring a wide range of beam currents and particle kinetic energies, and is particularly well suited to measuring low beam currents. The UniBEaM signal is optical rather than electrical, making small signals unsusceptible to interference. UniBEaM also provides control of the speed and position of the fiber, so that the user has flexibility to control integration time for low current beams and to synchronize fiber positioning with pulsed beams. Rotating helical wire scanners do not allow this. Dual orthogonal fibers also occupy less space along the beam axis than rotating helical wire scanners.

Each UniBEaM probe has two sensing fibers; one for X-profiles and one for Y-profiles (see Fig. 1 & Fig. 2). The sensor fibers are moved through the beam by stepper motor actuators. Home switches ensure accurate fiber positioning. There are no electronic components in the probe, making the probe radiation resistant. Two ports in each probe provide access to replace the fibers. Replacement sensor fibers are provided in protective cartridges which also serve as the installation tools. Fiber replacement takes about two minutes following vacuum venting. UniBEaM is an in-line device – it does not require a separate vacuum box or beam-pipe cross. KF and CF flanges options are available. With KF bulkhead clamps, the device has an insertion length of only 70mm.

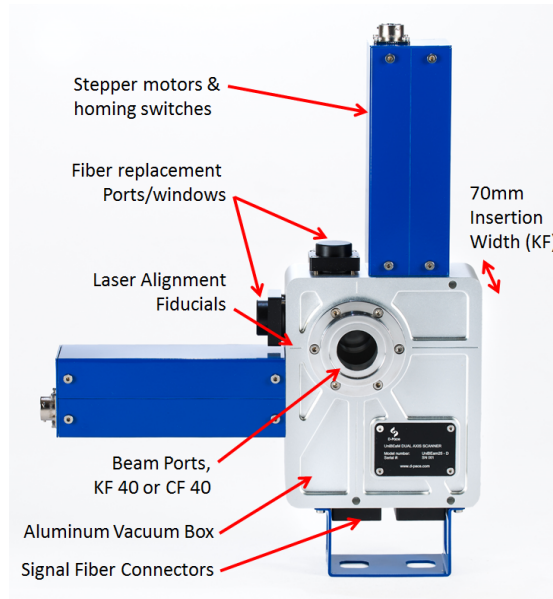


Fig. 1. D-Pace’s commercial UniBEaM dual axis probe

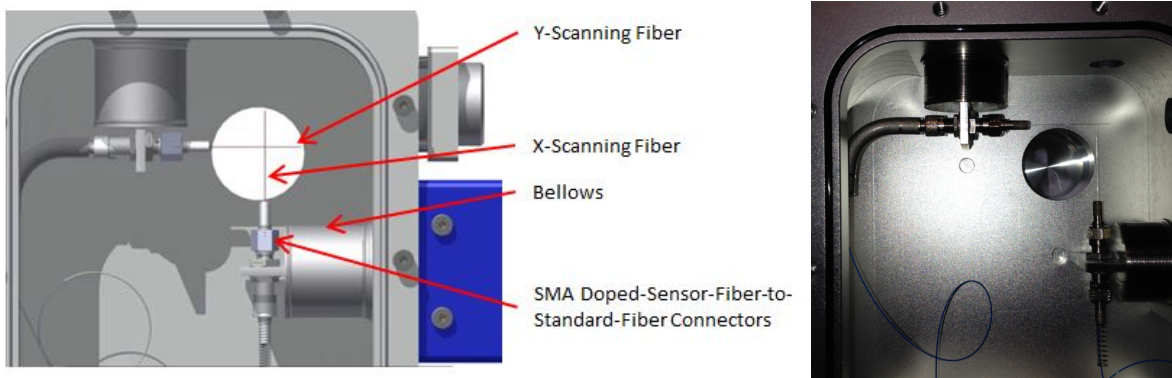


Fig. 2. Internal views of UniBEaM showing the X & Y scintillating sensor fibers and fiber connector

The optical sensing fibers were made by the University of Milano-Bicocca’s Department of Materials Science (UMB-DMS) using the sol-gel process. The fibers are SiO<sub>2</sub> doped with Ce<sup>3+</sup> ions as luminescent activators, and are drawn to a diameter of 200µm. UMB-DMS developed the fiber for dosimetry. The fiber produces intense and fast radio luminescence (RL) emitted by the Ce<sup>3+</sup> dopant ions, with an emission band centered at 450nm, as stated by Vedda et al. (2004), and Mones et al. (2006). The SiO<sub>2</sub> fiber also produces luminescence due to Cherenkov radiation, which is characterized by a broad spectral emission in the blue-UV wavelength region.

The sensor fibers are coupled to 200µm core, hard-clad, 0.5 NA fibers within the probe using SMA in-vacuum connectors. These non-scintillating, in-vacuum fibers pass through vacuum feedthroughs and are terminated on the atmosphere side of the probe with a second pair of optical SMA connectors. Another pair of optical fibers is used to connect the probe to the UniBEaM controller. These fiber-optic patch cables are 400µm, 0.5 NA fibers, which transmit the optical signal, with very low signal loss, to a silicon photo multiplier (SPM) located in the UniBEaM controller. The scintillation light can be transmitted tens or even hundreds of meters with minimal signal loss, and with no susceptibility to electromagnetic fields.

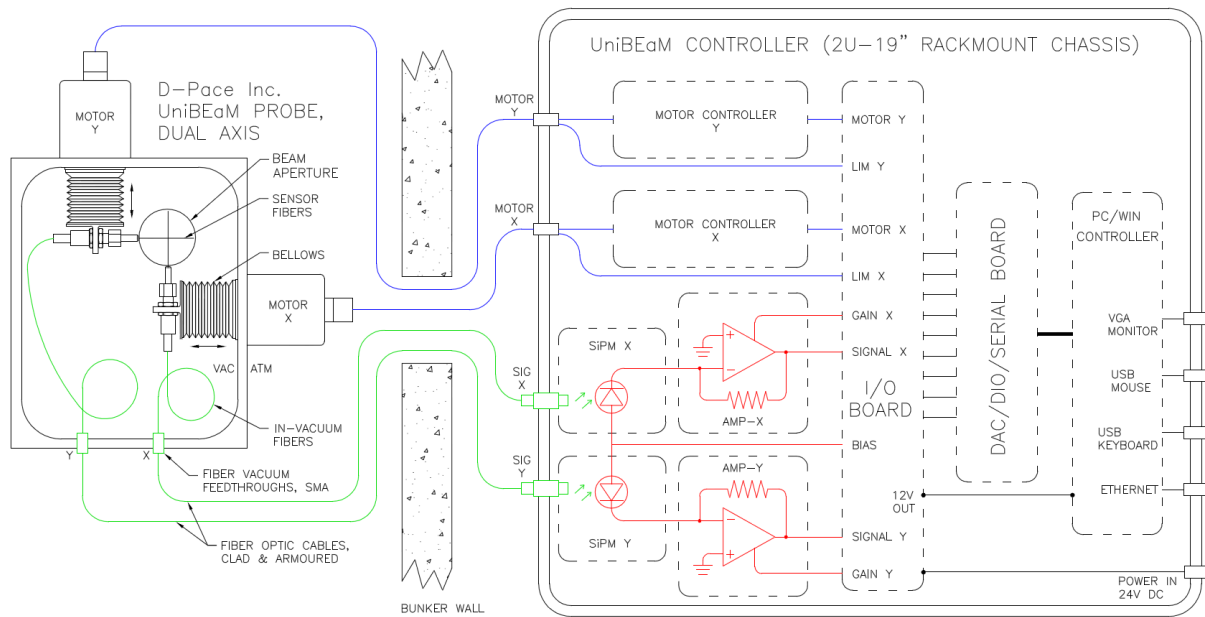


Fig. 3. UniBEaM commercial system architecture

The SPM sensors are very sensitive, fast, compact, and robust solid-state light sensors. The SPM sensor's spectral sensitivity is well matched to the spectral emission of the cerium-doped fiber. The SPMs utilize approximately 5000 sensor channels. Each channel acts as an independent avalanche photo diode, and behaves as a photo-activated switch, but the integrated total current of the large number of SPM channels results in a quasi-analog signal. The SPM bias voltage was optimized to achieve high gain while minimizing dark current to acceptable levels. The SPM active area was chosen based on compromises between sensitivity, resolution, response time and dark current.

Transimpedance amplifiers (2MHz, -3dB) with four orders of magnitude of programmable gain are used to convert the SPM photocurrent to voltage signals suitable for analog-to-digital conversion (ADC) ( $\pm 10V$ , 14bit, 20kS/s). A dedicated amplifier for each axis allows simultaneous X & Y profile scanning. At the fiber speed of 10mm/second, and position increments of 200 $\mu m$ , 5 samples per position increment per channel are averaged. An integrated single-board PC is used for signal processing and the graphical user interface. UniBEaM can be operated as a standalone system with the addition of a mouse and keyboard, or controlled using Ethernet and text-based commands.



Fig. 4.  $Ce^{3+}$  doped  $SiO_2$  fiber (L) and a replacement fiber cartridge (R)

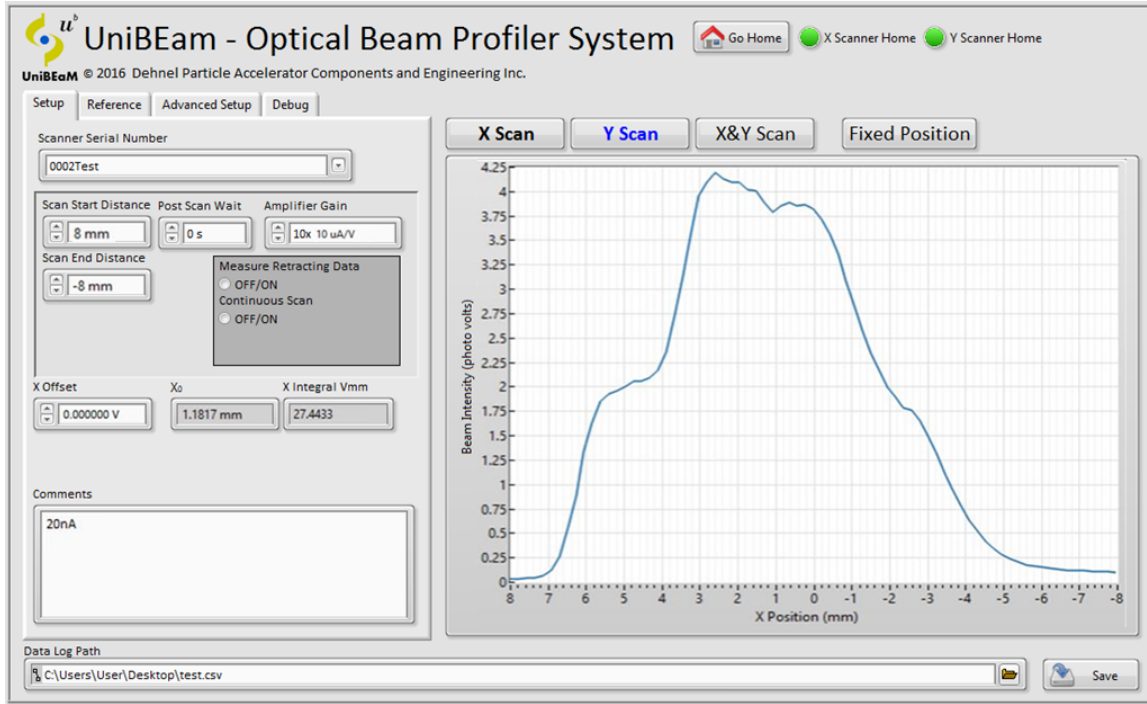


Fig. 5: UniBEaM software user interface, showing intensity profile for an 18MeV 20nA proton beam

The UniBEaM software acquires and analyzes beam profiles (see Fig. 5). The user can change the position step size, and the scan-start and scan-end positions. Single or continuous scans can be acquired. The profile plot of each pass of the fiber can be displayed separately, or overlaid in persistent-display mode to establish time-domain trends. The fiber scanning speed is adjustable. Slower scan speeds enable greater signal averaging for improving the signal-to-noise ratio of low beam current scans. The software calculates the beam centroid and the integral of the intensity profile. The user can set the zero value for the position and integral calculations. Profiles are saved in a CSV-format file with header data.

The UniBEaM software has a second operation mode, which allows the fiber to be moved to a fixed location, and the beam intensity at this position is measured as a function of time, displayed as a strip chart.

### 3. Maximum Absorbed Power Density of Silica Fiber

18MeV proton beams with currents of 20 $\mu$ A and a beam diameter of 5mm caused a temporary reduction of the linear response due to thermal effects on the SiO<sub>2</sub> fibers. For the 20 $\mu$ A beam the responsivity decreased by 25% following a 3 second pass of the fiber through the beam. This is an average beam power density of 18 W $\cdot$ mm<sup>-2</sup>. At 18MeV, the dE/dx for SiO<sub>2</sub> is 5.44 MeV/mm (SRIM software version 2013.00). A 200 $\mu$ m fiber has an average thickness of 0.157 mm, so the energy lost by the protons in the fiber is 0.85MeV, and the average absorbed power density ( $P_D$ ) of the fiber was calculated (equation 1) to be 0.9 W $\cdot$ mm<sup>-2</sup>. We considered this the maximum absorbed power density of the fiber.

$$P_{D(Absorbed)} = \frac{5.44 \frac{MeV}{mm} \cdot 20 \mu A \cdot 0.157 mm}{\frac{\pi}{4} (5.0 mm)^2} = 0.9 W \cdot mm^{-2} \quad (1)$$

A calculation based on radiative heat transfer of an SiO<sub>2</sub> fiber, with an emissivity of  $\epsilon = 0.88$  and a maximum temperature based on its glass transition temperature of  $T_g = 1473K$ , and a 100% view factor to a 300K blackbody,

resulted in a calculated maximum beam power density of  $0.74 \text{ W}\cdot\text{mm}^{-2}$ , which corresponds well with the maximum absorbed power density calculated above (equation 1). These  $P_D$  values for the  $\text{SiO}_2$  compare favorably with the maximum DC power densities reported in the literature by Strehl (1995), (2006), for metal wire scanners (W-Re wire at  $P_D = 0.5 - 1 \text{ W}\cdot\text{mm}^{-2}$ ).

#### 4. Example UniBEaM Intensity Profiles

Auger et al. (2016), measured DC beams from their 18MeV IBA Cyclone cyclotron with their prototype UniBEaM, at currents as low as 1pA. For very low current measurements, they utilized a  $200\mu\text{m}$   $\text{Ce}^{3+}$  doped fiber in conjunction with silicon photon multipliers and a single-photon-counting apparatus to achieve a signal-to-noise ratio (SNR) of 10 at 18MeV 1pA. Beam currents were measured using a Faraday cup (see Fig. 6).

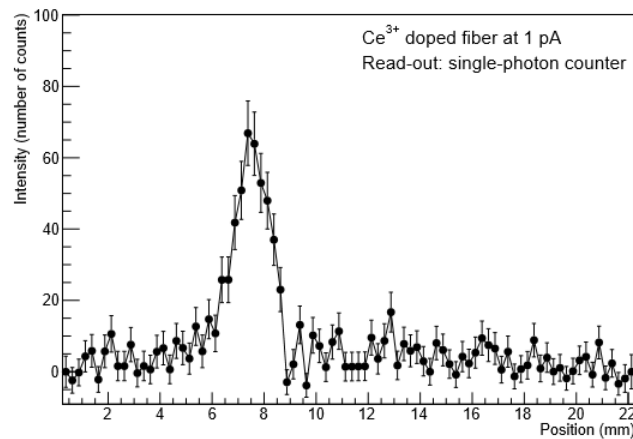
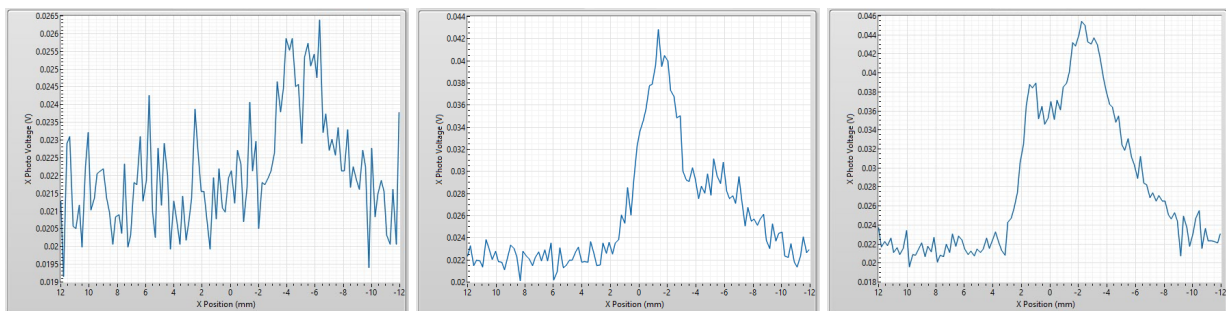


Fig. 6. Profile of an 18MeV 1pA  $\text{H}^+$  beam using photon counting method (courtesy of AEC-LHEP)

D-Pace used the commercial UniBEaM system described above on the same 18MeV cyclotron at  $\text{H}^+$  currents of 12pA, 62pA, 100pA, 225pA, 1nA, and 400nA (see Fig. 7). Integrals of the profiles were plotted (see Fig. 8) versus the beam current measured with the Faraday cup. Even though the beams are not perfectly axisymmetric, there is still good linearity between a Faraday cup current and the beam intensity integral. AEC-LHEP reported similar findings with their prototype UniBEaM System. AEC-LHEP also reported that the linear response of the sensing fiber was lost at currents exceeding a few  $\mu\text{A}$  due to thermal effects.



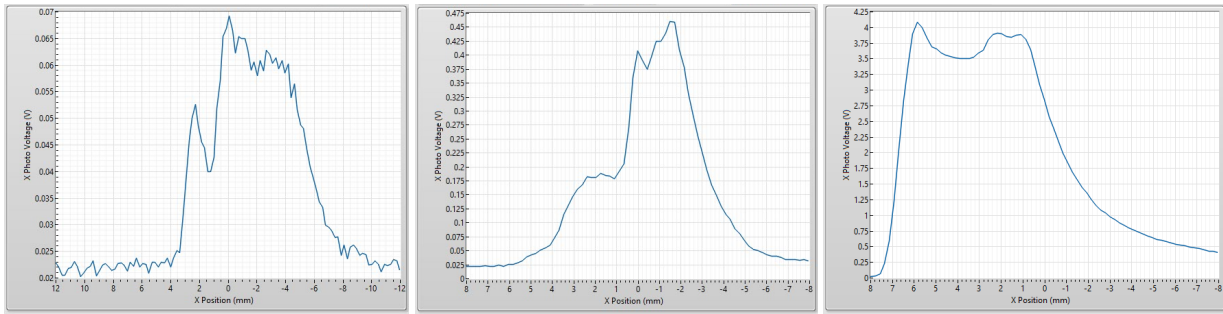


Fig. 7. Beam profiles measured using D-Pace’s commercial UniBEaM with 200 $\mu$  Ce<sup>3+</sup> fiber, on AEC-LHEP’s IBA Cyclotron. 18MeV H<sup>+</sup> currents 12pA, 62pA, 100pA, 225pA, 1nA, and 400nA

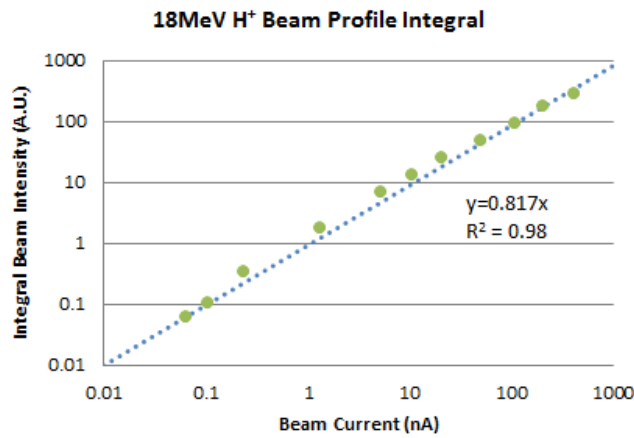


Fig. 8. Integral of beam intensity profile vs beam current measured by Faraday cup

The UniBEaM system commercialized by D-Pace achieved a SNR of 2 at 12pA, and 15 at 100pA, for 18MeV H<sup>+</sup>, using the significantly lower cost photo-current-sensing architecture shown in Fig. 3. Using this 18MeV beam as an example, customers operating with beam currents exceeding 100pA could use this cost-effective design, while customers with beam currents less than 100pA could use the higher-performance, higher-cost photon-counting approach use by AEC-LHEP.

D-Pace also used the commercial UniBEaM system to tune the beamline of our TRIUMF-licensed DC volume-cusp H<sup>-</sup> ion source. Fig. 9 shows the effects of beam steering on the position of a 25keV 500 $\mu$ A proton beam. For these measurements, a non-doped fiber was used, which had sufficient impurities to produce sufficient scintillation for this high current, low energy beam.

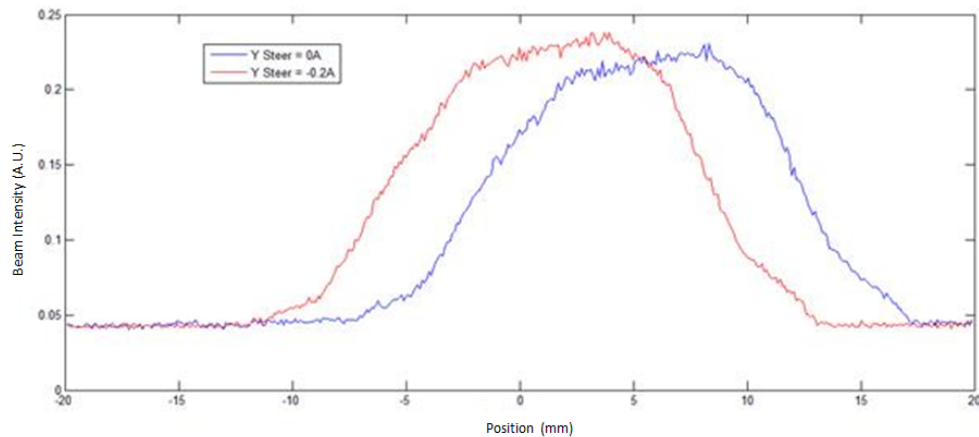


Fig. 9. Beam profiles showing the effects of a beam steering of a 25keV 500 $\mu$ A H<sup>-</sup> beam

Mones et al. (2006) at the University of Milano-Bicocca's Department of Materials Science studied the use of rare-earth doped fibers for dosimetry, measuring radio luminescence emitted from a Clinac 2100 CD (Varian, USA) medical linear accelerator, with both photons and electrons. Their prototype had satisfactory reproducibility and good linearity over the dose range of interest (from few cGy to approximately 10 Gy). D-Pace also made preliminary measurements of the scintillation of Ce<sup>3+</sup> doped SiO<sub>2</sub> fibers with X-ray (6MeV, 15MeV) and electron (6MeV, 12MeV, 20MeV) beams emitted from a Varian Model iX5 medical linear accelerator. These results will be discussed in future publications.

## 5. Future Work

Nesteruk et al. (2015), at the AEC-LHEP, demonstrated the use of UniBEaM for measuring the transverse emittance of their IBA Cyclone cyclotron using two different methods – quadrupole variation and multiple UniBEaM probes. D-Pace plans to develop software for using UniBEaM for transverse emittance calculations.

D-Pace is designing 50mm beam diameter (64mm beam pipe) and 75mm beam diameter (100mm beam pipe) versions of UniBEaM – all of which will have the same insertion length as the 25mm beam diameter (38mm beam pipe) probe described in this paper. A UHV version of UniBEaM is in progress.

D-Pace is investigating the manufacturability of scintillation fibers with diameters of 50 $\mu$ m and smaller for the purpose of scanning beams with diameters less than 1000 $\mu$ m.

D-Pace is working with industrial and scientific partners to explore applications for UniBEaM. D-Pace has an early adopter program where UniBEaM systems are offered at discounted rates in exchange for data sharing and product feedback.

## 6. Conclusions

UniBEaM is an alternative to conventional wire scanners, and offers the particle accelerator industry a compact and cost effective means of measuring charged particle, electron and x-ray beam intensity profiles over a large range of currents and beam energies.

## Acknowledgments

On behalf of D-Pace, the author gratefully acknowledges the financial contributions of the following Canadian government programmes: SRED and NRC. In addition, the author wishes to express his appreciation to the AEC-LHEP, University of Bern for their ongoing support with the commercialization of UniBEaM, and to the Department of Materials Science, University of Milano-Bicocca for their expertise in scintillating optical fibers. D-Pace also thanks Buckley Systems (Auckland, NZ) for their financial support of this project.

## References

- Dehnel, M.P., Potkins, D.E., Stewart, T.M., 2013. An Integrated Self-Supporting, Mini-Beamline for PET Cyclotrons. *Cyclotrons 2013 Conf. Proc.*, 251-253.
- Braccini, S., Ereditato, A., Giacoppo, F., Kreslo, I., Nesteruk, K.P., Nirko, M., Weber, M., Scampoli, P., Neff, M., Pilz, S., Romano, V., 2012. A beam monitor detector based on doped silica and optical fibres, *JINST* 7, T02001.
- Auger, M., Braccini, S., Carzaniga, T.S., Ereditato, A., Nesteruk, K.P., Scampoli, P., 2016. A detector based on silica fibers for ion beam monitoring in a wide current range, *JINST* 11, P03027.
- Nesteruk, K. P., Auger, M., Braccini, S., Carzaniga, T.S., Ereditato, A., Scampoli, P., 2015. Study of the transverse beam emittance of the Bern medical cyclotron, *Proceedings of IBIC2015*, MOPB041.
- Mones, E., Veronese, I., Moretti, F., Fasoli, M., Loi, G., Negri, E., Brambilla, M., Chiodini, N., Brambilla, G., Vedda, A., 2006. Feasibility study for the use of  $Ce^{3+}$  - doped optical fibres in radiotherapy, *Nuclear Instruments and Methods in Physics Research, A* 562, 449-455.
- Vedda, A., Chiodini, N., Di Martino, D., Fasoli, M., Keffer, S., Lauria, A., Martini, M., Moretti, F., Spinolo, G., 2004.  $Ce^{3+}$  - doped fibers for remote radiation dosimetry, *Applied Physics Letters*, Volume 85, Number 26.
- Strehl, P., 2006. *Beam Instrumentation and Diagnostics*. Springer-Verlag, Berlin Heidelberg, pp. 106-111.
- Strehl, P., 1995. Ion Beam Diagnostics, in "Ion Sources". In: Wolf, B (Ed.). CRC Press, Darmstadt, p. 419.
- Ziegler, J.F., Ziegler, M.D., Biersack, J.P., 2010. SRIM - The stopping and range of ions in matter, *Nuclear Instruments and Methods in Physics Research Section B*, Volume 268, Issue 11-12, p. 1818-1823.



# A system for online beam emittance measurements and proton beam characterization

---

K. P. Nesteruk,<sup>a,1</sup> M. Auger,<sup>a</sup> S. Braccini,<sup>a</sup> T. S. Carzaniga,<sup>a</sup> A. Ereditato,<sup>a</sup> P. Scampoli,<sup>a,b</sup>

<sup>a</sup>*Albert Einstein Center for Fundamental Physics (AEC),  
Laboratory for High Energy Physics (LHEP), University of Bern,  
Sidlerstrasse 5, CH-3012 Bern, Switzerland*

<sup>b</sup>*Department of Physics “E. Pancini”, University of Naples Federico II,  
Complesso Universitario di Monte S. Angelo, I-80126, Naples, Italy*

*E-mail:* [konrad.nesteruk@lhep.unibe.ch](mailto:konrad.nesteruk@lhep.unibe.ch)

**ABSTRACT:** A system for online measurement of the transverse beam emittance was developed. It is named <sup>4</sup>PrOBεaM (4-Profiler Online Beam Emittance Measurement) and was conceived to measure the emittance in a fast and efficient way using the multiple beam profiler method. The core of the system is constituted by four consecutive UniBEaM profilers, which are based on silica fibers passing across the beam. The <sup>4</sup>PrOBεaM system was deployed for characterization studies of the 18 MeV proton beam produced by the IBA Cyclone 18 MeV cyclotron at Bern University Hospital (Inselspital). The machine serves daily radioisotope production and multi-disciplinary research, which is carried out with a specifically conceived Beam Transport Line (BTL). The transverse RMS beam emittance of the cyclotron was measured as a function of several machine parameters, such as the magnetic field, RF peak voltage, and azimuthal angle of the stripper. The beam emittance was also measured using the method based on the quadrupole strength variation. The results obtained with both techniques were compared and a good agreement was found. In order to characterize the longitudinal dynamics, the proton energy distribution was measured. For this purpose, a method was developed based on aluminum absorbers of different thicknesses, a UniBEaM detector, and a Faraday cup. The results were an input for a simulation of the BTL developed in the MAD-X software. This tool allows machine parameters to be tuned online and the beam characteristics to be optimized for specific applications.

**KEYWORDS:** Beam-line instrumentation (beam position and profile monitors; beam-intensity monitors; bunch length monitors); Instrumentation for particle accelerators and storage rings - low energy (linear accelerators, cyclotrons, electrostatic accelerators); Beam dynamics

ARXIV EPRINT: [1705.07486](https://arxiv.org/abs/1705.07486)

---

<sup>1</sup>Corresponding author.

---

## Contents

<b>1</b>	<b>Introduction</b>	<b>1</b>
<b>2</b>	<b>Transverse RMS beam emittance</b>	<b>3</b>
<b>3</b>	<b>Materials and methods</b>	<b>4</b>
3.1	<sup>4</sup> PrOBεaM: a system for online measurement of the transverse beam emittance	4
3.2	Experimental method for measurement of the proton energy distribution	5
<b>4</b>	<b>Characterization of the 18 MeV proton beam from the Bern medical cyclotron</b>	<b>6</b>
4.1	Transverse RMS beam emittance as a function of cyclotron parameters	6
4.2	Transverse RMS beam emittance for the standard cyclotron settings	9
4.3	Proton energy distribution	12
4.4	Simulation of the Beam Transport Line	12
<b>5</b>	<b>Conclusions and outlook</b>	<b>14</b>

---

## 1 Introduction

Cyclotrons are nowadays common tools in medical applications and are used for the production of radioisotopes, as well as for cancer proton therapy. Medical cyclotrons have a high scientific potential, well beyond the aim for which they were designed [1]. To exploit that, knowledge of the beam characteristics as a function of the main operational parameters is essential.

A cyclotron laboratory for radioisotope production and multi-disciplinary research is in operation at Bern University Hospital (Inselspital) [2]. This facility hosts the IBA Cyclone 18 MeV proton cyclotron shown in figure 1. This kind of machine is able to accelerate  $H^-$  and  $D^-$  ions to the energy of 18 MeV and 9 MeV, respectively. However, to maximize the efficiency for daily medical radioisotope production in Bern, the machine is equipped with two  $H^-$  ion sources. High beam currents up to 150  $\mu A$  are provided in single or dual beam mode. Extraction is realized by stripping  $H^-$  ions in a 5  $\mu m$  thick pyrolytic carbon foil.

The Bern laboratory is equipped with a 6.5 m long Beam Transport Line (BTL), which is rare for a hospital based facility. It allows multi-disciplinary research to be carried out in parallel with daily radioisotope production. A schematic view of BTL is presented in figure 2. Alternate beam focusing and defocusing is realized by two horizontal-vertical quadrupole doublets. One is located in the cyclotron bunker, while the other in that of the BTL. A movable cylindrical neutron shutter is placed at the entrance of the BTL bunker to minimize the penetration of neutrons during routine production of radioisotopes. Experimental equipment used for scientific activities, such as particle detectors or specific target stations, are installed at the end of the BTL. For several research activities performed with the BTL, low beam current intensities (down to pA range) are required. This is



**Figure 1.** The Bern cyclotron opened during maintenance.

unusual for medical cyclotrons. However, the feasibility of stable operation of the Bern cyclotron at such low beam intensities was proven [3].

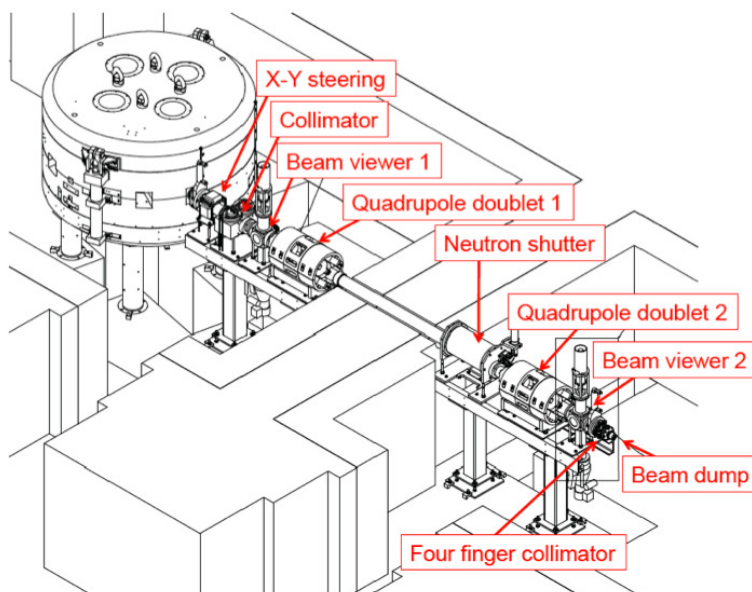


**Figure 2.** Schematic view of the Bern cyclotron facility, where all the main components of the BTL are highlighted.

For beam profile measurements, beam monitors developed by our group and named UniBEaM are used [4]. The UniBEaM detector is a compact device based on doped silica and optical fibers, which allows for fully automatized measurements of transverse beam profiles. A sensing

fiber moves transversally across the beam and charged particles passing through the fiber cause scintillation. The produced light is transported to a read-out device, the signal is digitized and plotted online as a function of the fiber position. The precise measurement of the beam profile is at the basis of the study presented in this paper. The characterization of the cyclotron beam was performed by measuring both the transverse RMS beam emittance and the proton energy distribution. In particular, a system based on four UniBEaM detectors and named <sup>4</sup>PrOBεaM (4-Profiler Online Beam Emittance Measurement) was developed to provide an online measurement of the beam emittance. This system was employed for measurements of the transverse beam emittance as a function of the main cyclotron parameters. The experimental results were an input for a simulation of the BTL developed with the MAD-X software [5]. This simulation is an important tool for optimizing irradiations for multi-disciplinary research. In this paper, we report on the first comprehensive study of the proton beam of the IBA 18 MeV cyclotron installed in Bern. It was performed for beam currents in the nA range, the typical operating conditions for research purposes.

## 2 Transverse RMS beam emittance

The beam emittance is the main physical quantity used to characterize an accelerated particle beam [6]. In the case of transverse beam dynamics, the phase space is given by two variables for both horizontal and vertical planes: position ( $x$  and  $y$ ) and momentum ( $p_x$  and  $p_y$ ). The momenta are typically expressed by the angles  $x' \approx p_x/p_z$  and  $y' \approx p_y/p_z$ , where  $p_z$  is the longitudinal momentum. In the phase space  $(x, x')$  or  $(y, y')$ , the points representing the particles are comprised inside an ellipse. The area of the phase space ellipse divided by  $\pi$  is called the transverse beam emittance and is usually given in mm-mrad. In further considerations, only the horizontal plane is discussed being the vertical plane completely equivalent.

Realistic beams are usually far from being Gaussian and an appropriate statistical approach is required for a reliable estimation of the transverse beam emittance. In the case of an arbitrary density distribution  $\rho(x, x')$ , the following moments can be defined:

$$\langle x^2 \rangle = \frac{\iint (x - \mu)^2 \rho(x, x') dx' dx}{\iint \rho(x, x') dx' dx} \quad (2.1)$$

$$\langle x'^2 \rangle = \frac{\iint (x' - \mu')^2 \rho(x, x') dx' dx}{\iint \rho(x, x') dx' dx}, \quad (2.2)$$

and the covariance:

$$\langle xx' \rangle = \frac{\iint (x - \mu)(x' - \mu') \rho(x, x') dx' dx}{\iint \rho(x, x') dx' dx}, \quad (2.3)$$

where  $\mu$  and  $\mu'$  are the expectation values for  $x$  and  $x'$ , respectively. The beam matrix  $\sigma(s)$  at the location  $s$  along the beamline is therefore expressed in the following way:

$$\sigma(s) = \begin{pmatrix} \sigma_{11} & \sigma_{12} \\ \sigma_{21} & \sigma_{22} \end{pmatrix} = \begin{pmatrix} \langle x^2 \rangle & \langle xx' \rangle \\ \langle xx' \rangle & \langle x'^2 \rangle \end{pmatrix}. \quad (2.4)$$

The RMS beam emittance  $\varepsilon_{rms}$  is then given by the determinant of the  $\sigma(s)$  matrix

$$\varepsilon_{rms} = \sqrt{\det(\sigma(s))}, \quad (2.5)$$

and is independent of the location  $s$ , according to Liouville's theorem.

### 3 Materials and methods

#### 3.1 ${}^4\text{PrOB}\epsilon\text{aM}$ : a system for online measurement of the transverse beam emittance

The  ${}^4\text{PrOB}\epsilon\text{aM}$  system was conceived to measure the transverse beam emittance in a fast and efficient way using the multiple beam profiler method [7]. The use of multiple beam profilers does not require any prior knowledge of the optical elements of the beam transport. The system consists of four UniBEaM detectors and its total length is 54 cm, which allows  ${}^4\text{PrOB}\epsilon\text{aM}$  to be installed at nearly any location along beamlines or directly at the accelerator output. For the measurements reported in this paper, the system was followed by a Faraday cup, which terminated the beamline to measure the beam current, as shown in figure 3. For the measurements in the complementary plane,  ${}^4\text{PrOB}\epsilon\text{aM}$  was rotated by 90 degrees. All four beam profiles are measured simultaneously in order

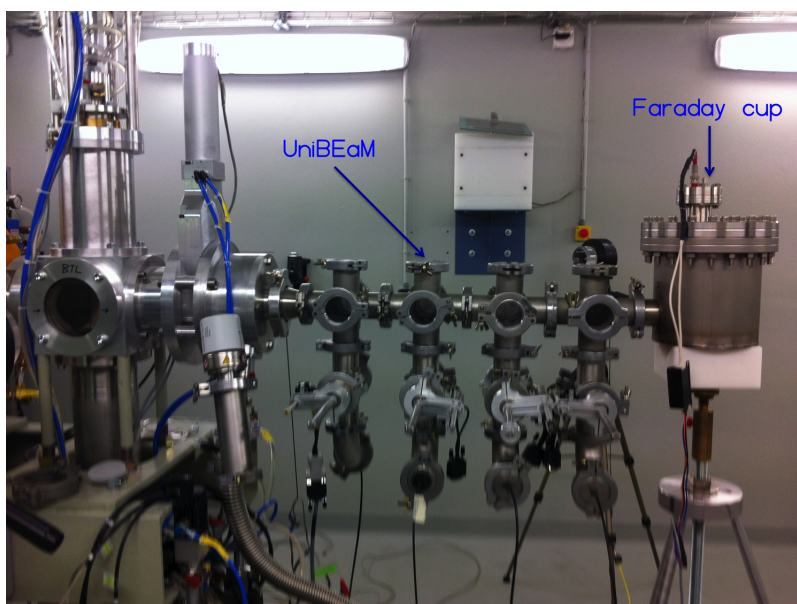


**Figure 3.** The  ${}^4\text{PrOB}\epsilon\text{aM}$  system and a Faraday cup installed on the BTL of the Bern cyclotron.

to minimize the influence of possible beam instabilities. Depending on the beam current range, different sensing fibers are used. For currents exceeding 1 nA, UniBEaMs are usually operated with non-doped optical fibers. Beam profiles are measured at four successive locations around a beam waist separated by a drift length  $L = 135$  mm, as depicted in figure 4. The optical signal from each detector is transmitted to a single-photon counter (commercial device of ID Quantique SA) and digitized. The whole data acquisition process consists of one full beam scan and is controlled by a Raspberry Pi 2 module with dedicated software. When the beam scan is complete, a ROOT [8] script is automatically launched, in which the whole data analysis is implemented. All four beam profiles are plotted in a separate window as histograms and saved in a pdf file. A single measurement of the beam emittance takes less than 1 minute. The variance is calculated for each histogram of the profile giving an estimate of  $\sigma_{11}(s)$  component of the beam matrix  $\sigma(s)$  at the location  $s$ . The

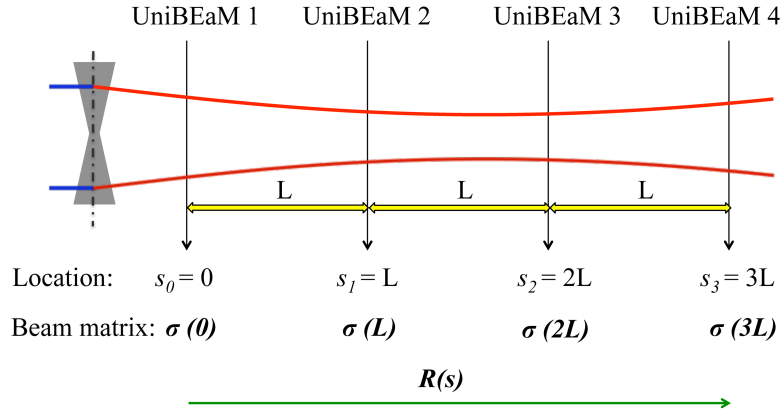


**Figure 4.** Sketch of principle of the multiple beam profiler method for the measurement of the transverse beam emittance.

beam transfer matrix  $R(s)$  involves only a drift:

$$R(s) = \begin{pmatrix} 1 & s \\ 0 & 1 \end{pmatrix}. \quad (3.1)$$

The beam matrix at any location  $s$  with respect to the location of the first UniBEaM detector ( $s_0 = 0$ ) is therefore given by the formula:

$$\sigma(s) = R(s)\sigma(0)R(s)^T. \quad (3.2)$$

From equation (3.2) it can be derived that  $\sigma_{11}(s)$  is a quadratic function of  $s$ :

$$\begin{aligned} \sigma_{11}(s) &= \sigma_{22}(0)s^2 + 2s\sigma_{12}(0) + \sigma_{11}(0) \\ &= f(s; \sigma_{11}(0), \sigma_{12}(0), \sigma_{22}(0)), \end{aligned} \quad (3.3)$$

where  $\sigma_{11}(0)$ ,  $\sigma_{12}(0)$ , and  $\sigma_{22}(0)$  are the components of the  $\sigma(0)$  matrix. These components and consequently the transverse emittance are evaluated by fitting the  $f(s; \sigma_{11}(0), \sigma_{12}(0), \sigma_{22}(0))$  function using the four data points representing the estimated variance values as a function of the location  $s$ . The plot with the corresponding best fit is displayed and saved in a file.

### 3.2 Experimental method for measurement of the proton energy distribution

In order to characterize the energy distribution of the beam extracted to the BTL, a set of Al absorbers of different thickness was employed. Each thickness corresponded to a different maximum beam energy of the protons that could be stopped within the absorber, as reported in table 1. The maximum energy was determined by performing a SRIM [9] simulation. For each absorber, a profile of the incident beam was measured by a UniBEaM detector and the intensity of the transmitted beam by a Faraday cup, as illustrated in figure. 5. The UniBEaM detector was located in front of the absorber and was used to normalize the measured beam current. For the  $i$ -th absorber, the beam profile integral  $S_i$  was calculated and the intensity  $I_i$  of the transmitted beam was obtained from an electrometer. The profile integral holds a linear dependence on the beam current [4]. A reference

measurement was performed without any absorber, giving the integral  $S_0$  and the beam current  $I_0$ . The fraction of the beam that was transmitted for each absorber  $T_i$  is computed from the following formula:

$$T_i = \frac{S_0}{S_i} \cdot \frac{I_i}{I_0} \quad i = 1, 2, \dots, 9. \quad (3.4)$$

The probability  $P_{i,i+1}$  of finding a proton of the energy between the maximum proton energies corresponding to the absorbers  $i$  and  $i + 1$  is given by the expression:

$$P_{i,i+1} = T_i - T_{i+1} \quad i = 1, 2, \dots, 8. \quad (3.5)$$

**Table 1.** Aluminum absorbers used for the measurement of the proton energy distribution.

#	Thickness [mm]	Max. proton energy [MeV]
1	1.42	16.0
2	1.50	16.5
3	1.58	17.0
4	1.67	17.5
5	1.75	18.0
6	1.84	18.5
7	1.93	19.0
8	2.02	19.5
9	2.11	20.0

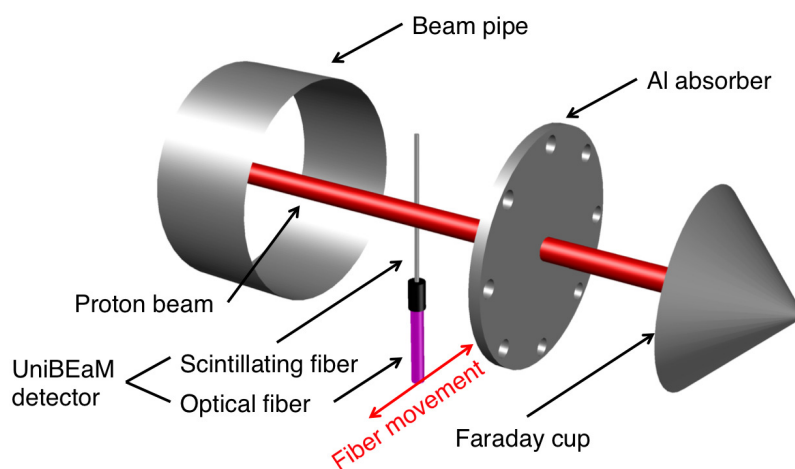


**Figure 5.** Schematic of the experimental method for the measurement of the proton energy distribution.

## 4 Characterization of the 18 MeV proton beam from the Bern medical cyclotron

### 4.1 Transverse RMS beam emittance as a function of cyclotron parameters

For research purposes, the Bern cyclotron is operated in the manual mode, which allows the cyclotron parameters to be tuned in order to obtain beams according to specific needs. These

parameters include the main coil current, RF peak voltage, azimuthal stripper angle, and ion source arc current. For standard irradiations at the BTL, the values corresponding to the maximum beam transmission are used, which are reported in table 2. For specific needs non-standard cyclotron parameters are chosen. In particular, the settings leading to non-optimal isochronism operation are deliberately selected when low current beams are required, as reported in [3]. To keep the same beam intensity over the course of long irradiations, the cyclotron parameters have to be continuously tuned. Therefore, the influence of a few important parameters on the beam emittance was studied by measuring the transverse RMS emittance as a function of the varied parameter. The  $^4\text{PrOB}\epsilon\text{aM}$  system, able to make a single emittance measurement in a short time, was employed.

**Table 2.** The standard settings of the cyclotron parameters used for research purposes.

Cyclotron parameter	Value
Main coil	136.9-137.2 A
RF peak voltage	32 kV
Stripper angle	84.2°
Ion source	1 mA

#### Variation of the main coil current

The current in the main coil is proportional to the magnetic field and thus influences isochronism. It is crucial for obtaining low intensity beams down to the pA range, since it allows the cyclotron to be operated in the regime of non-optimal isochronism. Moreover, the set point for the optimal isochronism has the tendency to drift towards higher values of the main coil current during long cyclotron runs. The influence of the main coil current on the transverse emittance was studied by gradually changing it and measuring the corresponding RMS emittance values. The other cyclotron parameters were set to the standard values (table 2). The beam current was measured by means of a Faraday cup installed at the end of the beamline. The minimum and maximum main coil currents were determined by requiring a beam intensity of the order of 1 nA. Since the isochronism depends on the operation time, the main coil scans for horizontal and vertical planes were first performed for “cold” machine, meaning that the cyclotron had not been operated before the measurement for at least a few hours. The results for the horizontal and vertical planes are presented in figure 6. In the case of the horizontal plane the emittance after an initial drop has a tendency to grow with the main coil current until the isochronism condition is reached. At the isochronism the emittance reaches a plateau corresponding to the region of the standard operation of the cyclotron. After that the emittance decreases reaching a local minimum. This is followed by another increase with a local maximum at a current of about 137.3 A. In this region the beam is unstable and this effect may be due to the interception of the beam by the body of the second ion source or to a resonant condition producing beam losses, as reported in [3]. In the vertical plane, the variation of the emittance is much smaller and the plateau region is wider, as there is no acceleration in this plane. The measurements were performed several times in consecutive days giving reproducible results.

The full main coil scan was repeated for both planes when the machine was “warm”, meaning that measurements were taken after a few hours of operation. The comparison of the results for the horizontal and vertical planes are presented in figure 7. An offset of the curve corresponding

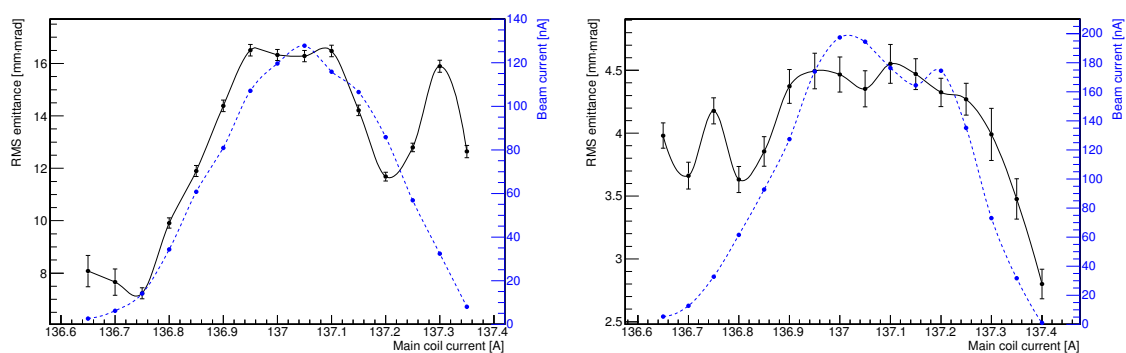


**Figure 6.** The horizontal (left) and vertical (right) transverse RMS emittance as a function of the main coil current for cold machine. The right vertical axis and blue dashed curve correspond to the beam current.

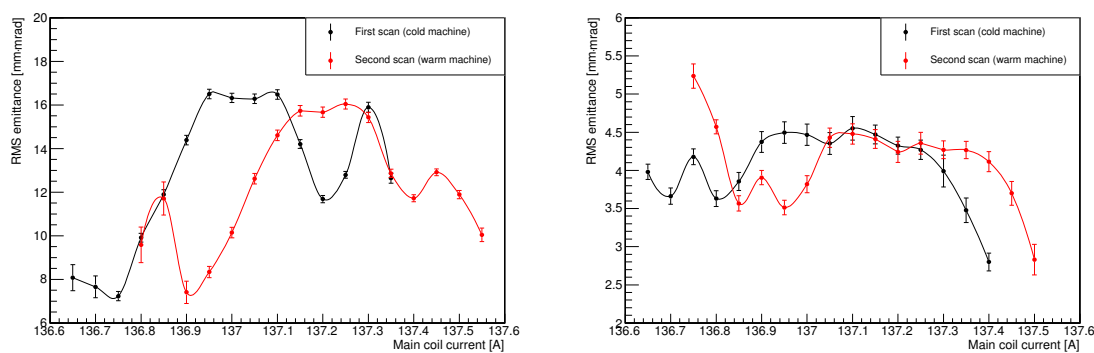


**Figure 7.** Comparison of the dependence of the horizontal (left) and vertical (right) RMS transverse emittance on the main coil current for cold and warm machine.

to the second scan (warm machine) is clearly visible for both the horizontal and vertical planes. This offset is due to the warm-up of the machine showing the tendency of the optimal isochronism condition to drift towards higher values of the main coil current over the course of the cyclotron operation. The curve patterns for both scans present differences mostly for the extreme values of the main coil current. This is probably due to the fact that change in the range of the main coil operation extends measurable non-isochronous region. Furthermore, instabilities are observed for very low and very high values of the main coil current.

#### Variation of the RF peak voltage

The peak voltage of the 42 MHz RF system is responsible for acceleration and extraction of  $H^-$  ions from the chimney of the ion source, and can be varied from 27 kV to 37 kV. The RF peak voltage was varied in the full range in steps of 0.5 kV. The beam current was again monitored by means of the Faraday cup. The main coil current was set to 137.05 A and 137.00 A for the horizontal and vertical planes, respectively. These values of the main coil current provided operation in the region of the emittance stability (figures 6 and 7). The results for the horizontal and vertical planes are presented in figure 8. In both planes oscillations of the emittance occur, while the emittance values at the local minima tend to increase. An exact explanation of the observed effects is very

difficult, since the centering of the beam is unknown, as there is no differential radial probe inside the machine. Also, the phase of the radial betatron oscillations is not controlled. The changes of the emittance measured at the chosen stripper azimuthal angle are caused by a superposition of the RF voltage modification, beam off-centering, and phase of the betatron oscillations. The total emittance of the extracted beam is a sum of emittances of beam parts extracted at the turns  $N, N + 1, N + 2, \dots$ . One may expect that higher RF voltages reduce the number of turns during acceleration and at the same time enlarge the accepted range of initial RF phases passing from the ion source to the stripper foil. This may be the reason for observing slightly larger beam emittances for larger values of the RF peak voltage.

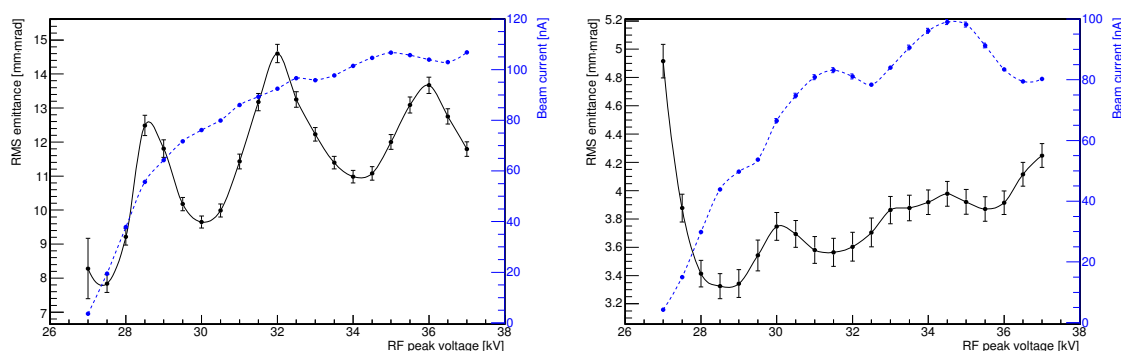


**Figure 8.** The horizontal (left) and vertical (right) transverse RMS emittance as a function of the RF peak voltage. The right vertical axis and blue dashed curve correspond to the beam current.

### Variation of the stripper angle

The stripper angle can be adjusted to optimize the extracted proton beams. In most irradiations a default stripper angle of  $84^\circ$  is used. The optimal angle can change due to stripper deformation or when a new stripper is installed during periodical cyclotron maintenance. The azimuthal angle was varied from the nominal value to  $96.4^\circ$ . The RF peak voltage and the main coil current were set for these measurements to 32 kV and 137.05 A, respectively. Since the nominal value of the stripper angle is chosen so that the beam intensity is maximum, the beam current monitored by the Faraday cup was decreasing with the increase of the angle. The transverse RMS emittance was found to decrease in the horizontal plane (figure 9 (left)) and increase in the vertical one (figure 9 (right)). The interpretation of the obtained result is difficult. It is likely that these changes of the beam emittance would not be observed if the beam was well centered and passed through the stripper in a single turn. Therefore, the results indicate imperfections in the studied machine.

## 4.2 Transverse RMS beam emittance for the standard cyclotron settings

The transverse RMS beam emittance was measured with two different methods for the cyclotron settings typically used for multi-disciplinary research with the BTL (table 2). The first technique employed was the variation of the quadrupole strength [7, 10]. For this method, the last quadrupole magnet of the BTL, which is defocusing in the horizontal plane and focusing in the vertical, was varied. The corresponding beam profiles at a distance of 694 mm from the quadrupole were measured with the UniBEaM detector for each magnet setting. The second technique was the use of

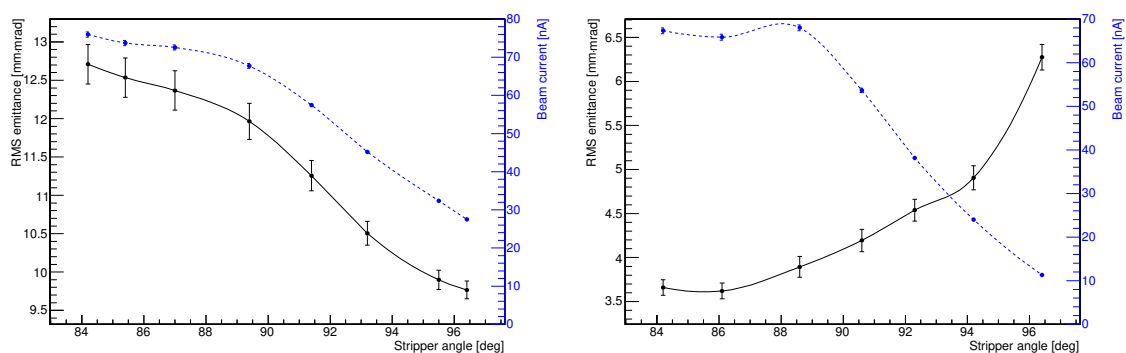


**Figure 9.** The horizontal (left) and vertical (right) transverse RMS emittance as a function of the stripper angle. The right vertical axis and blue dashed curve correspond to the beam current.

multiple beam profilers, for which the <sup>4</sup>PrOBεaM system was again used. During the measurements of the transverse beam emittance, the cyclotron parameters were kept constant and set to the standard values. The beam current, as monitored by means of a Faraday cup, was about 250 nA.

The estimated variance in the horizontal plane  $\langle x^2 \rangle$  as a function of the quadrupole current together with the fitted curve for the quadrupole variation method is shown in figure 10. A similar curve was obtained for the vertical plane, as presented in our preliminary study [11]. Fit results for both planes and the corresponding emittance values are listed in table 3. The transverse RMS emittance in the horizontal plane is 3.6 times larger than the one in the vertical plane.

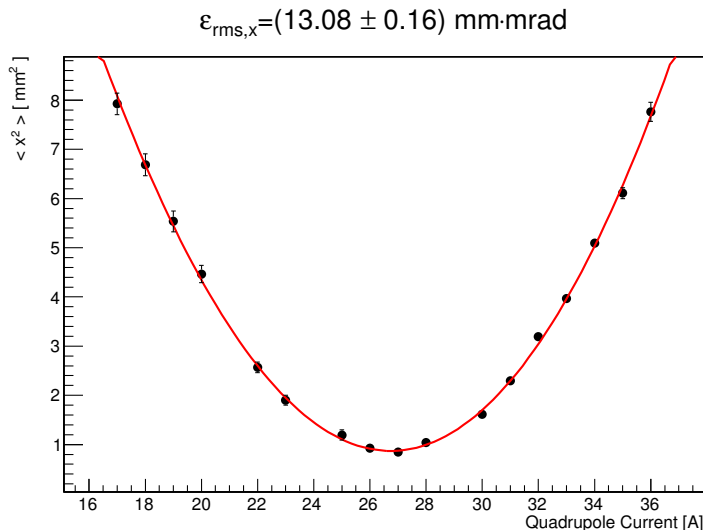


**Figure 10.** Variance as a function of the quadrupole current obtained in the horizontal plane. The red line corresponds to the best fit.

The estimated variance in the horizontal plane  $\langle x^2 \rangle$  as a function of the location  $s$  together with the fitted curve for the multiple beam profiler method is shown in figure 11. A similar curve was obtained for the vertical plane, as reported in [11]. Fit results for both planes and the corresponding

**Table 3.** Fit parameters and the RMS emittance values obtained by quadrupole variation for both horizontal and vertical planes.

Fit parameter	Horizontal plane	Vertical plane
$\sigma_{11}$ [ $\text{mm}^2$ ]	$200.23 \pm 0.08$	$21.59 \pm 0.36$
$\sigma_{12}$ [ $\text{mm}\cdot\text{mrad}$ ]	$-322.66 \pm 0.08$	$-2.98 \pm 0.07$
$\sigma_{22}$ [ $\text{mrad}^2$ ]	$520.80 \pm 0.22$	$1.02 \pm 0.02$
$\tilde{\chi}^2$	0.98	1.04
$\varepsilon_{rms}$ [ $\text{mm}\cdot\text{mrad}$ ]	$13.08 \pm 0.16$	$3.63 \pm 0.04$

emittance values are given in table 4.

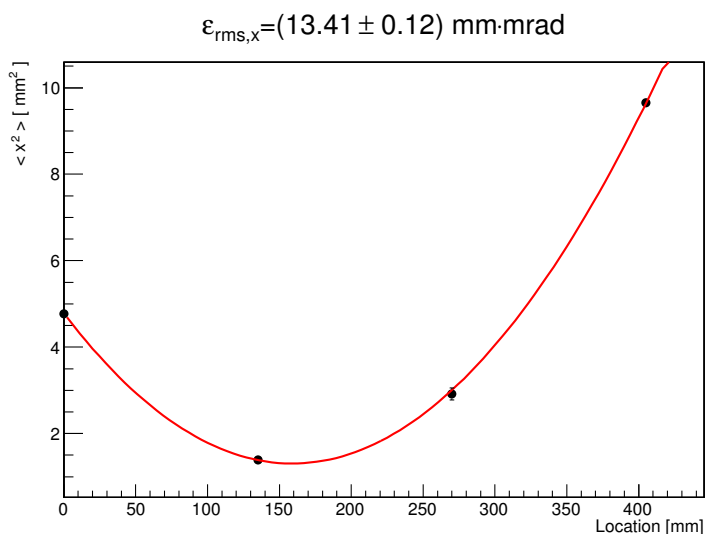


**Figure 11.** Variance as a function of the location obtained in the horizontal plane. The red line corresponds to the best fit.

**Table 4.** Fit parameters and the RMS emittance values obtained by using multiple profilers for both horizontal and vertical planes.

Fit parameter	Horizontal plane	Vertical plane
$\sigma_{11}$ [ $\text{mm}^2$ ]	$4.79 \pm 0.09$	$0.75 \pm 0.04$
$\sigma_{12}$ [ $\text{mm}\cdot\text{mrad}$ ]	$-21.90 \pm 0.48$	$-1.06 \pm 0.19$
$\sigma_{22}$ [ $\text{mrad}^2$ ]	$137.72 \pm 2.06$	$17.99 \pm 1.15$
$\tilde{\chi}^2$	0.47	0.76
$\varepsilon_{rms}$ [ $\text{mm}\cdot\text{mrad}$ ]	$13.41 \pm 0.12$	$3.53 \pm 0.13$

The results obtained by employing the two methods were found to be in agreement within  $1.65\sigma$  and  $0.71\sigma$  for the horizontal and vertical planes, respectively. The transverse RMS beam emittance in the horizontal plane is almost 4 times larger than the one in the vertical plane. This is typical for cyclotrons where acceleration takes place in the horizontal plane. This causes an

increase of the particle position spread along the  $x$ -direction.

### 4.3 Proton energy distribution

The results obtained for 9 aluminum absorbers are given in figure 12. The probability density is shown for each bin of 0.5 MeV width. A mean energy of  $(18.3 \pm 0.3)$  MeV and an RMS of  $(0.4 \pm 0.2)$  MeV were obtained. Additionally, a fit using a Verhulst function [12] was performed with  $\chi^2 = 0.6$ . The fitted function was chosen due to the skewness of the measured distribution and it is defined as:

$$P(x) = \frac{1}{A \cdot B} \cdot \frac{(2^A - 1) \cdot \exp\left(\frac{x-C}{B}\right)}{\left(1 + (2^A - 1) \cdot \exp\left(\frac{x-C}{B}\right)\right)^{\frac{A+1}{A}}}, \quad (4.1)$$

where  $A$ ,  $B$ , and  $C$  are the fit parameters. For the best fit they were found to be:  $A = 0.13 \pm 0.03$ ,  $B = 0.19 \pm 0.03$ , and  $C = 0.24 \pm 0.02$ . As expected, the mean beam energy at the BTL was found to be larger than the nominal one. This is due to the fact that a specific stripper holder is used which locates the stripper foil at a radius 5 mm larger with respect to the other outlets [2].

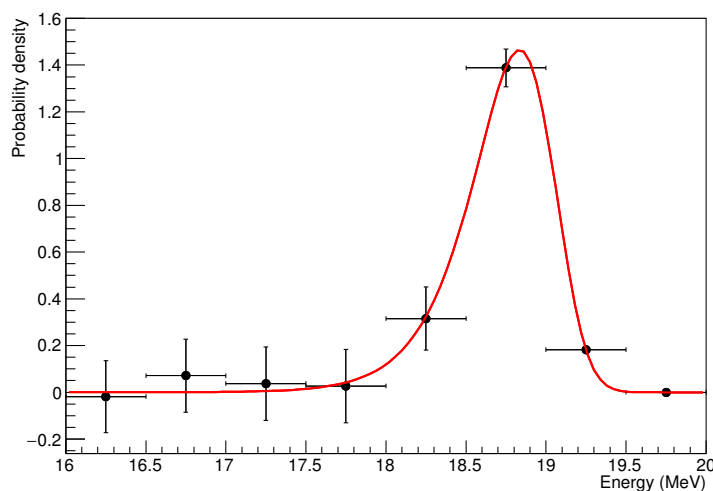


**Figure 12.** Distribution of the proton energy. The red line corresponds to the best fit of the Verhulst function.

### 4.4 Simulation of the Beam Transport Line

Methodical Accelerator Design (MAD-X) is a multi-purpose tool for charged-particle optics design and studies in alternating-gradient accelerators and beamlines. It was developed and is maintained by the Beams Department at CERN [5]. It allows defining a beamline as a sequence of beam optics components, calculating Twiss parameters at their locations, and finding beamline component settings corresponding to specific constraints. A simulation of the BTL of the Bern cyclotron was implemented on the basis of the measurements performed with the multiple beam profiler method reported in this paper. The Twiss parameters were calculated at the location of the first beam profiler and transported back to the beginning of the BTL by means of linear beam transport algebra. In

this way the beam phase space at the injection to the BTL was reconstructed assuming Gaussian distributions of  $(x, x')$  and  $(y, y')$ . The latter assumption leads to an ellipse limiting a certain fraction of the beam in the phase space. As an example, the  $1\sigma$ -ellipses for the standard cyclotron settings are shown in figure 13. The simulation of the BTL is used for beam optimization in various experiments. In figure 14 a simulated beam envelope in both horizontal and vertical planes for the standard cyclotron parameters and standard quadrupole settings is reported. This tool is crucial to design experiments for radiation hardness studies, irradiation of solid targets, and radiobiological research activities.

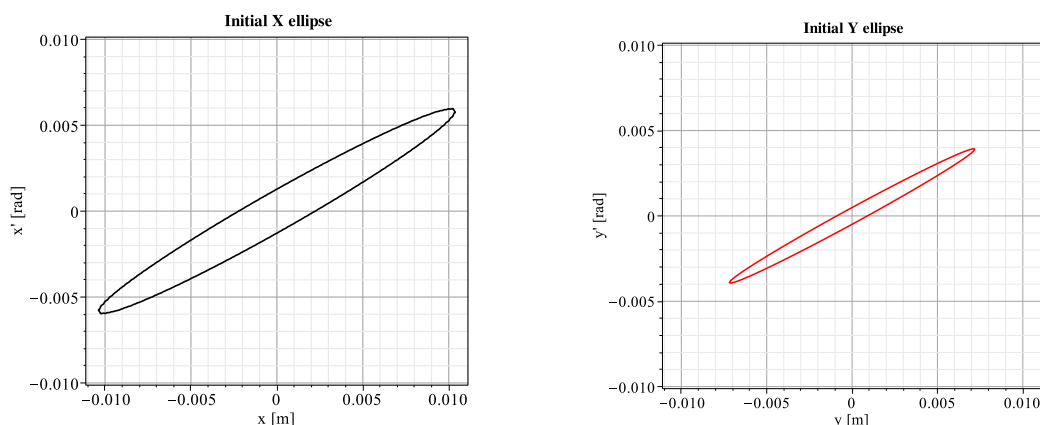


**Figure 13.** The horizontal (left) and vertical (right)  $1\sigma$ -phase-space ellipses at the injection to the BTL.

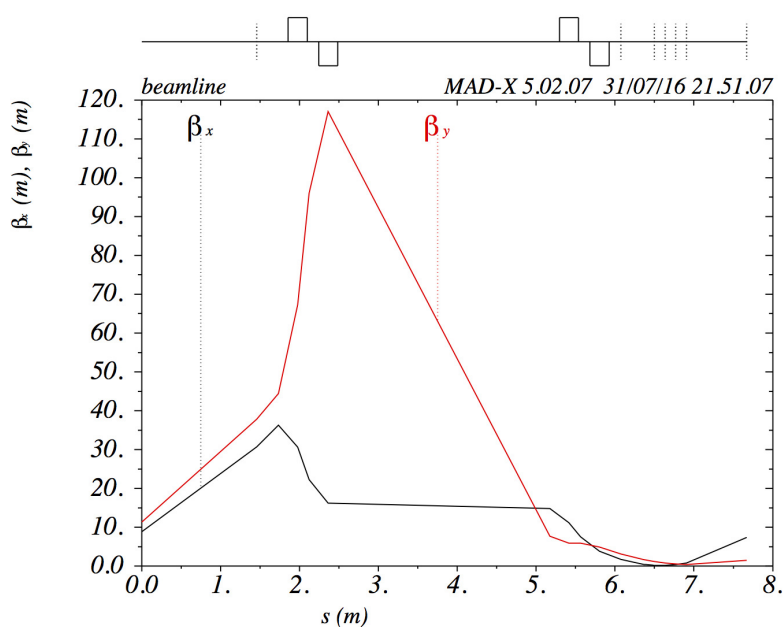


**Figure 14.** Simulated beam envelope in both horizontal and vertical planes.

## 5 Conclusions and outlook

A system for online measurement of the transverse beam emittance, named  ${}^4\text{PrOB}\epsilon\text{aM}$ , was developed at AEC-LHEP. It allows the transverse beam emittance to be measured in less than one minute. This compact system can be installed at any location along beamlines or directly at an accelerator outport. The characterization of the proton beam produced by the 18 MeV cyclotron in operation in Bern was performed. The transverse RMS beam emittance was measured with the  ${}^4\text{PrOB}\epsilon\text{aM}$  system as a function of several cyclotron parameters. This kind of study was performed for the first time with a medical cyclotron. Such measurements are essential for the beam optimization for multi-disciplinary research and can be useful for beamline commissioning and studies of machine imperfections. The transverse RMS emittance of the Bern cyclotron was also measured for the standard machine settings with two different methods and the results were found to be in a good agreement. The proton energy distribution at the BTL of the Bern cyclotron was also assessed for the first time. On the basis of the measurements reported in this paper, a simulation of the BTL was developed in the MAD-X software. This tool is essential for the optimization of the beams employed in the ongoing research activities.

The  ${}^4\text{PrOB}\epsilon\text{aM}$  system can be deployed for similar measurements at other accelerator facilities. Further optimizations of the system, including simultaneous beam scanning in both planes are ongoing, and its commercialization is planned.

## Acknowledgments

We acknowledge contributions from LHEP engineering and technical staff. The UniBEaM detector was partially developed in the framework of the grant by the Swiss National Science Foundation CR23I2\_156852.

## References

- [1] S. Braccini and P. Scampoli, *Science with a medical cyclotron*, *CERN Courier* (2016) **April 2016** 21-22.
- [2] S. Braccini, *The new Bern PET cyclotron, its research beam line, and the development of an innovative beam monitor detector*, *AIP Conf. Proc.* **1525** (2013) 144-150.
- [3] M. Auger et al., *Low current performance of the Bern medical cyclotron down to the pA range*, *Meas. Sci. Technol.* **26** (2015) 094006.
- [4] M. Auger et al., *A detector based on silica fibers for ion beam monitoring in a wide current range*, *JINST* **11** (2016) P03027.
- [5] Methodical Accelerator Design, <http://cern.ch/madx>.
- [6] H. Wiedemann, *Particle Accelerator Physics*, Springer 2007.
- [7] K. T. McDonald and D. P. Russell, *Methods of emittance measurement*, *Month M., Turner S. (eds) Frontiers of Particle Beams; Observation, Diagnosis and Correction. Lecture Notes in Physics, Springer 343* (1989).
- [8] An object oriented framework for large scale data analysis ROOT, <http://root.cern.ch>.

- [9] F. Ziegler et al., *SRIM - The stopping and range of ions in matter*, *Nucl. Instrum. Methods B* **268** (2010) 1818-1823, <http://www.srim.org>.
- [10] A. Mostacci et al., *Chromatic effects in quadrupole scan emittance measurements*, *Phys. Rev. ST Accel. Beams*, **15** (2012) 082802.
- [11] K. P. Nesteruk et al., *Study of the transverse beam emittance of the Bern medical cyclotron*, *Proc. of IBIC2015 (Melbourne, Australia)* (2015) MOPB041, <http://www.jacow.org>.
- [12] L. David Roper et al., *Realistic Functions for Nonlinear Systems*, <http://arts.bev.net/RoperLDavid>.

# STUDY OF THE TRANSVERSE BEAM EMITTANCE OF THE BERN MEDICAL CYCLOTRON

K. P. Nesteruk<sup>a,\*</sup>, M. Auger<sup>a</sup>, S. Braccini<sup>a</sup>, T. S. Carzaniga<sup>a</sup>, A. Ereditato<sup>a</sup>, P. Scampoli<sup>a,b</sup>,

<sup>a</sup>Albert Einstein Center for Fundamental Physics, Laboratory for High Energy Physics,  
University of Bern, Switzerland

<sup>b</sup>Department of Physics, University of Napoli Federico II, Naples, Italy

## Abstract

The cyclotron laboratory for radioisotope production and multi-disciplinary research at the Bern University Hospital (Inselspital) features an IBA Cyclone 18 MeV proton cyclotron equipped with a Beam Transport Line (BTL), ending in a separate bunker. The horizontal and vertical transverse beam emittances were measured for the first time for this kind of accelerator. Two different techniques were used. A measurement based on quadrupole strength variation and beam width assessment after the last focusing section on the BTL was first performed. A second technique was developed employing 4 beam profilers located at successive positions around a beam waist. These novel beam profile detectors were developed by our group and are based on doped silica and optical fibers. For the data analysis, a statistical approach allowing for estimation of the RMS transverse emittance of a beam with an arbitrary density profile was applied. The results obtained with both methods were found to be in good agreement.

## INTRODUCTION

A cyclotron laboratory for radioisotope production and multi-disciplinary research is in operation at the Bern University Hospital (Inselspital) [1]. The facility is equipped with an IBA Cyclone 18 MeV proton cyclotron shown in Fig. 1. The cyclotron is supplied with two  $H^-$  ion sources, a redundancy aimed at maximizing the efficiency for daily medical radioisotope production. It provides high beam currents up to  $150 \mu A$  in single or dual beam mode. Extraction is realized by stripping  $H^-$  ions in a  $5 \mu m$  thick pyrolytic carbon foil.

The Bern cyclotron laboratory is equipped with a Beam Transport Line (BTL), which is a unique feature for a hospital based facility. It allows to carry out multi-disciplinary research in parallel with daily radioisotope production. A schematic view of the BTL is presented in Fig. 2. Alternate beam focusing and defocusing is realized by two horizontal-vertical (H-V) quadrupole doublets, the former located in the cyclotron bunker and the latter in that of the BTL. A movable cylindrical neutron shutter is located at the entrance of the BTL bunker to minimize the penetration of neutrons during routine radioisotope production. For scientific activities, experimental equipment such as particle detectors or specific target stations are installed at the end of the 6.5 m long BTL.



Figure 1: The Bern cyclotron opened during commissioning.

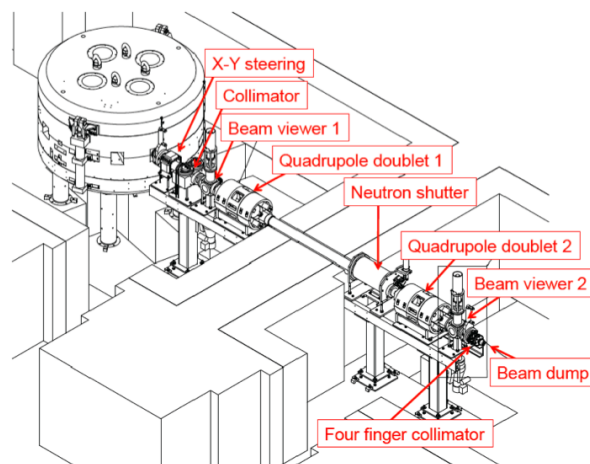


Figure 2: Schematic view of the Bern cyclotron facility, where all the main elements of the BTL are highlighted.

In this paper, we report on the first measurements of the transverse beam emittance of an IBA 18 MeV cyclotron. The measurements were conducted by means of beam profilers developed by our group and named UniBEaM. This detector is a compact device based on doped silica and optical fibers which allows for fully automatized measurements of transverse beam profiles. The first prototype of UniBEaM is described in [2]. For the measurements reported in this paper, a beam current of about 250 nA was used, which is unusual for medical cyclotrons. Such low currents are obtained with the methods described in [3]. This intensity range allows operating the UniBEaM detector in a linear

\* Corresponding author: konrad.nesteruk@lhcp.unibe.ch

regime thus avoiding distortions in the beam profiles. The transverse beam emittance was evaluated by applying two different methods, in which the beam profilers were installed along the BTL. Preliminary results are presented in the next sections.

## THE TRANSVERSE RMS BEAM EMITTANCE OF AN ARBITRARY DENSITY PROFILE

The beam emittance is the main physical quantity used to characterize an accelerated particle beam. It gives an area in the phase space of the particles. There are two phase space variables for each spatial direction - momentum and position, and the beam emittance describes the correlation between them. The transverse beam emittance can be determined for two planes - horizontal and vertical. The phase space is described by position  $x$  and angle  $x'$ , and position  $y$  and angle  $y'$  for the former and the latter plane, respectively. In further considerations, only the horizontal plane is discussed being the vertical plane completely analogous.

Realistic beams are usually far from being Gaussian and an appropriate statistical approach is required for a reliable estimation of the transverse beam emittance. In case of an arbitrary density distribution  $\rho(x, x')$ , the following moments can be defined:

$$\langle x^2 \rangle = \frac{\iint (x - \mu)^2 \rho(x, x') dx' dx}{\iint \rho(x, x') dx' dx} \quad (1)$$

$$\langle x'^2 \rangle = \frac{\iint (x' - \mu')^2 \rho(x, x') dx' dx}{\iint \rho(x, x') dx' dx}, \quad (2)$$

and the covariance:

$$\langle xx' \rangle = \frac{\iint (x - \mu)(x' - \mu') \rho(x, x') dx' dx}{\iint \rho(x, x') dx' dx}, \quad (3)$$

where  $\mu$  and  $\mu'$  are the expectation values for  $x$  and  $x'$ , respectively. The beam matrix  $\sigma(s)$  at the location  $s$  along the beamline is therefore expressed in the following way:

$$\sigma(s) = \begin{pmatrix} \sigma_{11} & \sigma_{12} \\ \sigma_{21} & \sigma_{22} \end{pmatrix} = \begin{pmatrix} \langle x^2 \rangle & \langle xx' \rangle \\ \langle xx' \rangle & \langle x'^2 \rangle \end{pmatrix}. \quad (4)$$

The RMS beam emittance  $\varepsilon_{rms}$  is then given by the determinant of the  $\sigma_s$  matrix:

$$\varepsilon_{rms} = \sqrt{\det(\sigma(s))}, \quad (5)$$

and is independent of the location  $s$  according to Liouville's theorem.

## QUADRUPOLE VARIATION METHOD

The quadrupole variation method was first used to measure the transverse beam emittance in both horizontal and vertical planes. The method is depicted in Fig. 3. The last quadrupole magnet of the BTL, located at  $s_0 = 0$ , is defocusing in the horizontal plane and focusing in the vertical. Its

strength was varied and the corresponding beam profiles at the location  $s_1 = 694$  mm were measured with the UniBEaM detector for each magnet setting. The measurements were performed for a beam current of 250 nA, which was monitored throughout the experiment by means of a Faraday cup. The profiler and Faraday cup installed on the BTL are shown in Fig. 4. The UniBEaM monitor was rotated by  $90^\circ$  for the corresponding measurements in the vertical plane.

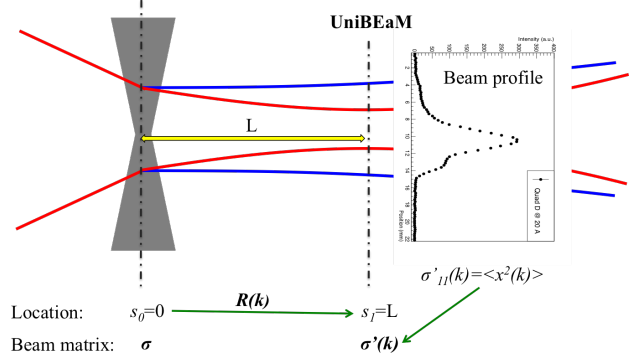


Figure 3: Variation of quadrupole strength for the measurement of the transverse beam emittance.

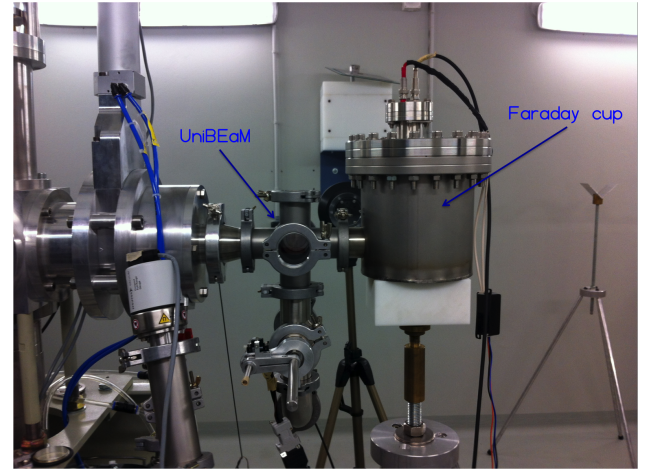


Figure 4: The UniBEaM detector and a Faraday cup installed on the BTL for the quad variation measurement of the transverse beam emittance in the horizontal plane.

Since each profile gives the marginal density distribution, the calculated variance (RMS squared) is an estimate of the  $\sigma'_{11}(k)$  component of the beam matrix  $\sigma'(k)$  at the location  $s_1$  for a given quadrupole strength  $k$ . A defocusing quadrupole magnet of an effective length  $d$  set at the strength  $k$  can be represented by the following matrix:

$$R_{DQ} = \begin{pmatrix} \cosh \sqrt{k}d & \frac{1}{\sqrt{k}} \sinh \sqrt{k}d \\ \sqrt{k} \sinh \sqrt{k}d & \cosh \sqrt{k}d \end{pmatrix}. \quad (6)$$

A drift of length  $L$  follows and leads to the matrix:

$$R_{DR} = \begin{pmatrix} 1 & L \\ 0 & 1 \end{pmatrix}. \quad (7)$$

Eventually, the beam transfer matrix  $R(k)$  is given by the matrix product:

$$R(k) = R_{DR}R_{DQ}, \quad (8)$$

which provides a linear transformation between the beam matrix  $\sigma$  at the entrance to the quadrupole and the beam matrix  $\sigma'(k)$  at the location of the UniBEaM detector. The matrix  $\sigma'(k)$  is obtained by the following algebraic operation:

$$\sigma'(k) = R(k)\sigma R(k)^T, \quad (9)$$

which gives the  $\sigma'_{11}(k)$  component as a function of  $k$ , containing three unknown parameters  $\sigma_{11}$ ,  $\sigma_{22}$ , and  $\sigma_{12} = \sigma_{21}$ . It holds:

$$\sigma'_{11}(k) = f(k; \sigma_{11}, \sigma_{12}, \sigma_{22}). \quad (10)$$

The strength  $k$  is directly related to the quadrupole current  $I$ . During the measurements, the magnet current was varied in the range 17-36 A and 25-63 A for the horizontal and vertical plane, respectively. The factor  $k$  was found on the basis of the quadrupole characteristics studies performed by the manufacturer. The components of the beam matrix  $\sigma$  at the entrance to the quadrupole and the corresponding transverse beam emittance value were obtained by performing a fit of the function  $f(I; \sigma_{11}, \sigma_{12}, \sigma_{22})$  to the data points. The estimated variance values  $\langle x^2 \rangle$  and  $\langle y^2 \rangle$  as a function of the quadrupole current together with the fitted curves are reported in Figs. 5 and 6 for the horizontal and vertical plane, respectively. The fit results for both planes and the corresponding emittance values are reported in Table 1. The transverse RMS emittance in the horizontal plane is 3.6 times bigger than the one in the vertical plane. This can be explained by the fact that particles are accelerated in the horizontal plane and therefore the position spread is significantly larger than in the vertical plane.

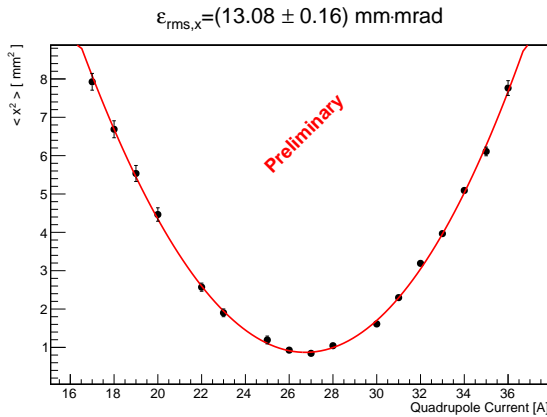


Figure 5: Variance as a function of the quadrupole current obtained in the horizontal plane. The red line corresponds to the best fit.

## MULTIPLE BEAM PROFILER METHOD

In this method, four UniBEaM detectors were installed on the BTL, as shown in Fig. 7. With respect to quad variation,

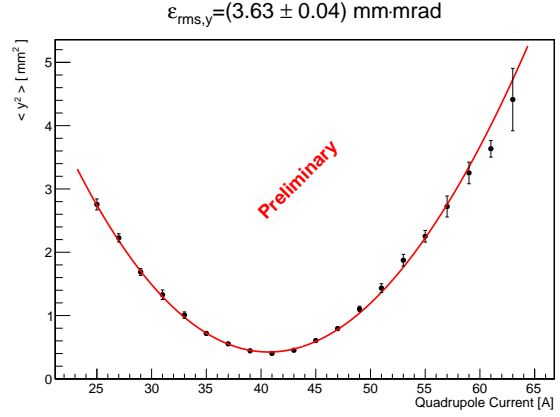


Figure 6: Variance as a function of the quadrupole current obtained in the vertical plane. The red line corresponds to the best fit.

Table 1: Fit Parameters and the RMS Emittance Values Obtained by Quadrupole Variation for Both Horizontal and Vertical Planes

Fit parameter	Horizontal plane	Vertical plane
$\sigma_{11}$ [mm <sup>2</sup> ]	$200.23 \pm 0.08$	$21.59 \pm 0.36$
$\sigma_{12}$ [mm·mrad]	$-322.66 \pm 0.08$	$-2.98 \pm 0.07$
$\sigma_{22}$ [mrad <sup>2</sup> ]	$520.80 \pm 0.22$	$1.02 \pm 0.02$
$\tilde{\chi}^2$	0.98	1.04
$\epsilon_{rms}$ [mm·mrad]	$13.08 \pm 0.16$	$3.63 \pm 0.04$

this method does not require any prior knowledge of the optical elements of the beam line. For a fixed setting of the quadrupole magnets and with a beam current of 250 nA, beam profiles were measured at four successive locations around a beam waist separated by a drift length  $L = 135$  mm, as depicted in Fig. 8. The UniBEaM monitors were rotated by 90° for the corresponding measurements in the vertical plane.

The beam profiles were analyzed in the same way, as in the case of the quadrupole variation method. The variance was calculated for each profile histogram giving an estimate of  $\sigma_{11}(s)$  component of the beam matrix  $\sigma(s)$  at the location  $s$ . The beam transfer matrix  $R(s)$  involves now only a drift:

$$R(s) = \begin{pmatrix} 1 & s \\ 0 & 1 \end{pmatrix}. \quad (11)$$

The beam matrix at any location  $s$  with respect to the location of the first profiler ( $s_0 = 0$ ) is therefore given by the formula:

$$\sigma(s) = R(s)\sigma(0)R(s)^T. \quad (12)$$

From equation (12) it can be derived that  $\sigma_{11}(s)$  is a quadratic function of  $s$ :

$$\sigma_{11}(s) = \sigma_{22}s^2 + 2s\sigma_{12} + \sigma_{11} = f(s; \sigma_{11}, \sigma_{12}, \sigma_{22}), \quad (13)$$

where  $\sigma_{11}$ ,  $\sigma_{12}$ , and  $\sigma_{22}$  are the components of the  $\sigma(0)$  matrix. These components and consequently the transverse

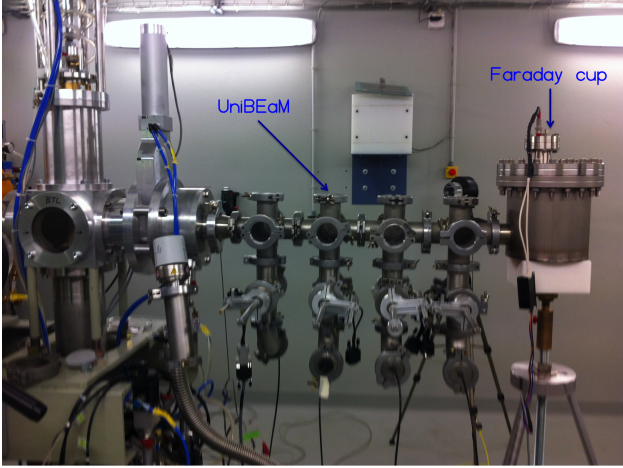


Figure 7: Four UniBEaM detectors and a Faraday cup installed on the BTL for the measurement of the transverse beam emittance in the horizontal plane.

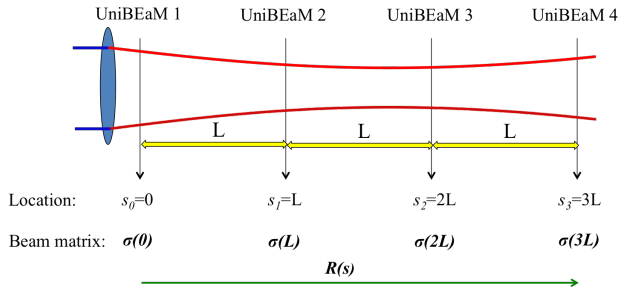


Figure 8: Multiple profilers for the measurement of the transverse beam emittance.

emittance were evaluated by fitting the  $f(s; \sigma_{11}, \sigma_{12}, \sigma_{22})$  function to the four data points representing the estimated variance values as a function of the location  $s$ , as reported in Figs. 9 and 10 for the horizontal and vertical plane, respectively. The fit results for both planes and the corresponding emittance values are reported in Table 2.

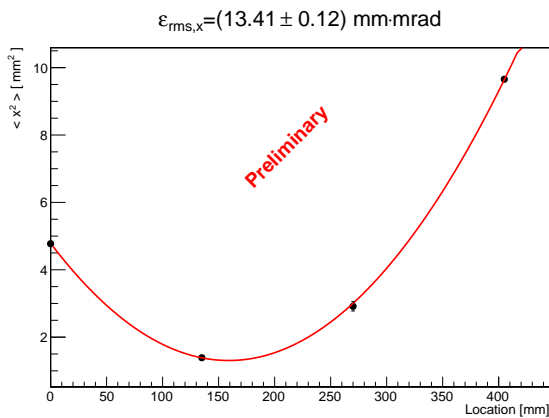


Figure 9: Variance as a function of the location obtained in the horizontal plane. The red line corresponds to the best fit.

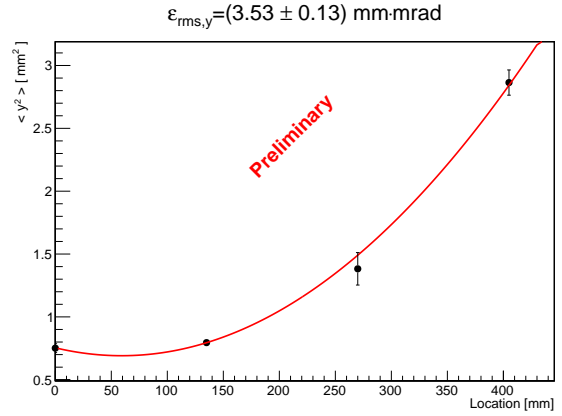


Figure 10: Variance as a function of the location obtained in the vertical plane. The red line corresponds to the best fit.

Table 2: Fit Parameters and the RMS Emittance Values Obtained by Using Multiple Profilers for Both Horizontal and Vertical Planes

Fit parameter	Horizontal plane	Vertical plane
$\sigma_{11}$ [mm <sup>2</sup> ]	$4.79 \pm 0.09$	$0.75 \pm 0.04$
$\sigma_{12}$ [mm-mrad]	$-21.90 \pm 0.48$	$-1.06 \pm 0.19$
$\sigma_{22}$ [mrad <sup>2</sup> ]	$137.72 \pm 2.06$	$17.99 \pm 1.15$
$\chi^2$	0.47	0.76
$\epsilon_{rms}$ [mm-mrad]	$13.41 \pm 0.12$	$3.53 \pm 0.13$

## CONCLUSIONS

The transverse beam emittance of the Bern medical cyclotron has been measured for the first time with the use of a novel beam monitor detector developed by our group. The emittance was evaluated with the two different techniques: quadrupole variation and multiple profilers installed along the beamline. The results were found to be in agreement within  $1.65\sigma$  and  $0.71\sigma$  for the horizontal and vertical plane, respectively. The transverse RMS beam emittance in the horizontal plane is almost 4 times bigger than the one in the vertical plane. This is due to acceleration in the horizontal plane, which causes an increase of the particle position spread along the  $x$ -direction. The measured emittance values will be implemented in the simulation of the BTL to provide beams of different shapes and sizes for multi-disciplinary research activities.

## REFERENCES

- [1] S. Braccini, *The New Bern PET Cyclotron, its Research Beam Line, and the Development of an Innovative Beam Monitor Detector*, American Institute of Physics (AIP) Conf. Proc. 1525 (2013).
- [2] S. Braccini et al., *A beam monitor detector based on doped silica and optical fibres*, 2012 JINST 7 T02001.

[3] M. Auger et al., *Low current performance of the Bern medical cyclotron down to the pA range*, Meas. Sci. Technol. 26 (2015)

094006 (6pp).



## Bibliography

- [1] W. Maciszewski and W. Scharf. Particle accelerators for radiotherapy, present status and future. *Phys. Med.*, XX:137–145, 2004.
- [2] J. Flanz. Accelerators for charged particle therapy. *Mod. Phys. Lett. A*, 30 (17): 1540020, 2015.
- [3] International Atomic Energy Agency. Cyclotron Produced Radionuclides: Principles and Practice. Technical report, Vienna, 2008.
- [4] J. J. Livingood. *Principles of cyclic particle accelerators*. D. Van Nostrand Company, Inc., 1961.
- [5] M. S. Livingston. The history of the cyclotron. *Proceedings of the 7th International Conference on Cyclotrons and their Applications, Zurich, Switzerland*, pages 635–638, 1975. <http://www.jacow.org>.
- [6] Lawrence Radiation Laboratory. *LRL Accelerators, The 184-Inch Synchrocyclotron*. UCRL-PUB-2D, 1960.
- [7] D. W. Kerst and R. Serber. Electronic Orbits in the Induction Accelerator. *Phys. Rev.*, 60:53, 1941.
- [8] F. Chautard. Beam dynamics for cyclotrons. *CAS - CERN Accelerator School: Small accelerators*, pages 209–229, 2006. CERN-2006-012.
- [9] L. H. Thomas. The Paths of Ions in the Cyclotron I. Orbits in the Magnetic Field. *Phys. Rev.*, 54:580, 1938.

## Bibliography

---

- [10] U. Amaldi. *Particle Accelerators: From Big Bang Physics to Hadron Therapy*. Springer, 2015.
- [11] U. Amaldi et al. Accelerators for hadrontherapy: From Lawrence cyclotrons to linacs. *Nucl. Instrum. Meth. A*, 620:563–577, 2010.
- [12] P. Schaffer et al. Direct Production of  $^{99m}\text{Tc}$  via  $^{100}\text{Mo}(p,2n)$  on Small Medical Cyclotrons. *Physics Procedia*, 66:383–395, 2015.
- [13] H. Wiedemann. *Particle Accelerator Physics*. Springer, 2007.
- [14] R. Q. Twiss and N. H. Frank. Orbital Stability in a Proton Synchrotron. *Rev. Sci. Instrum.*, 20:1, 1949.
- [15] K. T. McDonald and D. P. Russell. Methods of emittance measurement. *Month M., Turner S. (eds) Frontiers of Particle Beams; Observation, Diagnosis and Correction. Lecture Notes in Physics, Springer*, 343, 1989.
- [16] S. Y. Lee. *Accelerator Physics*. World Scientific, 2004.
- [17] A. Mostacci et al. Chromatic effects in quadrupole scan emittance measurements. *Phys. Rev. ST Accel. Beams*, 15:082802, 2012.
- [18] K. Ebihara et al. Non-destructive emittance measurement of a beam transport line. *Nucl. Instrum. Meth.*, 202:403–409, 1982.
- [19] S. Braccini et al. SWAN: a combined centre for radioisotope production, proton therapy and research in Bern. *Proceedings of the Workshop on Physics for Health in Europe, CERN, Geneva, Switzerland*, page 29, 2010.
- [20] S. Braccini. The new bern PET cyclotron, its research beam line, and the development of an innovative beam monitor detector. *AIP Conf. Proc.*, 1525:144, 2013.
- [21] V. Colard. Stripping member, a stripping assembly and a method for extracting a particle beam from a cyclotron, 2013. US Patent 8,432,090.
- [22] S. Braccini. *Particle Accelerators and Detectors for medical Diagnostics and Therapy*. Habilitation thesis, University of Bern, arXiv:1601.06820, 2013.

- [23] W. Kleeven. Injection and extraction for cyclotrons. *CAS - CERN Accelerator School: Small accelerators*, pages 271–296, 2006. CERN-2006-012.
- [24] M. Auger, K. P. Nesteruk et al. Low current performance of the Bern medical cyclotron down to the pA range. *Meas. Sci. Technol.*, 26:094006, 2015.
- [25] U. Reich. Beam diagnostics. *CAS - CERN Accelerator School: Small accelerators*, page 297, 2006. CERN-2006-012.
- [26] S. Braccini, K. P. Nesteruk et al. A beam monitor detector based on doped silica and optical fibres. *JINST*, 7:T02001, 2012. arXiv:1110.1583.
- [27] M. Auger, K. P. Nesteruk et al. A detector based on silica fibers for ion beam monitoring in a wide current range. *JINST*, 11:P03027, 2016.
- [28] M. Auger, K. P. Nesteruk et al. UniBEaM: a silica fiber monitor for charged particle beams. *Proceedings of WTTC16, Santa Fe (NM), USA, AIP Conf. Proc.*, 1845:020015, 2017.
- [29] D. E. Potkins, K. P. Nesteruk et al. A low-cost beam profiler based on cerium-doped silica fibers. *Proceedings of CAARI-16, Fort Worth (TX), USA, Physics Procedia*, 2016. submitted.
- [30] N. Chiodini et al. Ce-doped SiO<sub>2</sub> optical fibers for remote radiation sensing and measurement. *Proc. SPIE*, 7316:731616, 2009.
- [31] M. Neff et al. Broadband fluorescence of Sb<sup>3+</sup>-doped silica fibers. *Opt. Matter.*, 33:1, 2010.
- [32] A. Mitaroff and M. Silari. The CERN-EU high-energy Reference Field (CERF) facility for dosimetry at commercial flight altitudes and in space. *Radiat. Prot. Dosim.*, 102:7–22, 2002.
- [33] A. Vedda et al. Ce<sup>3+</sup> doped optical fibers for remote radiation dosimetry. *App. Phys. Lett.*, 85:6356, 2005.
- [34] E. Mones et al. Feasibility study for the use of Ce<sup>3+</sup> - doped optical fibres in radiotherapy. *Nucl. Instrum. Meth. A*, 562:449–455, 2006.

## Bibliography

---

- [35] K. P. Nesteruk et al. A system for online beam emittance measurements and proton beam characterization. *JINST*, 2017. submitted, Ref. JINST\_102P\_0517, arXiv:1705.07486.
- [36] K. P. Nesteruk et al. Study of the transverse beam emittance of the Bern medical cyclotron. *Proceedings of IBIC2015, Melbourne, Australia*, MOPB041:134–138, 2015. <http://www.jacow.org>.
- [37] An object oriented framework for large scale data analysis ROOT. <http://root.cern.ch>.
- [38] T. S. Carzaniga, K. P. Nesteruk et al. Measurement of Sc-43 and Sc-44 production cross-section with an 18 MeV medical PET cyclotron. *submitted to Appl. Radiat. Isot.*, 2017. Ref. ARI\_2017\_438.
- [39] J. F. Ziegler, M. D. Ziegler, and J. P. Biersack. SRIM - The stopping and range of ions in matter. *Nucl. Instrum. Methods*, B 268(11-12):1818–1823, 2010. <http://www.srim.org>.
- [40] L. David Roper. Realistic Functions for Nonlinear Systems.
- [41] Maple. <http://www.maplesoft.com>.
- [42] Methodical Accelerator Design. <http://cern.ch/madx>.
- [43] K. Jayamanna et al. The TRIUMF Compact DC H-/D- Ion Source. *Proceedings of EPAC90, Nice, France*, pages 647–649, 1990. <http://www.jacow.org>.
- [44] N. Yu. Kazarinov et al. Axial Injection Channel of IPHC Cyclotron TR24 and Possibility of Ion Beam Bunching. *Proceedings of Cyclotrons2016, Zurich, Switzerland*, TUP26:224–226, 2016. <http://www.jacow.org>.
- [45] E. Bouquerel et al. Design of a Beamline from CYRCé for Radiobiological Experiments. *Proceedings of Cyclotrons2016, Zurich, Switzerland*, THP24:359–362, 2016. <http://www.jacow.org>.

## Declaration of consent

on the basis of Article 28 para. 2 of the RSL05 phil.-nat.

Name/First Name: Nesteruk Konrad Pawel

Matriculation Number: 13-124-052

Study program: doctoral study: Physics - Doktorat PHIL NAT

Bachelor  Master  Dissertation

Title of the thesis: A new system for online measurement of the beam emittance of particle accelerators for research and medical applications

Supervisor: Antonio Ereditato

I declare herewith that this thesis is my own work and that I have not used any sources other than those stated. I have indicated the adoption of quotations as well as thoughts taken from other authors as such in the thesis. I am aware that the Senate pursuant to Article 36 para. 1 lit. r of the University Act of 5 September, 1996 is authorised to revoke the title awarded on the basis of this thesis. I allow herewith inspection in this thesis.

Bern, 09.05.2017

Place/Date

  
Signature



# Curriculum Vitae

Name: Nesteruk, Konrad Paweł

Birthday: August 2<sup>nd</sup>, 1989

Place of Birth: Siedlce, Poland

**2013-2017** Ph.D. student, Albert Einstein Center for Fundamental Physics, Laboratory for High Energy Physics of the University of Bern, Switzerland

**2015** Student of the U.S. Particle Accelerator School, *Cyclotrons*, Rutgers University, East Brunswick (NJ), USA

**2014** Student of the U.S. Particle Accelerator School, *Accelerator physics using Maple*, University of New Mexico, Albuquerque (NM), USA

**2011-2013** Master's student in physics, graduated *cum laude* in nuclear and particle physics, University of Warsaw, Poland

**2012** Laboratory assistant, Swiss Federal Institute of Technology (ETH), Zurich, Switzerland

**2012** Invited researcher, Deutsches Elektronen-Synchrotron (DESY), Hamburg, Germany

**2009, 2010, 2011, 2012** Summer student, Albert Einstein Center for Fundamental Physics, Laboratory for High Energy Physics of the University of Bern, Switzerland

**2008-2011** Bachelor's student in physics, University of Warsaw, Poland

**2005-2008** Bolesław Prus Highschool No. 1, graduated with highest honors, Siedlce, Poland